

Screw-theory-based Synthesis Method and Dynamic Behavior Study of Wheeled Mobile Robot

Siyang Long

2022

Screw-theory-based Synthesis Method and Dynamic Behavior Study of Wheeled Mobile Robot

Siyong Long

Department of Mechanical Engineering and Science
Graduate School of Engineering, Kyoto University

A thesis submitted for the degree of
Doctor of Engineering

2022

Acknowledgment

I had a dream of being a researcher when I was a child. I never thought that I could have an opportunity to realize it even when I was 33 years old. Therefore, I would like to give a huge thanks to my supervisor, Prof. Masaharu Komori, for providing me a chance to be a researcher and for the guidance, counsel, and support in my Ph.D. journey. Without his patient guide, sage advice, and excellent creativity, I can not complete the Ph.D. research so steadily and surely. More than that, he also did his best to help me to deal with the financially crippled problem in my life.

I want to give my heartfelt gratitude and appreciation to the coauthors of my research papers. Especially appreciate to Assist. Prof. Tatsuro Terakawa, not only for the detailed confirmation and insightful suggestions on the writing of papers, but also for the kind guidance and support on the research. I also want to thank Mr. Yugo Nishida and Mr. Kippe Matsuda for their preceding studies about my research. The greatest gratitude is also sent to Mr. Takumi Ougino and Mr. Yusuke Hattori for their diversified support in carrying on analyses and experiments.

I shall be grateful to all members of the Mechanism and Motion Engineering laboratory. Assist. Prof. Tetsuya Nonaka helped me construct the research environment and gave me good guidance on the daily life. Talking with him and the student members in the lab made the laboratory life full of fun and surprise.

I am deeply grateful to the Japan Society for the Promotion of Science (JSPS) and the Support for Pioneering Research Initiated by the Next Generation program operated by the Japan Science and Technology Agency (JST) for their financial support. The research was partly supported by them. The grant number is JSPS Kakenhi Grant Number 16H04257, JSPS KAKENHI Grant Number JP21K14067, and JST SPRING Grant Number JPMJSP2110, respectively.

Finally, I express my greatest gratitude to my family including my mother, my wife, and my son. Without their complete support and understanding, I am not able to finish the Ph.D. program. I was also very sorry for leaving a bit little time to accompany them in the past years. I would like to dedicate this thesis to express my greatest appreciation to them.

Contents

Chapter 1	Introduction	1
1.1	Wheeled Mobile Robot	1
1.2	Studies on Kinematics	3
1.3	Studies on Dynamics	4
1.4	Goals and Methodology	5
1.5	Thesis Organization	5
Chapter 2	Type Synthesis and Kinematic Analysis of Wheeled Locomotion Vehicle	7
2.1	Introduction	7
2.2	Brief View of Screw Theory	8
2.3	Synthesis and Modeling Methods Based on Screw Theory	9
2.3.1	Type Synthesis Method and Process	9
2.3.2	Kinematic Model Based on Screw Theory	10
2.4	An Example: Type Synthesis of an Omnidirectional Two-wheeled Vehicle	12
2.4.1	Type Synthesis of Three-DOF Two-wheeled Vehicle	12
2.4.2	Feasible Wheel Types and Combinations	13
2.4.3	Kinematic Modeling and Characteristics Analysis	15
2.5	Summary	17
Chapter 3	Type Synthesis of Six-DOF Mobile Parallel Mechanisms	19
3.1	Introduction	19
3.2	Type Synthesis Method for Mobile Parallel Mechanism	20
3.2.1	Conditions of Motion and Structure	20
3.2.2	Synthesis Method and Process	21
3.3	Type Synthesis of Connecting Chain	22
3.3.1	Applying Singularity Configuration	23
3.3.2	Using Additional Connecting Chain to Limit Undesired Motion	28
3.4	Type Synthesis of Mobile Base	29
3.4.1	Mobility Analysis	29
3.4.2	Type Synthesis of Driving Unit	30
3.5	Integration of Connecting Chain and Mobile Base	34
3.5.1	Connecting Scheme	34
3.5.2	Actuating Mechanism	35
3.5.3	Examples of Mobile Parallel Manipulator	37
3.6	Summary	39
Chapter 4	Analysis of Traveling Strategies for Driving Vehicle around a Corner	41

4.1	Introduction	41
4.2	Modeling of Vehicles and Traveling Area	42
4.2.1	Kinetic Model of Conventional Wheeled Vehicle	42
4.2.2	Kinematic Model of Omni-wheeled Vehicle	43
4.2.3	Definition of Traveling Area	44
4.3	Motion Patterns of CWV and OWV	45
4.3.1	Motion Pattern of CWV	45
4.3.2	Motion Pattern of OWV	47
4.4	Analysis and Comparison of Traveling Strategies	57
4.4.1	Traveling Strategies Analysis of CWV	58
4.4.2	Traveling Strategies Analysis of OWV	60
4.4.3	Comparison between CWV and OWV	66
4.5	Summary	68
Chapter 5 Traveling Stability of Omnidirectional Single-Track Vehicle in Roll Direction		71
5.1	Introduction	71
5.2	Kinetic Contact Model of Single-track vehicle	72
5.2.1	Model of Vehicle	73
5.2.2	Kinetic Contact Model of Vehicle	75
5.3	Motion Simulation of Single-track Vehicle	80
5.3.1	Traveling Stability	81
5.3.2	Analysis of Traveling Stability Mechanism	82
5.3.3	Effective Range of Traveling Stability	87
5.3.4	Summary of Simulation Results	89
5.4	Traveling Experiment	90
5.4.1	Experimental Setup	90
5.4.2	Experimental Results	91
5.5	Summary	94
Chapter 6 Conclusions and Future Work		97
6.1	Conclusions	97
6.2	Future Work	98
Appendix		100
	Appendix A.	100
	Appendix B.	101
Reference		102
List of Publications		108

Chapter 1

Introduction

1.1 Wheeled Mobile Robot

According to the locomotion mechanism type, mobile robots are mainly distinguished into the legged type, the wheeled type, the hybrid type, and others like the tracked type and active cord type [1-5]. The legged mobile robot, which contacts the ground with serials of points, has higher maneuverability on the rough and unstructured terrain but a more complex mechanical structure than other types. Several legged mobile mechanisms were developed: one leg [6-7], biped [8-9], quadruped [10-11], and hexapod [12-13]. The wheeled mobile robot is the most popular locomotion device in human life. It can move efficiently especially on flat and hard ground. For instance, the differential drive locomotion [14-16] and the omnidirectional locomotion [17-19] are used. The hybrid type such as leg-wheeled mobile robot combines the characteristics of the above two types of mechanisms, which make it have much higher adaptability to more complex environments [20-22]. Compared with other locomotion mechanisms, the wheeled locomotion shows the advantages of less energy consumption, lower control complexity, and a relatively simpler structure [23]. Therefore, this thesis focuses on the wheeled mobile robot.

Various wheel mechanisms have been developed in the past decades. Typical wheel mechanisms are shown in Fig. 1.1. The fixed wheel is the normal and conventional wheel, as shown in Fig. 1.1(a), which only can travel along the wheel plane direction because of the kinematic constraint [24]. A vehicle equipped with this wheel can only move forward-backward or steer toward the required direction. With this in mind, the caster wheels including the centered orientable wheel and the off-centered orientable wheel were also proposed as shown in Fig. 1.1(b) and (c) [25-26]. Their wheel planes can freely rotate around the vertical axis, so that the wheels can move in various directions. However, the singularity occurs at some conditions unconsciously when this rotation motion is passive, which increases the complexity of control.

Except for the above conventional wheels, various omnidirectional wheel mechanisms were proposed, with which the vehicle can move in an arbitrary direction immediately. A major example is the omni wheel, which has a series of free rollers along the outer circumference of the wheel main body, as shown in Fig. 1.1(d) [27-28]. When the wheel main body is driven by a motor, the wheel rotates actively in one direction. When the free rollers are rotated by an external force, the wheel runs passively in another direction. Their combination allows the vehicle with three or more omni wheels to move in an arbitrary direction. Another example is the Mecanum wheel as shown in Fig.

1.1(e), which can also be used to construct an omnidirectional vehicle. It has several free rollers attached to the circumference of the wheel main body at an angle [29-30]. The Mecanum wheel can move in a similar way to the omni wheel. The spherical wheel is a ball-shaped wheel that is driven by multiple rollers or wheels as shown in Fig. 1.1(f) [31-32]. By the combination of the rollers or wheels driven by motors, the spherical wheel can move actively in any direction.

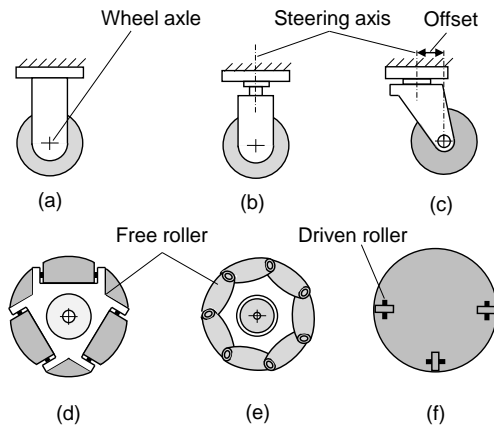


Fig. 1.1 Wheel mechanisms. (a) Fixed wheel, (b) centered orientable wheel, (c) off-centered orientable wheel, (d) omni wheel, (e) Mecanum wheel, and (f) spherical wheel.

By equipping with these wheels, the wheeled mobile robot can realize two-degree-of-freedom (DOF) or three-DOF planar motion by arranging them properly. With the two-DOF or three-DOF mobility, it can be used as a locomotion vehicle to transport goods or a manipulation tool called a wheeled mobile manipulator to operate objects. As the locomotion vehicle, it has been widely used in logistics, operation in a dangerous environment, and so on. For instance, there are the automated guided vehicle (AGV) in the factory or warehouse, and the detecting robot for high voltage lines [33-35].

Another most attractive application is the wheeled mobile manipulator, which combines the function of locomotion and manipulation. The wheeled mobile manipulator is grouped into the vehicle-mounted manipulator and the mobile parallel manipulator. The structure in which the serial manipulator or parallel manipulator mounted on the mobile base is called a vehicle-mounted manipulator as shown in Fig. 1.2(a) and (b) [36-37]. With respect to the mobile parallel manipulator shown in Fig. 1.2 (c), it is composed of an output platform, connecting chains, and a mobile base including several driving units [38]. The parallel mechanism mounted on the mobile base is called VMPPM as shown in Fig. 1.2(b), while the structure of the mobile parallel manipulator in Fig. 1.2(c) is called MPM. The wheeled mobile manipulators are not only able to transport the goods on the horizontal plane but also to handle them in space. They are widely used in industrial production, agriculture, nursing and support service, and so on. For instance, polishing robot for a turbine blade, fruit harvest robot, the household maid in the human care [39-42]. But more than these, the application of wheeled mobile robots is still growing.

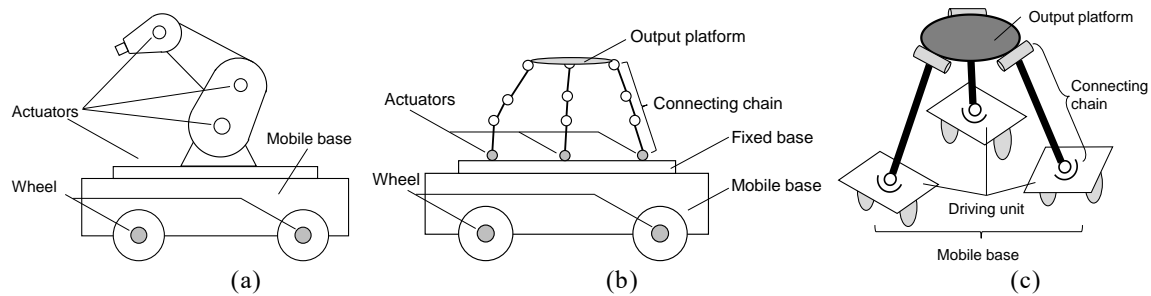


Fig. 1.2 Schematic description of mobile manipulators. (a) Mobile serial manipulator, (b) Parallel mechanism mounted on a mobile robot (VMPM), (c) Mobile parallel manipulator (MPM) [38].

1.2 Studies on Kinematics

Because of the wide application of the wheeled mobile robots, more and more attention was paid to studying them. The studies about the wheeled mobile robot are simply divided into kinematics and dynamics.

With respect to the kinematics of wheeled locomotion vehicles, various researchers mainly focused on the modeling, characteristics analysis, and the kinematics control. The kinematic modeling is the first step for mobility analysis and control of the wheeled mobile robot. Many modeling methods were proposed, including the vector approach [43], the geometric approach [44], and the transfer approach [45]. The kinematic models were constructed for the robot on flat ground or uneven terrain [46-47]. To evaluate the kinematic characteristics of the wheeled mobile robots, various indices were proposed such as maneuverability, mobility, singularity, and isotropy [48-50]. Based on the kinematic model, the position control method without consideration of the dynamic properties was proposed for the wheeled mobile robot [51-52].

With respect to the kinematics of wheeled mobile manipulators, the studies mainly focused on the forward/inverse kinematics and the analysis of the characteristics. Various methods were proposed to solve the inverse kinematic equation because of its nonlinearity, e.g. Newton-Raphson method [53] and neural networks [54]. The singularity, manipulability, and workspace were analyzed to assess the ability of the wheeled mobile manipulator [55-57].

These studies focused primarily on the kinematics and property analyses of the specified wheeled locomotion vehicle or the mobile manipulator. The type synthesis is determining the structure of a mechanism according to the mobility requirement, such as the wheel composition of the wheeled locomotion vehicle or the chain structure of the mobile parallel mechanism. It is an important stage of their design. However, their type synthesis method has been rarely reported. The wheel types and layout were generally determined through trial-and-error method, which took effort. Considering the wheeled locomotion vehicles, various wheel mechanisms were proposed as introduced in the previous section. Therefore, to realize the two-DOF or three-DOF mobility, many feasible wheel types and combinations may exist according to the mobility requirement. To fill the design gap, it is

necessary to establish a type synthesis method for the wheeled locomotion vehicle. On the other hand, the type synthesis method of MPMs also needs to be constructed. The type synthesis of conventional parallel mechanisms can be applied in that of VMPMs shown in Fig. 1.2(b) [58-59]. However, the MPM shown in Fig. 1.2(c) is equipped with several driving units, which is different from the conventional parallel mechanism with a fixed base. Therefore, the type synthesis method of conventional parallel mechanisms cannot be applied to the MPM.

1.3 Studies on Dynamics

The dynamics modeling of wheeled locomotion vehicles is the basis of studies. Many researchers had proposed the dynamics modeling method based on the Lagrange formulation, Newton-Euler formulation, and their extensions [60-62]. To make the motion of the robot closer to the real world, the dynamics modeling was constructed with consideration of the longitudinal or lateral slip of the wheel [63-64].

The research theme about the dynamics of the wheeled locomotion vehicles other than the modeling mainly focuses on navigation and motion control. This thesis focuses on the path planning for navigation as an application of the dynamics. Path planning is grouped into path generation and trajectory tracking. With consideration of the velocity constraint or the torque constraint, the path generation gives the time-optimal trajectory, the obstacle-avoiding path, the smooth path, or the minimum power-consumption path [65-68]. Various methods were developed to obtain these paths, for instance, the potential field method, the cell decomposition approach, the heuristic approach like the neural network, and so on [69]. The trajectory tracking aims to make the robot moves along the designated path precisely. It is essentially a control problem for the wheeled locomotion vehicle. Various controllers were designed for the tracking control of wheeled locomotion vehicles. For instance, nonlinear model predictive control, robust tracking control, receding horizon controller, and so on [70-71].

The above studies about dynamics were mostly conducted on the conventional-wheeled vehicle, while rarely on the omnidirectional-wheeled vehicle. For instance, the traveling strategies of omnidirectional-wheeled vehicles have not been investigated when they are required to travel on a curve path. An omnidirectional-wheeled vehicle has three DOFs and can move in an arbitrary direction immediately. Therefore, various traveling strategies are available even when they are required to turn a corner. As a reference to the path generation, it is necessary to clarify the characteristics of each traveling strategy and systematically show what kind of traveling strategy is suitable for each situation for the omnidirectional-wheeled vehicle.

For another example, the rolling characteristics of single-track vehicles are important to prevent falling. The rolling characteristics of conventional-wheeled vehicles, such as bicycles and motorbikes, have been studied to keep balance with respect to the dynamics. Many researchers tried

to realize self-balancing by adding flywheels or controlling the steering [72-74]. However, it mainly concerned the vehicle equipped with conventional tired wheels, while the dynamic characteristics of the omnidirectional-wheeled single-track vehicle in roll direction were rarely investigated.

1.4 Goals and Methodology

This thesis aims to solve the abovementioned problems of wheeled mobile robots with respect to kinematics and dynamics. Regarding the kinematics, the screw-theory-based type synthesis methods for wheeled locomotion vehicles and MPMs are proposed. The feasible wheel compositions, as well as the structures of chains, are figured out by handling the wheeled mechanism and the parallel mechanism uniformly as the combination of revolute pairs and prismatic pairs according to the mobility requirement. With respect to the dynamics, the traveling strategy for path planning and the traveling stability for stabilization control of omnidirectional-wheeled locomotion vehicles are studied. Based on the acceleration/deceleration behavior and the nonslip condition, the possible traveling patterns of omnidirectional-wheeled vehicles are shown analytically to reveal the advantages of each traveling form according to the various path conditions. Then the traveling strategies of the omnidirectional-wheeled locomotion vehicle are proposed and compared with that of the conventional-wheeled locomotion vehicle. Additionally, the dynamics characteristics of the omnidirectional-wheeled single-track vehicle in the roll direction are investigated. Through the analysis of the wheel-ground contact mechanism, the traveling stability of the wheeled locomotion vehicle is investigated. By taking the vehicle with double-row active omni wheels as an example, the system of the rolling stability of the vehicle and the conditions of keeping the vehicle stable without any control are identified.

1.5 Thesis Organization

The thesis is composed of six chapters.

Chapter 1 introduces a background of this research and designates the problems in the current study for wheeled mobile robots, which is grouped into two categories: kinematics and dynamics. The aim and approach of the thesis are described briefly.

Chapter 2 proposes a screw-theory-based type synthesis method to obtain the feasible wheel types and combinations for the wheeled locomotion vehicle according to the requirement of mobility. A kinematic modeling method is also proposed based on the screw theory, based on which the kinematic characteristics are analyzed to determine the wheel layout. Then an example of synthesizing the two-wheeled locomotion vehicle with three-DOF mobility is performed based on the proposed method. The vehicles regarding the synthesized wheel types and combinations are modeled and analyzed to verify the validity of the proposed method.

Chapter 3 proposes the type synthesis method for the MPM based on the screw theory. The type synthesis of the MPM is divided into that of the connecting chain and the mobile base, where the synthesis of the mobile base is conducted based on the synthesis method proposed in Chapter 2. The synthesis method of connecting chain is constructed based on the method of achieving the required mobility by applying the singularity configuration and the adding an additional chain. The methods of integrating the connecting chain and the mobile base are discussed and revealed. Based on the proposed type synthesis method, novel MPM structures are enumerated and analyzed.

Chapter 4 presents the possible traveling strategies for the omnidirectional-wheeled vehicle when it is required to travel on a specified path with one corner. The kinetic model of the vehicle is established based on the nonslip condition. The possible traveling patterns are proposed based on the kinetic model. The time cost is analyzed and compared when the path conditions are varied. The feasible traveling strategies are suggested based on the above analysis. Finally, the traveling strategies of omnidirectional-wheeled vehicles are compared with that of conventional-wheeled vehicles.

Chapter 5 deals with the traveling stability in the roll direction of an omnidirectional-wheeled single-track vehicle with respect to the dynamics. The single-track vehicle equipped with two double-row active omni wheels is chosen as the subject, the effect of the double-row wheel structure on the rolling stability is investigated. The stabilization mechanism is analyzed and confirmed through simulation based on the dynamic model considering the contact state between the outer rollers and the ground. Experiments are conducted on a developed prototype to verify the effectiveness of double-row structure on rolling stability further.

Chapter 6 summarizes the conclusions in each chapter and states the further study.

Chapter 2

Type Synthesis and Kinematic Analysis of Wheeled Locomotion Vehicle

2.1 Introduction

Wheeled locomotion vehicles are widely used as a transport tool in factories and warehouses. They are grouped into the two-DOF type and three-DOF type. The wheeled locomotion vehicles with two fixed wheels have two DOFs, which can actively move forward-backward or turn corresponding to the DOFs. However, it cannot move in the lateral or diagonal direction without turns or switchbacks. The three-DOF locomotion vehicles are equipped with omnidirectional wheel mechanisms, which let the vehicles move in an arbitrary direction immediately. As a result, the three-DOF locomotion vehicle can move efficiently even on a narrow passage.

Concerning the two-DOF or three-DOF locomotion vehicles, various studies were reported as introduced in Chapter 1. However, such studies were mainly conducted on wheeled locomotion vehicles with specified wheel compositions. The type synthesis method of two-DOF or three-DOF wheeled locomotion vehicles has been rarely studied. Therefore, subject to the two-DOF or three-DOF mobility requirement, the possible wheel compositions (including types, combinations, and layouts) are comprehensively unknown. Additionally, the previous method of determining the wheel composition was first establishing the kinematic model for the specified wheel compositions. Then the Jacobian matrix was calculated to confirm the degree of mobility. If the degree of mobility satisfied the requirement, the wheel types and combinations were obtained and the kinematic analysis was conducted to confirm singularity to determine the final wheel layouts. If the degree of mobility did not satisfy the requirement, the wheel types or combinations would be modified and the kinematic model was remodeled to confirm the degree of mobility again. Such trial-and-error method took effort especially the repeated calculation of Jacobian matrix.

In the previous studies, the wheel mechanisms were considered as the compositions of revolute pairs and prismatic pairs to construct the kinematic model. For example, Muir firstly constructed the kinematic model of a wheeled mobile robot by applying the Sheth-Uicker convention with considering the wheel as high pairs [45]. Therefore, the type synthesis method of the parallel link mechanisms can also be applied in the synthesis of wheel mechanisms by considering them as combinations of pairs. On the other hand, many type synthesis methods have been proposed for parallel link mechanisms, which are based on the screw theory, the theory of differential geometry, linear transformation and evolutionary morphology theory, and so on [75-78]. Among these methods,

the screw-theory-based method can intuitively express the rotation and translation motion of the rigid body by vectors. Additionally, the mobility of the mechanism can be analyzed easily by the geometrical method based on the screw theory.

Based on the above analysis, this chapter proposes a screw-theory-based method to solve the type synthesis issue of the wheeled locomotion vehicles. An example of the synthesis of the two-wheeled omnidirectional locomotion vehicle is shown to explain the method. The kinematic model and characteristics are constructed and analyzed to verify the validity of this method.

2.2 Brief View of Screw Theory

A brief review of the screw theory is introduced in this section [79]. A unit screw can be written by

$$\hat{\$} = [\lambda \mathbf{s} + \mathbf{s}_0 \times \mathbf{s}] = [L \quad M \quad N \quad P \quad Q \quad R]^T \quad (2.1)$$

where \mathbf{s} is a unit vector that defines the direction of the screw axis, \mathbf{s}_0 defines the position of a point on the screw axis that refers to the reference coordinate system, λ is the pitch of the screw, and L , M , N , P , Q , and R are the Plücker coordinates of the screw. When $\lambda = 0$, the screw is a zero-pitch screw, while an infinite-pitch screw exists when $\lambda = \infty$. These two types of screws are given as:

$$\hat{\$} = \begin{cases} [\mathbf{s}_0 \times \mathbf{s}] & \text{if } \lambda = 0 \\ [\mathbf{0}] & \text{if } \lambda = \infty \end{cases} \quad (2.2)$$

When two screws satisfy the following equation, they are reciprocal to each other.

$$\$_r \circ \$ = S_{r4}S_1 + S_{r5}S_2 + S_{r6}S_3 + S_{r1}S_4 + S_{r2}S_5 + S_{r3}S_6 = 0, \quad (2.3)$$

where $\$ = [S_1 \quad S_2 \quad S_3 \quad S_4 \quad S_5 \quad S_6]$ and $\$_r = [S_{r1} \quad S_{r2} \quad S_{r3} \quad S_{r4} \quad S_{r5} \quad S_{r6}]$. The geometrical conditions for the reciprocal screws are as follows:

Rule A1. Two zero-pitch screws are reciprocal to each other unless they are coplanar.

Rule A2. Two infinite-pitch screws are always reciprocal to each other regardless of their positions and orientations.

Rule A3. A zero-pitch screw is reciprocal to an infinite-pitch screw only when they are perpendicular to each other.

The screw is applied to represent the instantaneous motions of or constraints imposed on a rigid body, which are called a twist and a wrench, respectively. Their Plücker coordinates are as follows:

$$\hat{\$} = \begin{cases} [\omega_x \quad \omega_y \quad \omega_z \quad v_x \quad v_y \quad v_z] & \text{if the screw represents a twist} \\ [f_x \quad f_y \quad f_z \quad m_x \quad m_y \quad m_z] & \text{if the screw represents a wrench} \end{cases} \quad (2.4)$$

When the screw is a twist, the first three components represent the rotation motion, while the last three components represent the translational motion. When the screw is a wrench, the first three components represent the force constraint, while the latter three components represent the couple constraint.

A twist system with n linearly independent screws is called an n -system, the corresponding wrench system forms a $(6 - n)$ -system.

2.3 Synthesis and Modeling Methods Based on Screw Theory

The type synthesis method of wheeled locomotion vehicles is introduced in this section. The type synthesis of the wheeled locomotion vehicle is divided into two steps. First is the synthesis of the wheel types and combinations, after which the vehicle regarding the synthesized wheel types and combinations is modeled and analyzed to obtain the most proper wheel layout.

2.3.1 Type Synthesis Method and Process

The screw-theory-based synthesis method is introduced in this section. It is assumed that the wheel contacts the ground at a point and does not slip. Therefore, all types of wheels can be equivalent to the combination of a revolute pair and one or two prismatic pairs. For example, the fixed wheel and centered orientable wheel are equivalent to the combination of a passive revolute pair that is perpendicular to the ground and an active prismatic pair that is parallel to the wheel plane.

Additionally, the wheeled locomotion vehicle can be considered equivalent to a planar parallel mechanism when its wheels are regarded as higher pairs. Therefore, the wheel types and combinations can be obtained by a series of reciprocal product calculations. The required mobility of the vehicle can be represented by twists. Through the reciprocal product calculation of these twists, the wrench imposed on the vehicle chassis is obtained. The twist representing the wheel can be given through the reciprocal product of the abovementioned wrench. By considering these conditions, the feasible wheel types and combinations of the vehicle can be obtained with respect to the mobility requirement. After that, the kinematic models of the vehicle regarding these wheel types and combinations are established, based on which the kinematic characteristics are analyzed to obtain the feasible wheel layout. Then the feasible structure of the vehicle can be obtained. Summarizing the above, the proposed synthesis process is as shown in Fig. 2.1.

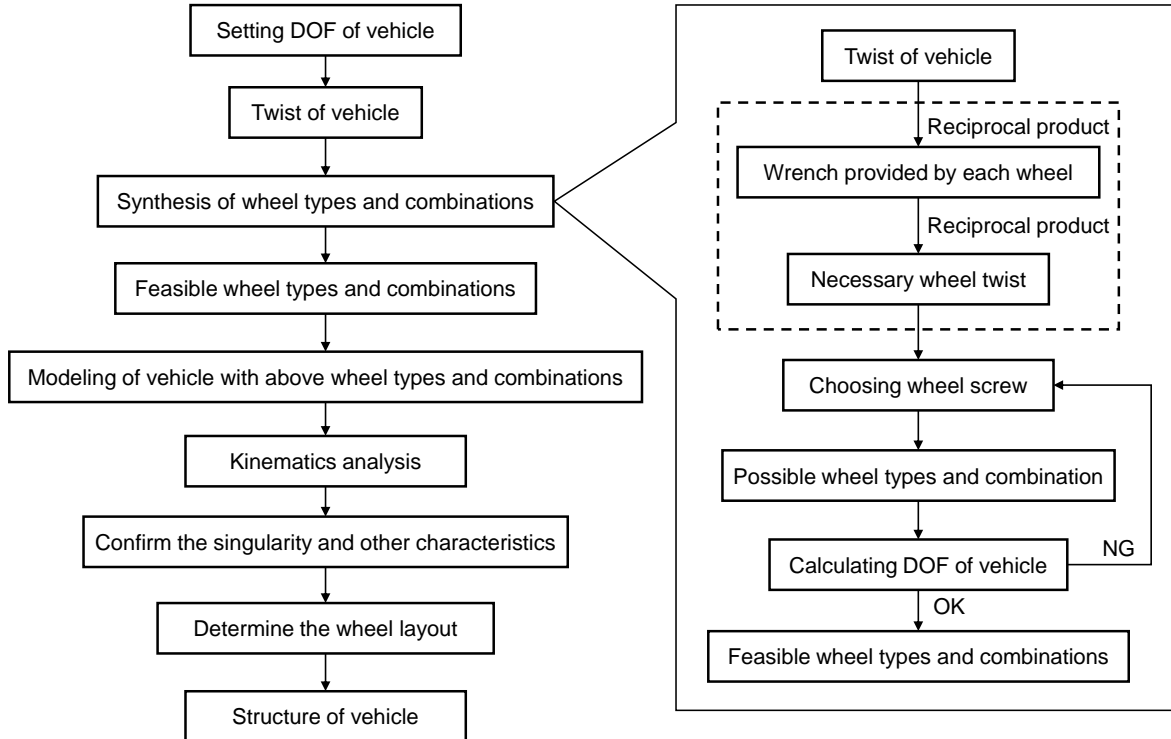


Fig. 2.1 Type synthesis flowchart of a wheeled locomotion vehicle according to the mobility.

2.3.2 Kinematic Model Based on Screw Theory

To obtain the feasible wheel layout, modeling is necessary for the kinematic analysis. As introduced in Chapter 1, many methods were proposed in the kinematic modeling of wheeled locomotion vehicles. A new kinematic modeling method based on the screw theory is introduced in this section. A schematic model of a wheel referring to the vehicle body is shown in Fig. 2.2. A coordinate system $O-xy$ is fixed at the center of the vehicle. It is assumed that wheel i contacts the ground at point P , which leaves from point O with distance l_{wi} . All wheels except for the fixed wheel and centered orientable wheel are equivalent to the combination of a revolute pair and two prismatic pairs according to the discussion in the above section. The translation velocity along the wheel plane is \dot{g}_i , which also represents the velocity of the corresponding prismatic pair. The moving velocity vertical to the wheel plane is \dot{f}_i , which also denotes the velocity of another prismatic pair. The rotation velocity around the vertical axis passing through point P is \dot{e}_i , which can be seen as the velocity of the revolute pair. The angle between line OP and the x axis is α_i . The angle between the line OP and the wheel axle is β_i .

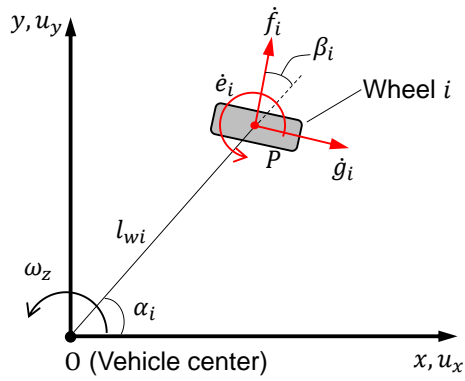


Fig. 2.2 Schematic model of a wheel

The ground, the wheel, and the vehicle chassis combine as an open-loop link chain. The vehicle velocity is calculated according to the screw theory as follows:

$$\$_v = \dot{g}_i \$_{i1} + \dot{f}_i \$_{i2} + \dot{e}_i \$_{i3}, \quad (2.5)$$

where $\$_v = [0 \ 0 \ \omega_z \ u_x \ u_y \ 0]$ is a twist screw representing the velocity of the vehicle, u_x and u_y are the velocity along the x - and y -axis directions, respectively, ω_z is the rotation velocity around the axis vertical to the ground, $\$_{i1}$ is the screw representing the equivalent prismatic pair along the wheel plane, $\$_{i2}$ is the screw representing the equivalent prismatic pair vertical to the wheel plane, and $\$_{i3}$ is the screw representing the equivalent revolute pair vertical to the ground.

If \dot{g}_i is controlled by a motor, it means the infinite-pitch screw $\$_{i1}$ is active. A screw $\$_{rg}$ that is reciprocal to the remained passive zero-pitch and infinite-pitch screws can be found through the geometrical method. Take the reciprocal product to both sides of Eq. (2.5) with the reciprocal screw of $\$_{i2}$ and $\$_{i3}$, the following equation is obtained:

$$\$_v \circ \$_{rg} = \dot{g}_i \$_{i1} \circ \$_{rg}, \quad (2.6)$$

Similarly, if \dot{f}_i is controlled by a motor, it means the infinite-pitch screw $\$_{i2}$ is active. The screw $\$_{rf}$ reciprocal to the remained passive screws is also easy to obtain by the geometrical method. Take the reciprocal product to both sides of Eq. (2.5) with the reciprocal screw of $\$_{i1}$ and $\$_{i3}$, the following equation is obtained:

$$\$_v \circ \$_{rf} = \dot{f}_i \$_{i2} \circ \$_{rf}, \quad (2.7)$$

Based on the above discussion, the kinematic equation of the vehicle is established by combining Eqs. (2.6) and (2.7) according to the motor configuration.

2.4 An Example: Type Synthesis of an Omnidirectional Two-wheeled Vehicle

In order to show the details of the proposed synthesis methods, the type synthesis of an omnidirectional two-wheeled vehicle is given. Compared with three- or four-wheeled automobiles, two-wheeled vehicles have high maneuverability even in a narrow passage or on a winding road. Additionally, the wheel arrangement is flexible, such as the front-rear type belonging to single-track vehicle or the left-right type belonging to double-track vehicle. However, conventional two-wheeled vehicles equipped with fixed wheels need to turn or switch back when moving toward specific directions, which reduces their maneuvering efficiency when moving in a limited space or avoiding obstacles. Therefore, the two-wheeled vehicle with three-DOF mobility is needed. The proposed method is applied to figure out the possible wheel compositions to realize the three-DOF mobility.

2.4.1 Type Synthesis of Three-DOF Two-wheeled Vehicle

The three-DOF mobility means the position and orientation of the vehicle need to be changeable. Therefore, the vehicle twist system is written by:

$$\begin{cases} \hat{\$}_1 = [0 & 0 & 1 & 0 & 0 & 0] \\ \hat{\$}_2 = [0 & 0 & 0 & 1 & 0 & 0], \\ \hat{\$}_3 = [0 & 0 & 0 & 0 & 1 & 0] \end{cases} \quad (2.8)$$

where $\hat{\$}_1$, $\hat{\$}_2$, and $\hat{\$}_3$ represent the rotation around the z axis, translation along the x axis, and translation along the y axis, respectively, referring to the coordinate system fixed on the center of the vehicle as shown in Fig. 2.3.

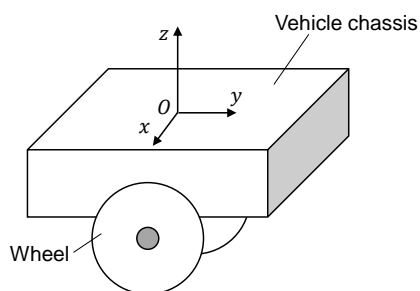


Fig. 2.3 Schematic model of vehicle

The wrench system imposed on the vehicle chassis can be obtained easily via using the geometrical method of determining the reciprocal screw, which is the same as its twist system [81]. Therefore, the wrench imposed on the vehicle by the wheels is a three-system as follows:

$$\begin{cases} \hat{\$}_1^r = [0 & 0 & 1 & 0 & 0 & 0] \\ \hat{\$}_2^r = [0 & 0 & 0 & 1 & 0 & 0] \\ \hat{\$}_3^r = [0 & 0 & 0 & 0 & 1 & 0] \end{cases} \quad (2.9)$$

When applying the above wrench system to the vehicle chassis, the twist of each wheel can be one-, two-, or three-system, and the twist can be written by one of the following screws or a linear combination of them:

$$\begin{cases} \hat{\$}_1^t = [0 & 0 & 1 & 0 & 0 & 0] \\ \hat{\$}_2^t = [0 & 0 & 0 & 1 & 0 & 0] \\ \hat{\$}_3^t = [0 & 0 & 0 & 0 & 1 & 0] \end{cases} \quad (2.10)$$

Since the total number of the actuators is normally equal to the DOFs of the vehicle, at least one wheel must have two active DOFs when the vehicle is equipped with two wheels. Therefore, the wheel twist is either a two- or a three-system. In the two-system case, the vehicle twist is divided into two types. One is the linear combination of $\hat{\$}_1^t$ with $\hat{\$}_2^t$ or $\hat{\$}_3^t$, which represents the rotation about the z axis and translation along the x - or y -axis direction, while the other is the linear combination of $\hat{\$}_2^t$ with $\hat{\$}_3^t$, which represents the translation along the x - and y -axis directions.

2.4.2 Feasible Wheel Types and Combinations

As introduced in Chapter 1, various wheel mechanisms were proposed in the previous studies. However, they have only one active DOF. To realize the three-DOF mobility of the two-wheeled vehicle, one of the wheels should have two active DOFs. To meet this requirement, the active omni wheel (AOW) is used here, which can actively move along or vertical to the wheel plane [80].

When the vehicle is equipped with an AOW and a fixed wheel as shown in Fig. 2.4(a), the motion of the AOW is represented by a zero-pitch screw $\hat{\$}_1^z$ and two infinite-pitch screws $\hat{\$}_1^x$ and $\hat{\$}_1^y$, while the motion of the fixed wheel is represented by a zero-pitch screw $\hat{\$}_2^z$ and an infinite-pitch screw $\hat{\$}_2^y$. The screw $\hat{\$}_i^z (i = 1, 2)$ denotes the rotation motion around the axis vertical to the ground, which is shown by the black solid line. The screws $\hat{\$}_i^x$ and $\hat{\$}_i^y$ represent the translation motion along the wheel axle and wheel plane directions, respectively, both of which are shown by the black dash line. The AOW chain forms a three-system twist, while the fixed wheel chain forms a two-system twist. It is easy to obtain the reciprocal screws of each twist system as shown by the red solid lines and dash lines according to the geometrical method of determining the reciprocal screw, which are the wrench constraints acting on the vehicle chassis. By calculating the reciprocal product to the wrenches, the twist representing the mobility of the vehicle is obtained as shown by the blue line.

The twist shows that the vehicle can only move along the wheel plane direction of the fixed wheel and rotate around the vertical axis passing through the contact point between the fixed wheel and the ground. Therefore, when the AOW is combined with the fixed wheel, the vehicle only has

two active DOFs. Similarly, the vehicle also only has two active DOFs when the vehicle is equipped with an AOW and a centered orientable wheel as shown in Fig. 2.4(b).

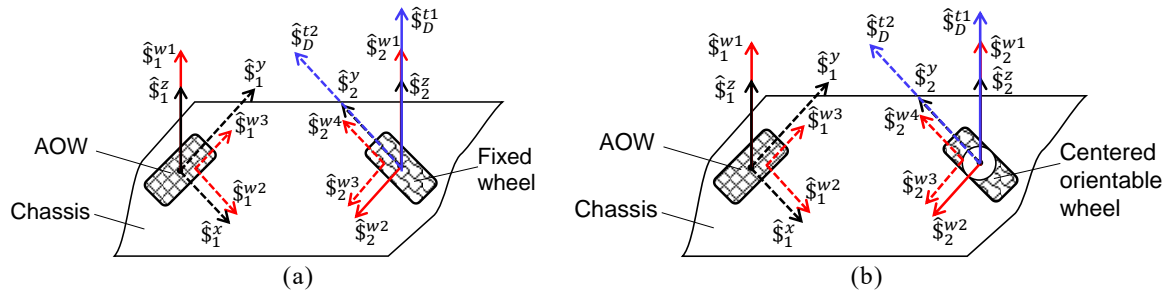


Fig. 2.4 Screws of a vehicle equipped with AOW and fixed wheel or centered orientable wheel. (a) A vehicle equipped with AOW and fixed wheel. (b) A vehicle equipped with AOW and centered orientable wheel

On the other hand, when the vehicle is equipped with an AOW and the other types of wheels that are equivalent to a revolute pair and two prismatic pairs, such as the off-centered orientable wheel or omni wheel, the screw system formed by the wheel chains is shown in Fig. 2.5. As a result of the same calculating process of the reciprocal screw as the above, the motion screw of the vehicle is a three-system twist. This means that the vehicle is capable of three-DOF mobility.

Therefore, the vehicle can realize three-DOF mobility by equipping with an AOW and any other wheels except for the fixed wheel and centered orientable wheel. Similarly, the two-AOW wheel layout is also feasible to realize three-DOF mobility.

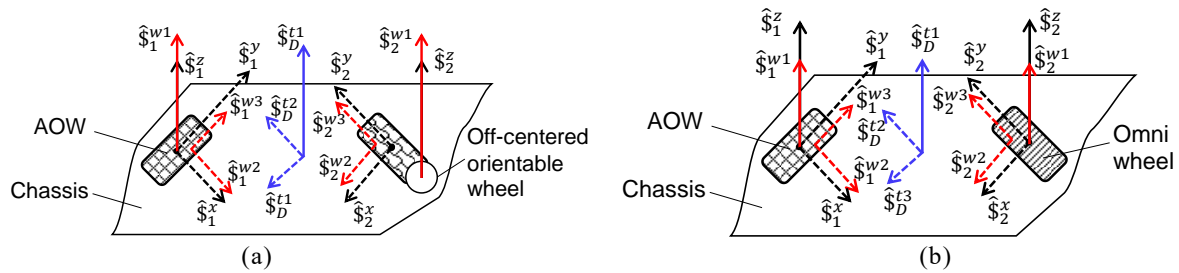


Fig. 2.5 Screws of a vehicle equipped with an AOW and an omni wheel or off-centered orientable wheel. (a) A vehicle equipped with an AOW and an off-centered orientable wheel. (b) A vehicle equipped with an AOW and an omni wheel

Overall, the vehicle can realize the three-DOF mobility when the vehicle is equipped with an AOW and an off-centered orientable wheel, an omni wheel, or another AOW. Examples of the wheel types and combinations are shown in Fig. 2.6. Note that the following example only show the configuration of the driving wheels.

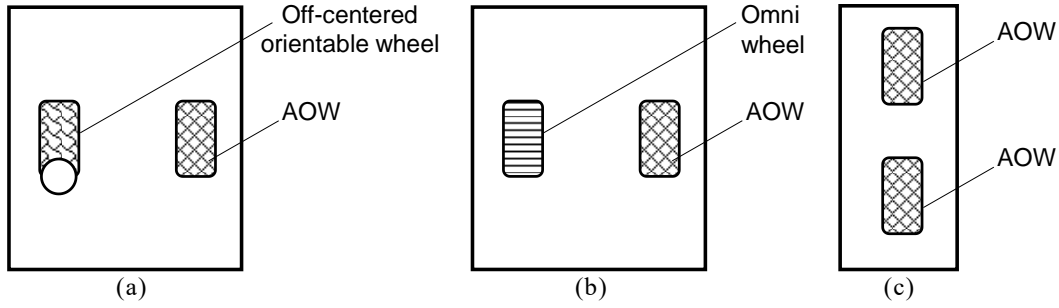


Fig. 2.6 Examples of feasible wheel layouts

2.4.3 Kinematic Modeling and Characteristics Analysis

The proposed modeling method is applied to establish the kinematic model of the vehicle in this section. It is verified by constructing the kinematic model of the vehicle with the synthesis result in the previous section. The velocity characteristics of the vehicle regarding the specified wheel layouts are discussed.

2.4.3.1 Vehicle Equipped With AOW and Omni wheel

When the vehicle is equipped with an AOW and an omni wheel, the screws represent the pairs of both wheels are written by

$$\begin{cases} \$i_1 = [0 & 0 & 0 & \sin(\alpha_i + \beta_i) & -\cos(\alpha_i + \beta_i) & 0] \\ \$i_2 = [0 & 0 & 0 & \cos(\alpha_i + \beta_i) & \sin(\alpha_i + \beta_i) & 0] \\ \$i_3 = [0 & 0 & 1 & l_{wi}\sin\alpha_i & -l_{wi}\cos\alpha_i & 0] \end{cases} \quad (2.11)$$

where index $i = 1$ represents the parameters of the AOW, index $i = 2$ represents that of the omni wheel.

The reciprocal screw of the remained passive zero-pitch and infinite-pitch screws can be found through the geometrical method. The reciprocal screws is $\$rgi = [\sin(\alpha_i + \beta_i) \quad -\cos(\alpha_i + \beta_i) \quad 0 \quad 0 \quad 0 \quad -l_{wi}\cos\beta_i]$ corresponding to that the velocities along the wheel plane are controlled by the motors. The other reciprocal screw is $\$rfi = [\cos(\alpha_i + \beta_i) \quad \sin(\alpha_i + \beta_i) \quad 0 \quad 0 \quad 0 \quad l_{wi}\sin\beta_i]$ corresponding to that the velocities perpendicular to the wheel plane are controlled by the motors. Substituting $\$rgi$ and $\$rfi$ for $\$rg$ and $\$rf$ in Eqs. (2.6) and (2.7), then the kinematic equation of the vehicle is written by

$$J[u_x \quad u_y \quad \omega_z]^T = [g_1 \quad f_1 \quad g_2]^T, \quad (2.12)$$

where

$$J = \begin{bmatrix} \sin(\alpha_1 + \beta_1) & -\cos(\alpha_1 + \beta_1) & -l_{w1}\cos\beta_1 \\ \cos(\alpha_1 + \beta_1) & \sin(\alpha_1 + \beta_1) & l_{w1}\sin\beta_1 \\ \sin(\alpha_2 + \beta_2) & -\cos(\alpha_2 + \beta_2) & -l_{w2}\cos\beta_2 \end{bmatrix},$$

Note that the lateral velocity \dot{f}_2 is passive, and the constraint equation can also be obtained by the same method shown in Section 2.4. Additionally, the constructed kinematic model is the same as that shown in the previous study [82]. Then, the feasibility of the established method for the kinematic model based on the screw theory is verified.

When the determinate of the matrix J is zero, the vehicle is at the singular configuration. The equation of the singular condition is shown in Eq. (2.13). It should be avoided by arranging the wheel properly according to the following equation.

$$l_{w1} \cos(\alpha_2 + \beta_2 - \alpha_1) - l_{w2} \cos\beta_2 = 0 \quad (2.13)$$

The velocity of AOW is maximum when it moves to the forward-backward or transverse direction, while the velocity is limited to a lower value in the diagonal direction [83]. Considering this point, it is assumed that both \dot{g}_1 and \dot{f}_1 are limited in the same range $(-V_{max}, V_{max})$. The velocity \dot{g}_2 of the omni wheel is also limited in the same range. With respect to the wheel layout shown in Fig. 2.6 (b), the maximum velocity distribution of the vehicle is shown in Fig. 2.7. It shows that the velocity in both the front-rear direction and lateral direction is larger than the diagonal direction.

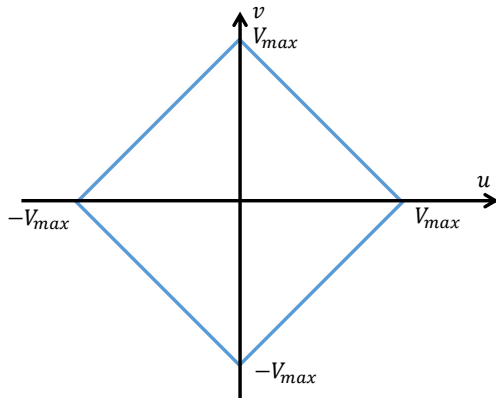


Fig. 2.7 Maximum velocity distribution of a vehicle equipped with an AOW and an omni wheel.

2.4.3.2 Vehicle Equipped with Two AOWs

When the vehicle is equipped with two AOWs, the kinematic equation of the vehicle is written by

$$J[u_x \quad u_y \quad \omega_z]^T = [\dot{g}_1 \quad \dot{f}_1 \quad \dot{g}_2 \quad \dot{f}_2]^T, \quad (2.14)$$

where

$$J = \begin{bmatrix} \sin(\alpha_1 + \beta_1) & -\cos(\alpha_1 + \beta_1) & -l_{w1} \cos\beta_1 \\ \cos(\alpha_1 + \beta_1) & \sin(\alpha_1 + \beta_1) & l_{w1} \sin\beta_1 \\ \sin(\alpha_2 + \beta_2) & -\cos(\alpha_2 + \beta_2) & -l_{w2} \cos\beta_2 \\ \cos(\alpha_2 + \beta_2) & \sin(\alpha_2 + \beta_2) & l_{w2} \sin\beta_2 \end{bmatrix}$$

and indices 1 and 2 represent the parameters of two AOWs, respectively. The kinematic model is the same as that shown in the previous study [80]. With respect to the wheel layout shown in Fig. 2.6(c), the velocity of the vehicle is the same as that in Fig. 2.7.

The vehicle equipped with two AOWs is a redundantly driving system, which has no singular configuration. However, the velocity characteristics are altered when the wheel layout changes. Because the velocity of both AOWs must be the same when the vehicle travels along a direction, the wheel planes of AOWs are suggested to parallel to each other to obtain the maximum potential of the AOW. It is assumed that $l_{w1} = l_{w2} = l_w$, two AOWs can be arranged like the black points as shown in Fig. 2.8. The velocity of a single AOW is shown as the blue frame. Therefore, the velocity of the vehicle along the x - or y -axis directions is the same as that shown in Fig. 2.7. However, the rotation velocity ω_z takes the maximum value when the wheel plane is coplanar or the wheel axle is collinear because the circumferential velocity indicated by red lines that the AOWs should output can take the maximum value at these configurations.

Compared with the vehicle equipped with an AOW and omni wheel, the vehicle equipped with two AOWs does not show singularity, which leads to simplification of the control.

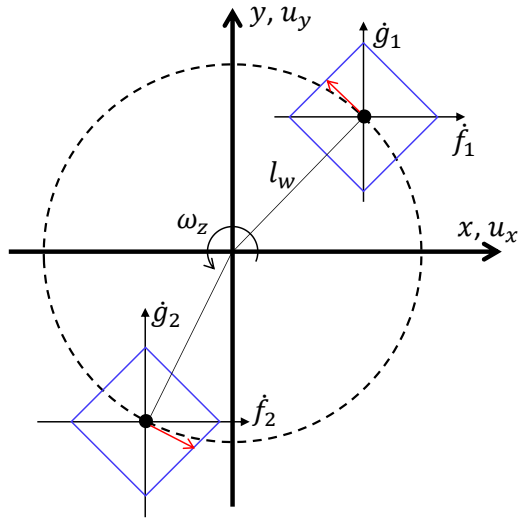


Fig. 2.8 Wheel layout and velocity distribution of vehicle equipped with two AOWs.

Based on the kinematics analysis, it is proved that the screw-theory-based method is feasible to solve the type synthesis issue of the wheeled locomotion vehicle.

2.5 Summary

The wheel composition was determined by the trial-and-error method according to mobility requirement, by which cannot derive the possible wheel composition of wheeled locomotion vehicle comprehensively and theoretically. To solve this problem, the screw-theory-based type synthesis

method was proposed to figure out the feasible wheel types, combinations, and layouts. The following results were obtained.

- A screw-theory-based method was proposed to synthesize the feasible wheel types and combinations comprehensively and theoretically according to the requirement of mobility by considering the wheel mechanism as the combination of revolute pairs and prismatic pairs.
- A kinematic modeling method based on the screw theory was proposed, based on which the kinematic characteristics of vehicles could be analyzed to obtain the feasible wheel layouts.
- An example of synthesizing the two-wheeled three-DOF vehicle was given to explain and verify the proposed method. The feasible wheel types, combinations, and layouts were obtained based on the proposed method. Their kinematic characteristics were analyzed based on the kinematic model.

Chapter 3

Type Synthesis of Six-DOF Mobile Parallel Mechanisms

3.1 Introduction

Wheeled mobile manipulators were proposed to solve the issue of workspace limitation of the conventional parallel mechanism with a fixed base. Wheeled mobile manipulators extend the motion range from the planar to the space, which makes it be able to complete relatively complex tasks. As introduced in Chapter 1, the mobile parallel manipulator contains two types. One is called VMPM where the parallel mechanism is mounted on the mobile base, the other one is called MPM which shares the driving sources with the mobile base as shown in Fig. 1.2(b) and (c), respectively. The position and orientation on the ground of the VMPM can be changed mainly by moving the mobile base. In this type, the output platform is controlled by different motors from those of the mobile base. Regarding the MPM, each driving unit is connected to a connecting chain. When the mobile base is powered by the driving units and moves on the ground, the entire MPM moves. When one of the driving units moves relative to the other driving units, the motion is transmitted via the connecting chain and the output platform performs spatial motions, namely the change in height or tilt. Therefore, both the movements of the entire MPM on the ground and the spatial motion of the output platform are powered by the same driving units. It is thought that the driving motors of MPM are utilized more effectively than that of VMPM. Additionally, it is notable that the stiffness of this MPM has proved to be higher than the conventional Stewart platform under some conditions [84]. Therefore, this study focuses on the MPM.

Type synthesis is one of the most important stages in the design of an MPM. However, previous studies about MPMs were very few and focused primarily on the kinematics and property analyses of the specified MPMs, and have rarely addressed their type synthesis of MPMs. Therefore, design solutions other than those used in existing MPMs could be developed. Many type synthesis methods have been proposed for conventional parallel mechanisms, such as the Lie subgroup synthesis method or the constraint synthesis method based on screw theory [85-86]. However, unlike the conventional parallel mechanisms those with fixed bases, an MPM is powered by several movable driving units [87]. As a result, even though the abovementioned method can be applied to the type synthesis of a connecting chain, it cannot be used in the type synthesis of an entire MPM structure, which means it is necessary to establish an alternative type synthesis method for MPMs.

With this in mind, this thesis proposes an MPM type synthesis method by using the screw theory based on the integration of a connecting chain and mobile base. To that end, possible structures are explored for six-DOF MPMs by first dividing those motions into three-DOF planar motions (realized by the planar motion of the mobile base) and three-DOF spatial motions (realized by the relative motions of the driving units through the connecting chains). As a result, the structures of the connecting chain for three-DOF spatial motion, and the mobile base for three-DOF planar motion, are enumerated separately based on their motion requirements. Then the connecting chain structure is discussed by considering two possible solutions: applying a singularity configuration and adding another constraining chain. The mobile base is synthesized for the planar motion requirement based on the method proposed in Chapter 2. Next, the method of integrating the connecting chain with the mobile base is discussed. Finally, feasible MPM structures are obtained based on the proposed type synthesis method, and four examples are provided to confirm its feasibility.

3.2 Type Synthesis Method for Mobile Parallel Mechanism

3.2.1 Conditions of Motion and Structure

As stated above, this chapter aims to find out the possible six-DOF MPM structures. Based on the idea that a symmetrical structure makes the design and control of the MPM easier in practical applications [58], an input-symmetrical MPM is set as the object of type synthesis. In this method, the number of the connecting chains is set to three, and pair compositions of all connecting chain and the driving units are the same, as shown in Fig. 3.1.

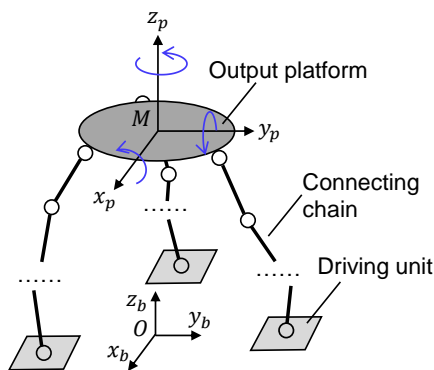


Fig. 3.1 Schematic description of an MPM with three connecting chains.

The MPM workflow proceeds as follows. First, the MPM moves to a specified location and then starts the required work. After finishing that job, the MPM moves to another location and continues. In such operations, the six-DOF mobility of the MPM is divided into the planar motion of the mobile base and the spatial motion of the output platform. Additionally, to achieve unlimited workspace, the mobile base must be able to move in any direction on the ground. Therefore, three-DOF planar

motion, including the two-DOF translation along the x_b - and y_b -axes and one-DOF rotation mobility around the z_b -axis, are necessary to permit the mobile base to change the position and orientation of the MPM. The three-DOF spatial motion of the output platform refers to translations along the z_p -axis and rotation around the x_p - and y_p -axes, which permit the end effector to access the target position and posture. Note that the coordinate systems $M-x_p y_p z_p$ and $O-x_b y_b z_b$ are fixed at the output platform center and on the ground, respectively, while the z_p - and z_b -axes are always perpendicular to the ground. The combination of the three-DOF planar motion and three-DOF spatial motion provides the MPM with six-DOF mobility.

Since all of the pairs included in the connecting chains are passive, the motions of the mobile base are applied as a unique driving source to achieve the motions of the output platform. The planar motions of the mobile base are considered to be directly equivalent to those of the output platform. The relative movements of the driving units are transmitted to the output platform through the connecting chain to vary its orientation and/or position. More specifically, the motions of the driving units are transmitted to achieve the planar or spatial motion of the output platform. Therefore, the synthesis of MPM is divided into those of connecting chain and mobile base separately.

Generally, the control of the MPM becomes easy if the spatial motion is decoupled with the planar motion. Namely, the relative motions of the driving units affect the spatial motions of the output platform but do not change the position of the whole MPM when the MPM is located at a specified position.

3.2.2 Synthesis Method and Process

A screw-theory-based type method is proposed for the type synthesis of the MPM. All kinds of pairs can be seen as equivalent to the combination of one or more revolute and prismatic pairs. Additionally, the mobile base of an MPM can be considered equivalent to a planar parallel mechanism when its wheels are regarded as the combination of lower pairs in the chain. Therefore, the structures of the connecting chain and mobile base in an MPM can be obtained by the similar synthesis method proposed in Chapter 2. As discussed in Section 3.2.1, after dividing the mobility of the MPM into the mobility of the output platform and that of the mobile base, the type synthesis of the connecting chain and the mobile base is performed separately. Meanwhile, the geometric relationship between pairs during the synthesis of connecting chain can be obtained via the reciprocal screw rules. For example, to form a zero-pitch wrench on the output platform that is perpendicular to the ground, all of the passive prismatic pair axes should be parallel to the ground, while the revolute pair axes should be coplanar with the zero-pitch wrench. By considering these conditions, the pair composition for the connecting chain or driving unit structure can be obtained. Finally, the MPM structure is obtained by integrating the type synthesis results of the connecting chain with

those of the mobile base. Summarizing the above, our proposed MPM type synthesis process is as shown in Fig. 3.2.

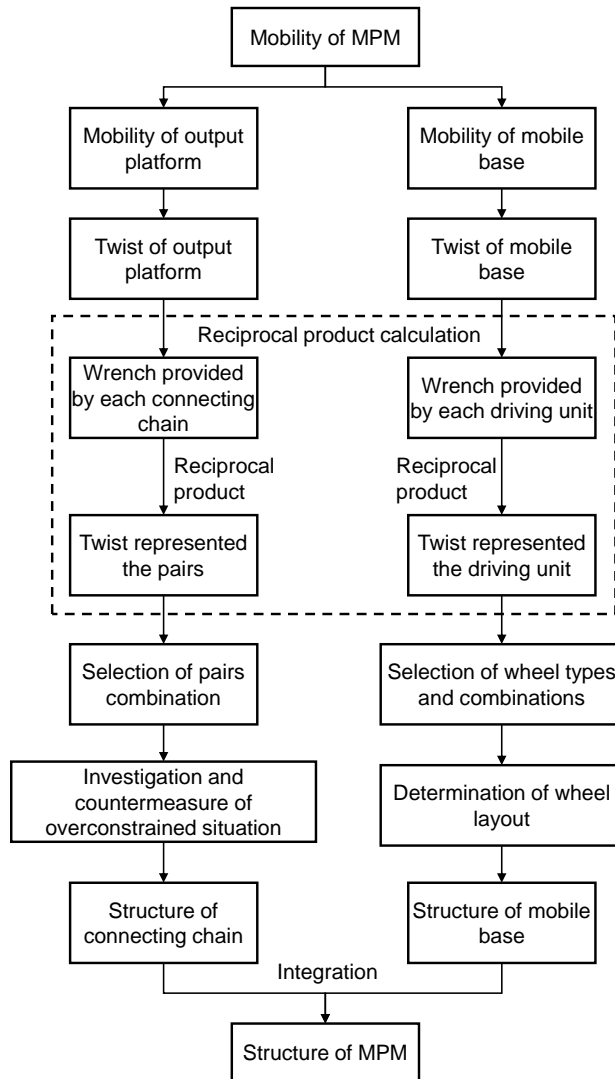


Fig. 3.2 MPM type synthesis flowchart.

3.3 Type Synthesis of Connecting Chain

As discussed in Section 3.2.1, the connecting chains must facilitate the mobility of rotation around the x_p - or y_p -axis and translation along z_p -axis (RxRyTz) to the output platform when the driving units move in the appropriate directions. The RxRyTz mobility of the output platform can be represented by a three-system twist composed of an infinite-pitch screw and two zero-pitch screws, in which the axis of the infinite-pitch screw is perpendicular to that of the zero-pitch screws. In this configuration, the possible wrench system provided by each connecting chain can be a one-, two-, three-, or zero-system, as shown in Fig. 3.3. When the wrench system is a one-system, it contains

only one zero-pitch wrench. When the wrench system is a two-system, it is composed of pure zero-pitch wrenches or one zero-pitch wrench and one infinite-pitch wrench. When the wrench system is a three-system, it is formed by one infinite-pitch wrench and two zero-pitch wrenches. When the wrench is a zero-system, it means each connecting chain acts no wrench on the output platform. Regardless of which of the above wrench systems is used, the axis of any infinite-pitch wrench must be perpendicular to the axes of zero-pitch wrenches provided by the same connecting chain.

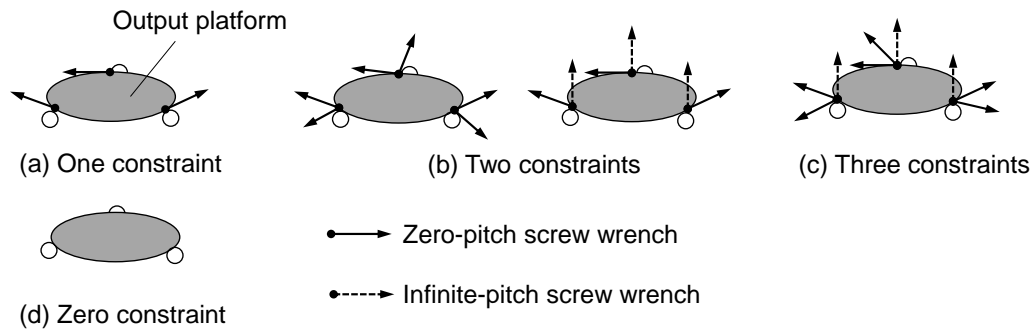


Fig. 3.3 Possible constraints imposed on the output platform.

Based on the above analysis, two solutions are considered to realize such spatial motions of the output platform. One is realizing motions under a singular configuration with respect to the situation shown in Fig. 3.3(a), (b), and (c). The singular configuration is caused if the wrench acted by the connecting chain is also reciprocal to the equivalent pair screw representing the motion of the driving unit. Then the motions other than the $RxRyTz$ motion are restricted when the driving unit moves or rotates. Therefore, at least one zero-pitch wrench of each connecting chain must be in parallel with the ground to ensure that the wrench is also reciprocal to the equivalent pair screw representing the specified motion of the driving unit under this situation. The other is using an additional connecting chain that acts as three wrenches to the output platform with respect to the situation shown in Fig. 3.3(d), which can limit the undesired motion. Both solutions will be discussed separately in this section. The former and latter methods are discussed in Sections 3.3.1 and 3.3.2, respectively.

3.3.1 Applying Singularity Configuration

Under the singularity configuration discussed here, the six-DOF mobility of the MPM is limited to the $RxRyTz$ motion. The possible connecting chain structures for the $RxRyTz$ mobility are enumerated and discussed below.

3.3.1.1 Enumeration of Connecting Chains

3.2.1.1.1 Chain with One Constraint

When each chain provides just one zero-pitch wrench to the output platform, as shown in Fig. 3.3(a), the screws of each chain form a five-system twist, which means the maximum number of the independent one-DOF pair screws is five. Additionally, based on Rule A3 in Chapter 2, the number of revolute pairs in each chain is more than three. Revolute pair (R) and prismatic pair (P) are applied as the fundamental pairs because all other pairs can be equivalent to their combinations. At this point, the composition possibilities of each chain are 5R, 4R1P, or 3R2P. Because there is no infinite-pitch screw in the chain wrench system, the axes of more than three revolute pairs in each chain are non-coplanar. It is possible that situations can occur in which any two axes of the three revolute pairs do not intersect at a point, or in which two axes intersect at the same point, but the remaining axis does not pass through that point, or in which all axes intersect at the same point. For simplicity, it is assumed that the axes of the revolute pairs satisfy the latter two geometrical conditions. In general, each of the revolute pair axes should remain on the same plane as the reciprocal screw, while each prismatic pair axis should be perpendicular to that of the reciprocal screw.

Considering the above conditions, the possible chain structures are shown in Fig. 3.4, where new structures are obtained if the order of the pairs is altered properly. The screw $\$i$ indicated by a dashed line represents the axis of the i -th pair. The screw $\$r$ indicated by a red line refers to a wrench that is unique to the chain twist system. Here, \underline{RR} refers to the axes of revolute pairs that intersect at a point, \overline{RR} means the axes of these revolute pairs that are in parallel, $R_{\perp P}$ refers to the axis of a revolute pair that is perpendicular to that of the neighboring prismatic pair, while $P_{\perp R}$ indicates the opposite configuration. However, the structures shown in Fig. 3.4(b), (d), and (g) are inappropriate because the direction of the one-system wrench must be in parallel with the ground.

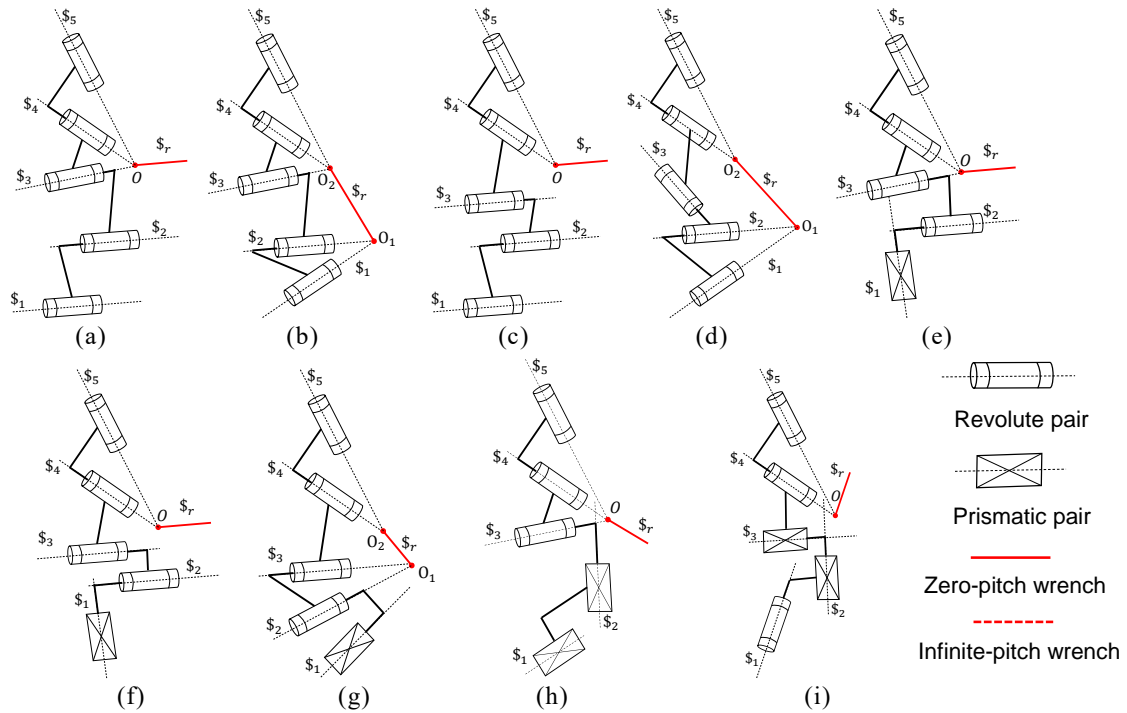


Fig. 3.4 Possible connecting chain structures with one force constraint. (a) \overline{RRRRR} , (b) $\underline{RR} \underline{RRR}$, (c) $\underline{RRR} \underline{RR}$, (d) \underline{RRRRR} , (e) $\underline{P}_{1R} \underline{R}_{1P} \underline{RRR}$, (f) $\underline{P} \underline{R}_{1P} \underline{R}_{1P} \underline{RR}$, (g) $\underline{PRR} \underline{RR}$, (h) \underline{PPRRR} , and (i) $\underline{RP}_{1R} \underline{P}_{1R} \underline{RR}$.

3.2.1.1.2 Chain with Two Constraints

When the chain wrench system is a two-system, as shown in Fig. 3.3(b), the chain twist system is composed of four independent one-DOF pairs. When the wrench system is composed of two zero-pitch wrenches, the maximum number of prismatic pairs in the connecting chain is one. Additionally, two or three of the revolute pairs should intersect at a common point to ensure there is no infinite-pitch screw in the chain wrench system. The reciprocal screws should pass through the intersection point. If they do not, they are either in the same plane as the remaining revolute pair or are perpendicular to the prismatic pair. Therefore, the composition possibilities of each chain are 4R and 3R1P, as shown in Fig. 3.5. Note that $\$_{r2}$ in Fig. 3.5(b) is on the intersection line of the plane formed by $\$_1$ and $\$_2$ and the plane formed by $\$_3$ and $\$_4$. However, the structure in Fig. 3.5(b) is unsuitable because it is unable to keep the one of the wrench direction being stably in parallel with the ground.

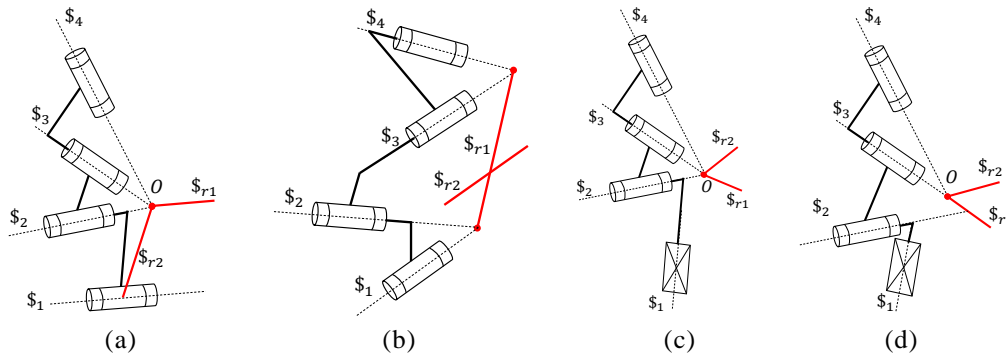


Fig. 3.5 Possible connecting chain structures with two force constraints. (a) \underline{RRRR} , (b) $\underline{RR RR}$, (c) \underline{PRRR} , and (d) \underline{PRRR}

When the chain wrench system is a two-system composed of an infinite-pitch wrench and a zero-pitch wrench, the maximum number of axis-intersected revolute pairs in the connecting chain must be two to ensure there is one infinite-pitch screw in the chain wrench system. The remaining revolute pairs must be in parallel with one of the axis-intersected revolute pairs, while the prismatic pair axes should be perpendicular to the zero-pitch reciprocal screw, as stipulated by Rules A2 and A3 in Chapter 2. Therefore, the composition possibilities of each chain are 4R, 3R1P, and 2R2P, as shown in Fig. 3.6.

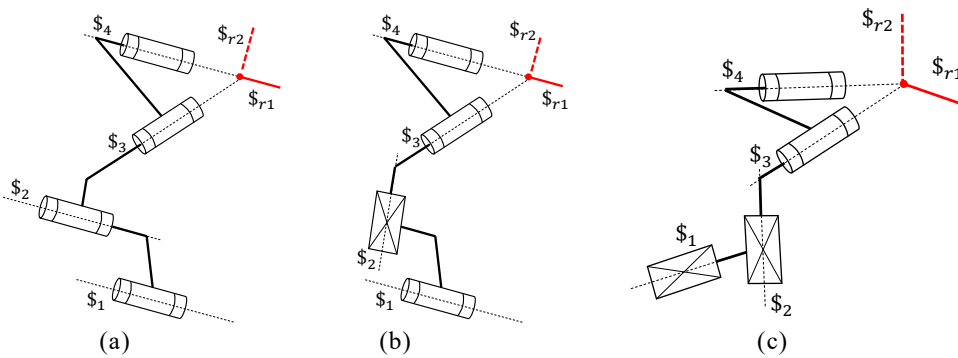


Fig. 3.6 Possible chain structures with two constraints composed of a force and a couple constraint. (a) \underline{RRRR} , (b) $\underline{R_{\perp P_{\perp}}RR}$, and (c) \underline{PRRR} .

3.2.1.1.3 Chain with Three Constraints

When the chain wrench system is a three-system, as shown in Fig. 3.3(c), the chain twist system is composed of three independent one-DOF pairs, and the maximum number of prismatic pairs in the connecting chain is one to ensure there are two zero-pitch screws in the chain wrench system. Therefore, the composition possibilities of the connecting chain are 3R and 2R1P, as shown in Fig. 3.7. The axes of intersected revolute pairs reside in a horizontal plane, while the axis of the remaining revolute pair is in parallel with one of the axis-intersected revolute pairs shown in Fig. 3.7(a), and the axis of the remaining prismatic pair is perpendicular to that horizontal plane, as shown in Fig. 3.7(b).

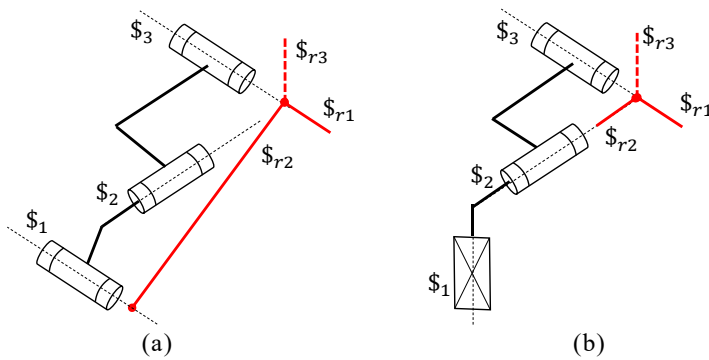


Fig. 3.7 Possible connecting chain structures with three constraints. (a) RRR and (b) PRR.

3.3.1.2 Analysis of the Enumerated Chain Structures

According to Gruebler's equation, when each connecting chain imposes one, two, or three constraints on the output platform, the DOFs of the MPM (excluding the mobile base) are 3, 0, and -3, respectively. This result indicates that using chain structures with three constraints to construct a six-DOF MPM is unfeasible, even though the other two structure types could potentially realize the desired MPM mobility by integrating them with the driving unit.

On the other hand, the above DOF evaluation is based on the assumption that there is no overconstraint. An overconstrained mechanism is one that has more DOFs in the actual motion than are given by Gruebler's equation. Next, the enumerated structures are analyzed while considering overconstrained characteristics. In general, an overconstrained condition occurs when pair axes are in specified relationships, such as when the axis of a prismatic pair in a connecting chain is in parallel with those in other chains, when the axes of the revolute pair are collinear with each other among three connecting chains, when the axes of all revolute pairs intersect at a common point, and so on. In the MPM discussed here, the conditions related to revolute pairs are not always satisfied due to the three-fold symmetric structure of the entire MPM and the motion constraints of the enumerated chain structures. Nevertheless, the condition regarding the prismatic pair can be satisfied in some situations, as will be discussed below.

If only one constraint is imposed on the output platform by each connecting chain, the overconstrained mechanism exists at the structures shown in Fig. 3.4(e), (f), (h), and (i) when the axis of the prismatic pair is perpendicular to the ground. For the structures shown in Fig. 3.4(e) and (f), the overconstrained issue is easily solved when the axis of the prismatic pair is in parallel with the ground. With regards to the structures shown in Fig. 3.4(h) and (i), the overconstrained issue cannot be solved unless one prismatic pair axis is arranged obliquely. However, in Fig. 3.4(i), it can be seen that the angle of the prismatic pair in relation to the ground cannot be fixed due to the revolute pair, which means that the overconstrained configuration changes during operation, which is unacceptable for an MPM.

When two constraints are imposed on the output platform by each connecting chain, the overconstrained mechanism exists at the structures shown in Figs. 3.5(c), 3.5(d), 3.6(b), and 3.6(c) when the prismatic pair is perpendicular to the ground. For the structures shown in Fig. 3.5(c) and (d), the overconstrained issue is also solved if the axis of the prismatic pair is set obliquely. The structure shown in Fig. 3.6(b) permits the angle of the prismatic pair relative to the ground to be changeable due to the revolute pair, which means that the overconstrained characteristics can vary. Hence, this structure is also unsuitable for use by an MPM. As for the structures shown in Fig. 3.6(c), at least one prismatic pair should be arranged obliquely to avoid the overconstrained situation.

In the case of the connecting chain with three constraints, the structure shown in Fig. 3.7(b) produces the overconstrained mechanism when the prismatic pair is vertical. However, even when the overconstrained situation occurs, the available DOFs obtained are not sufficient to construct an MPM.

3.3.2 Using Additional Connecting Chain to Limit Undesired Motion

Since the output platform has six-DOF mobility if the connecting chains do not impose any wrench on it as shown in Fig. 3.3(d), it is possible to realize the RxRyTz motion by constraining other undesired motions with an additional chain. First, the possible connecting chain structure that imposes no constraint on the output platform is discussed below. In this case, the number of the revolute pairs is more than three because no infinite-pitch wrench is imposed on the output platform. Therefore, the composition possibilities of the connecting chain are 6R, 5R1P, 4R2P, and 3R3P. Additionally, since three revolute pairs must intersect at a point to ensure there is no infinite-pitch wrench, the remaining pairs are arranged to ensure they do not create a zero-pitch wrench. Considering these conditions, the possible connecting chain structures are shown in Fig. 3.8. With regards to the structures shown in Fig. 3.8(a) and (b), the unique reciprocal screw of the two intersected revolute pair sets ($\$2$ and $\$3$; $\$4$, $\$5$, and $\$6$) passes through points O_1 and O_2 . If the last revolute pair is not coplanar with line O_1O_2 , as shown in Fig. 3.8(a), or if it is not perpendicular to the prismatic pair shown in Fig. 3.8(b), there is no screw reciprocal to the chain twist. With regards to the structure shown in Fig. 3.8(c), the screw reciprocal to the four revolute pair screws exists in the plane formed by point O and the axis of pair $\$3$. If the axis of the remaining prismatic pair is not perpendicular to that plane, there is no wrench imposed on the output platform. With regards to structures shown in Fig. 3.8(d), the three prismatic pairs axes are not coplanar, which means there is no zero-pitch wrench constraining the output platform.

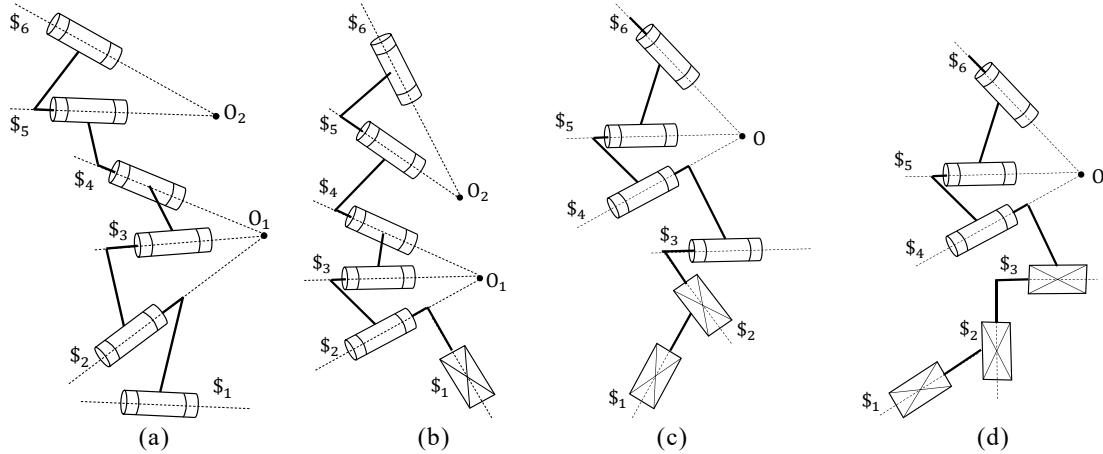


Fig. 3.8 Possible connecting chain structures with six-system twist. (a) $\underline{RRRR} \underline{RR}$, (b) $\underline{PRRR} \underline{RR}$, (c) \underline{PPRRRR} , and (d) \underline{PPRRRR} .

Next, the additional connecting chain, which is required to impose three constraints on the output platform, is discussed. The structural possibilities of this additional chain are the same as those shown in Fig. 3.7. However, with regards to the structure shown in Fig. 3.7(a), the direction of the wrench $\$_{r2}$ changes from instant to instant when the revolute pair $\$1$ rotates. Therefore, only the structure shown in Fig. 3.7(b) is suitable for use as the additional chain.

Finally, the DOF of this type of solution is analyzed. Without the overconstrained situation, the MPM with three connecting chains and one additional chain (excluding the mobile base) has three DOFs. The overconstrained mechanism exists at the structures shown in Fig. 3.8(b), (c), and (d), providing a prismatic pair axis is perpendicular to the ground. To avoid this overconstrained situation, the prismatic pairs should be arranged in parallel with or obliquely to the ground.

3.4 Type Synthesis of Mobile Base

In this section, the possible structures of the mobile base are obtained based on the synthesis method proposed in Chapter 2. Here, the mobile base is seen as a virtual planar parallel mechanism composed of three driving units.

3.4.1 Mobility Analysis

Since the position and orientation of the mobile base need to be changeable to solve the limited workspace problem and achieve the spatial motion of the output platform, both three-DOF planar motion and three-DOF relative motion are necessary to achieve six-DOF mobility for the mobile base. Hence, the mobile base twist system for the former motion is written by

$$\begin{cases} \hat{\xi}_1 = [0 & 0 & 1 & 0 & 0 & 0] \\ \hat{\xi}_2 = [0 & 0 & 0 & 1 & 0 & 0] \\ \hat{\xi}_3 = [0 & 0 & 0 & 0 & 1 & 0] \end{cases} \quad (3.1)$$

In Eq. (3.1), $\hat{\xi}_1$, $\hat{\xi}_2$, and $\hat{\xi}_3$ represent the rotation around the z_b axis, translation along the x_b axis, and translation along the y_b axis, respectively, referring to the coordinate system shown in Fig. 3.1. Therefore, the twist of each driving unit also can be written by one of the following screws or a linear combination of them by the same process explained in Chapter 2:

$$\begin{cases} \hat{\xi}_1^t = [0 & 0 & 1 & 0 & 0 & 0] \\ \hat{\xi}_2^t = [0 & 0 & 0 & 1 & 0 & 0] \\ \hat{\xi}_3^t = [0 & 0 & 0 & 0 & 1 & 0] \end{cases} \quad (3.2)$$

Since the total number of the actuators is normally equal to the DOFs of the MPM, the input-symmetric structures require two active DOFs for each driving unit. Therefore, the driving unit twist is either a two- or a three-system. In the two-system case, the driving unit twist is divided into two types. One is the linear combination of $\hat{\xi}_1^t$ with $\hat{\xi}_2^t$ or $\hat{\xi}_3^t$, which represents the rotation about the z_b axis and translation along the x_b - or y_b -axis direction, while the other is the linear combination of $\hat{\xi}_2^t$ with $\hat{\xi}_3^t$, which represents the translation along x_b - and y_b -axis directions. On the other hand, the three-system twist is also feasible if only two twist motions are active and the third is passive.

3.4.2 Type Synthesis of Driving Unit

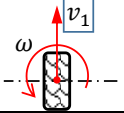
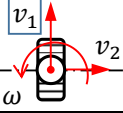
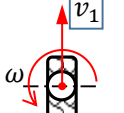
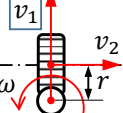
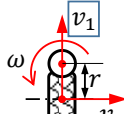
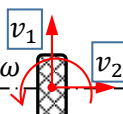
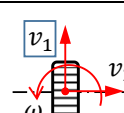
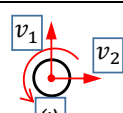
In this section, the type synthesis of the driving unit is discussed in relation to the number of wheels.

3.4.2.1 Driving Unit with One Wheel

As introduced in Chapter 1 and Chapter 2, various wheel mechanisms have been reported in previous studies. All types of wheels can be equivalent to the combination of a revolute pair and one or two prismatic pairs. Although the regular omni wheel or Mecanum wheel only has one active DOF, they become actively orientable when a steering axis is added mechanically. The AOW can perform active translations in two directions. The typical spherical wheel, which is equivalent to one active revolute pair and two active prismatic pairs, has three active DOFs.

Wheel motions can be expressed by screws, as shown in Table 3.1. The actuatable motion of the typical configuration is denoted by the blue frame in the figure. All wheels, except for the fixed wheel and the simple omni wheel or Mecanum wheel, can obtain at least two active DOFs. Therefore, based on the above discussion, they can even function as driving units by themselves. However, it should be noted that only two DOFs of the spherical wheel can be active when it is used to form a driving unit.

Table 3.1 Mobility of wheel mechanism represented by screw.

Wheel mechanism	Mobility	Unit twist screw	Wheel mechanism	Mobility	Unit twist screw
Fixed wheel		$\begin{bmatrix} 0 & 0 & 1 & 0 & 0 & 0 \\ 0 & 0 & 0 & 1 & 0 & 0 \end{bmatrix}$	Centered orientable omni wheel		$\begin{bmatrix} 0 & 0 & 1 & 0 & 0 & 0 \\ 0 & 0 & 0 & 1 & 0 & 0 \\ 0 & 0 & 0 & 0 & 1 & 0 \end{bmatrix}$
Centered orientable wheel		$\begin{bmatrix} 0 & 0 & 1 & 0 & 0 & 0 \\ 0 & 0 & 0 & 1 & 0 & 0 \end{bmatrix}$	Off-centered orientable omni wheel		$\begin{bmatrix} 0 & 0 & 1 & r & 0 & 0 \\ 0 & 0 & 0 & 1 & 0 & 0 \\ 0 & 0 & 0 & 0 & 1 & 0 \end{bmatrix}$
Off-centered orientable wheel		$\begin{bmatrix} 0 & 0 & 1 & r & 0 & 0 \\ 0 & 0 & 0 & 1 & 0 & 0 \\ 0 & 0 & 0 & 0 & 1 & 0 \end{bmatrix}$	Active omni wheel		$\begin{bmatrix} 0 & 0 & 1 & 0 & 0 & 0 \\ 0 & 0 & 0 & 1 & 0 & 0 \\ 0 & 0 & 0 & 0 & 1 & 0 \end{bmatrix}$
Omni wheel		$\begin{bmatrix} 0 & 0 & 1 & 0 & 0 & 0 \\ 0 & 0 & 0 & 1 & 0 & 0 \\ 0 & 0 & 0 & 0 & 1 & 0 \end{bmatrix}$	Spherical wheel		$\begin{bmatrix} 0 & 0 & 1 & 0 & 0 & 0 \\ 0 & 0 & 0 & 1 & 0 & 0 \\ 0 & 0 & 0 & 0 & 1 & 0 \end{bmatrix}$

3.4.2.2 Driving Unit with Two Wheels

Next, the structure of a two-wheeled driving unit is discussed. First, it is assumed that each wheel has only one active DOF. In this situation, the wheels, ground, and chassis of the driving unit form a closed-loop mechanism that has two chains. When the driving unit is equipped with two fixed wheels, each wheel is equivalent to the combination of a passive revolute pair and an active prismatic pair, as shown in Fig. 3.9. The pair revolving around the axis perpendicular to the ground is defined as screw ξ_i^z , while screw ξ_i^y represents the prismatic pair along the wheel plane. The index i represents wheel i and $i = 1, 2$. Each wheel chain forms a four-system wrench to the chassis, which is composed of two zero-pitch screws (ξ_i^{w1} and ξ_i^{w2}) shown as red solid lines, and two infinite-pitch screws (ξ_i^{w3} and ξ_i^{w4}) shown as red dashed lines.

The twist screw of the chassis can be obtained by calculating the reciprocal product of the abovementioned wrench screws. When the axles of the wheels intersect at a point, as shown in Fig. 3.9(a), there is only one twist screw ξ_D^t that is reciprocal to the wrench system. This indicates that the driving unit is only able to rotate about the axis perpendicular to the ground. When the wheel axles are lying on the same line, as shown in Fig. 3.9(b), two twist screws (ξ_D^{t1} and ξ_D^{t2}) can be obtained by the reciprocal product. This indicates that the driving unit can not only rotate about the vertical axis but also travel along the direction in parallel with the wheel planes. Therefore, to obtain the two-DOF mobility when the driving unit is equipped with two fixed wheels, the wheel axles should be collinear.

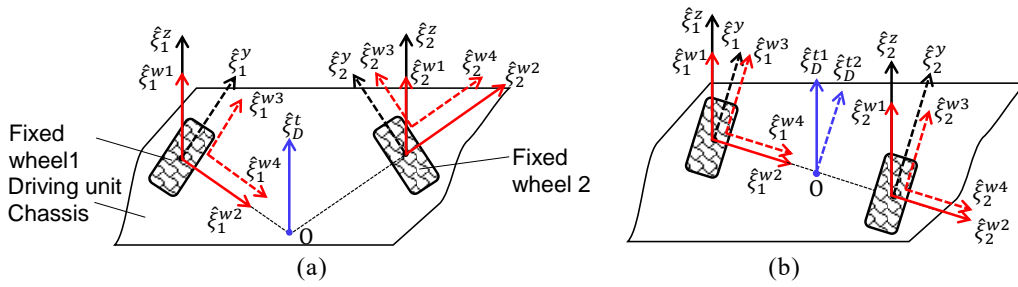


Fig. 3.9 Screws formed in driving units with two fixed wheels. (a) Intersection arrangement, (b) Collinear arrangement.

When a driving unit is equipped with two centered orientable wheels, the wrench system provided by the wheels at each instant is similar to that provided by fixed wheels. However, unlike a fixed wheel, a center orientable wheel is steerable, which means the wrench system provided by the wheels changes from moment to moment. For example, when both wheels are rotated actively, the driving unit can rotate around the steering axis of wheel 2 under the situation shown in Fig. 3.10(a), while it can travel along the wheel plane direction in the situation shown in Fig. 3.10(b). However, in this case, the steering of the wheels should be passive due to the assumption that each wheel has one active DOF, which means that switching between Figs. 3.10(a) and (b) conditions is involuntary. Hence, this configuration is unsuitable.

On the other hand, this problem can be solved when wheel 1 is actively steerable, and wheel 2 rotates actively. In such cases, excluding the situation shown in Fig. 3.10(a), the driving unit can perform a translation when the wheel planes are in parallel with each other, as shown in Fig. 3.10(b), and perform a circular motion when the wheel planes are oblique to each other. This means that wheel 2 does not need to be orientable. Therefore, a centered orientable wheel should be combined with a fixed wheel to form a driving unit in the same manner as a driving unit with an off-centered orientable wheel.

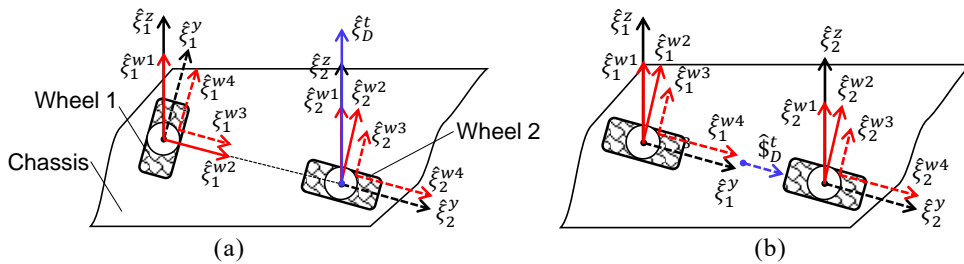


Fig. 3.10 Screws formed in driving units with two centered orientable wheels. (a) Intersection arrangement, (b) Parallel configuration.

When a driving unit is equipped with two omnidirectional wheels that have three DOFs, such as an omni wheel, the twist screw system representing the wheel contains a zero-pitch screw ξ_i^z and two infinite-pitch screws ξ_i^x and ξ_i^y . The wrench system provided by each wheel chain is a three-system containing three independent screws shown by red lines in Fig. 3.11. By calculating the

reciprocal product of the wrench system formed by both wheels, the mobility of the driving unit is given by ξ_D^{t1} , ξ_D^{t2} , and ξ_D^{t3} , as shown by the blue line in the figure. This figure also shows that the driving unit has three DOFs that contain one rotation and two translations. However, since one of three DOFs becomes uncontrollable due to the passive motion represented by the infinite-pitch screw ξ_i^x , one of the omnidirectional wheels must be replaced with a fixed wheel to form a driving unit.

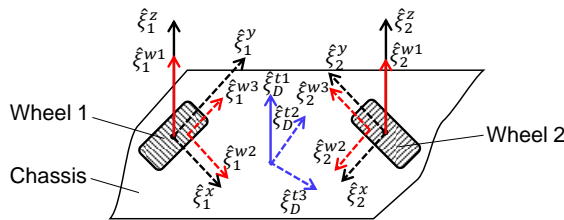


Fig. 3.11 Screws formed in driving units with two omnidirectional wheels.

Based on the method introduced in Chapter 2, the wheel layouts can be determined when the driving unit is formed by two wheels. Therefore, the possible driving unit structures are shown in Fig. 3.12. They are composed of either a single wheel, such as the centered orientable wheel, or two wheels, such as two independent drive fixed wheels. According to the above discussion, driving units can be divided into two types. The first, of which there are two types, is equivalent to the combination of two active prismatic pairs and includes a single active omni wheel, as shown in Fig. 3.12(e), and a spherical wheel, as shown in Fig. 3.12(f). The second, of which there are eight types, combines active revolute and prismatic pairs. Both structures enable the mobile base to realize both three-DOF planar and three-DOF relative movements.

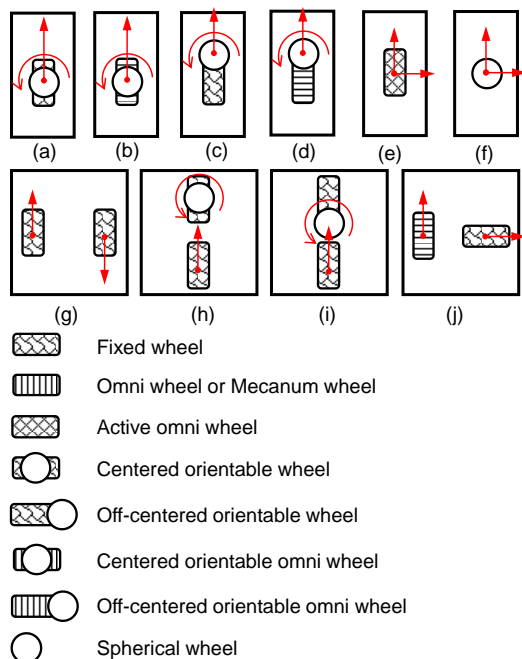


Fig. 3.12 Possible driving unit structures.

3.5 Integration of Connecting Chain and Mobile Base

In this section, the integration methods of the connecting chain and mobile base are discussed, and the MPMs are synthesized.

3.5.1 Connecting Scheme

As analyzed in Section 3.2, some of the enumerated connecting chain structures bring redundant DOFs to the MPM. These are the one-constraint chain with or without overconstraint, the two-constraint chain with or without overconstraint, and the no-constraint chain with or without overconstraint. To construct an MPM properly, such redundant DOFs must be constrained but kept movable at the same time. To address this issue, the appropriate number of pairs in the connecting chains are made activate by using the driving units.

When each connecting chain imposes only one constraint on the output platform without overconstraint, the end pair of each connecting chain can be actuated by the driving unit. Then, the posture of the output platform is uniquely decided by the input motions of the three driving units. If an overconstraint situation occurs, the redundant DOFs exceed three, at which point they can no longer be actuated by the three driving units. Therefore, a one-constraint chain with overconstraint is unsuitable for use by the MPM.

When each connecting chain imposes two constraints on the output platform without overconstraint, the equivalent pair screws representing the motions of the driving units should be reciprocal to at least one of the wrenches. If the equivalent pair screw is reciprocal to just one of the wrenches, the wrench imposed on the output platform is reduced from two to one by the addition of the driving unit. In this situation, activation is unnecessary, and the connecting chain is only required to connect with the driving unit. If the equivalent pair screw is reciprocal to both wrenches, it is regarded as a surplus pair in the chain and prevents the input motion of the driving unit from converting into the spatial motion of the output platform. At this time, the end pair of the connecting chain must be actuated by the driving unit. The end pair must also be actuated when the connecting chains constitute an overconstrained mechanism.

When no constraint is imposed on the output platform, an additional connecting chain is added to limit the undesired motions. Without overconstraint, the three connecting chains, excluding the additional chain, are needed to join with the driving unit, and the end pair must be actuated. With overconstraint, the redundant DOF exceeds the capability of the driving units, and the MPM cannot be constructed.

Based on the above analysis, the connecting chain structures are divided into Groups A, B, and C. For the structures in Groups A and C, it is necessary to use the motion of the driving unit to actuate the end pair of the connecting chain, which means the vertical rotation axis or horizontal

moving direction of driving unit should be converted to be consistent with the rotation axis or translation direction of the end pair. In contrast, for the Group B structures, it is only necessary to join the driving unit with the connecting chain directly, where the transmission mechanism between the driving unit and end pair is unnecessary. The enumerated types of connecting chain structures are summarized and classified in Table 3.2.

Table 3.2 Summary of the enumerated connecting chain structures.

Method	Constraint situation	Structure	Classification
Applying singularity configuration	One constraint (without overconstraint)	Fig. 3.4(a), (c), (e), (f),and (h)	Group A
	Two constraints (with overconstraint or wrench overlap)	Fig. 3.5(c) and (d); Fig. 3.6(a) and (c)	
	Two constraints (without overconstraint)	Fig. 3.5(a), (c), and (d); Fig. 3.6(a) and (c)	Group B
Using additional connecting chain	No constraint (without overconstraint)	Fig. 3.8(a), (b), (c), and (d)	Group C

3.5.2 Actuating Mechanism

As discussed in the previous section, the motion of driving units should be transmitted to the end pairs of the connecting chain in Groups A and C. The mobility of the driving unit is composed of either two planar translations or translation and rotation. Therefore, the translation or rotation motion of the driving unit must be capable of being used as the driving source to power the end pair of the connecting chain. When the end pair is a prismatic pair, its sliding direction is assumed to be either in parallel with or perpendicular to the ground. Note that, the transmission is unnecessary when the sliding direction of end pair is in parallel with the ground, because it can be arranged to be same with translation direction of the driving unit. When the end pair is a revolute pair, its axis is assumed to be in parallel with the ground. This is because if the end pair axis is perpendicular to the ground, the zero-pitch wrench formed by the connecting chain must be perpendicular to the ground as well. However, the output platform would be unable to translate along the vertical direction under this condition. Therefore, it is necessary to consider a transmission mechanism to convert the rotation or translation of the driving unit to the revolute pair or prismatic pair of the connecting chain. Examples of the transmission mechanisms according to the configuration of the end pair are shown in Fig. 3.13. The transmission mechanism, such as bevel gear, worm drive, orthogonal double-slider mechanism, rack and pinion, and helical transmission, is used to change motion direction or motion form.

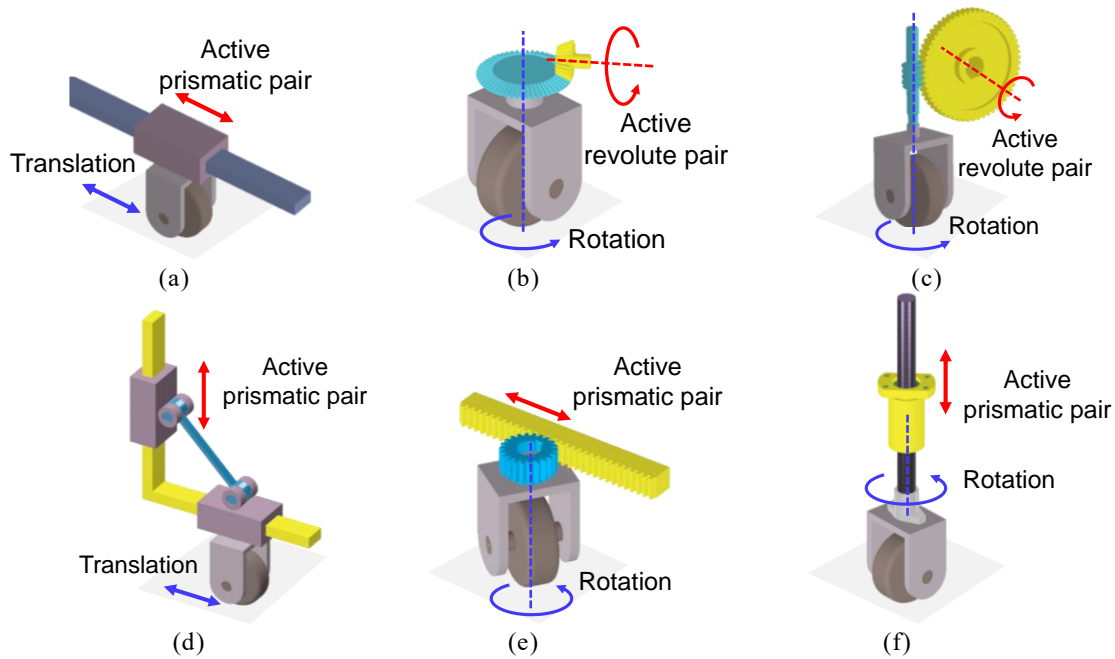


Fig. 3.13 Examples of transmission mechanisms between driving unit and connecting chain. (a) Direct drive, (b) Bevel gear mechanism, (c) Worm drive mechanism (d) Orthogonal double-slider mechanism, (e) Rack and pinion, and (f) Helical mechanism.

The possible actuating mechanisms for the driving unit to drive the end pair of the connecting chain are summarized in Table 3.3 based on the end pair configurations and the input motion of the driving unit. For example, when the translation motion of the driving unit is applied as the driven source, the orthogonal double-slider mechanism is used to change the motion direction if the end pair is a vertical prismatic pair. Alternatively, when the rotation motion of the driving unit is applied to drive the vertical prismatic pair, the helical mechanism is used to change the rotation motion to the translation motion.

Table 3.3 Driving unit actuating mechanisms

End pair type of connecting chain	Feasible motion of driving unit		Corresponding connecting chain structure
	Translation	Rotation	
Prismatic pair (parallel to the floor)	Driving directly	Rack and pinion	Fig. 3.4(e), (f), and (h); Fig. 3.8(b), (c), and (d)
Prismatic pair (perpendicular to the floor)	Orthogonal double-slider mechanism	Helical mechanism	Fig. 3.5(c) and (d); Fig. 3.6(c)
Revolute pair (parallel to the floor)	Rack and pinion	Bevel gear, worm drive	Fig. 3.4(a) and (c); Fig. 3.6(a); Fig. 3.8(a)

Overall, there are 13 feasible connecting chain structures for Groups A and C. For each structure, ten and eight types of the driving unit can feasibly use translation motion and rotation motion, respectively, to actuate the end pair of the connecting chain. Hence, the number of the possible

structures for the MPM in Group A is $13 \times 18 = 234$. On the other hand, five types of connecting chain structures and ten types of driving units are feasible for Group B, which means it has $5 \times 10 = 50$ possible structure combinations for the MPM. Therefore, there are 284 types of MPM structures in total based on the proposed type synthesis method.

3.5.3 Examples of Mobile Parallel Manipulator

Based on the above integration method, several novel MPM structures are obtained. One example of an MPM with one chain constraint, which integrates the connecting chain shown in Fig. 3.4(e) with the driving unit shown in Fig. 3.11(a), is shown in Fig. 3.14. The connecting chain structure, which is composed of a prismatic pair, a revolute pair, and a spherical pair, is classified as belonging to Group A. The centered orientable wheels, where the orientation and the rotation of the wheel are active, are applied as the driving units. The end prismatic pair is directly actuated by the translation motion of the driving unit. When the driving units travel along the rail, the spatial motion of the output platform is achieved. The steering and rotation of the driving unit are controlled to realize the planar motions of the output platform. Therefore, this proposed MPM can achieve six-DOF motion.

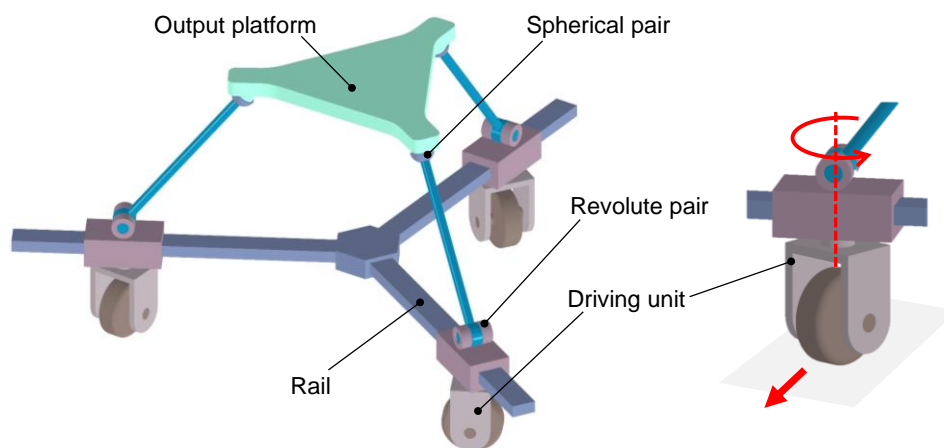


Fig. 3.14 3-PRS MPM.

Fig. 3.15 shows another example of Group A, in which the connecting chain shown in Fig. 3.6(a) is integrated with the driving unit shown in Fig. 3.12(g). A worm drive mechanism is used as the transmission mechanism to change the vertical rotation motion of the driving unit into the horizontal rotation motion of the end revolute pair. Two revolute pairs and one universal pair provide the link that connects the gear axis and the output platform. When the driving units rotate at a fixed location, the rotation direction is altered and transmitted to produce the spatial movement of the output platform. Meanwhile, the cooperative motions of the driving units make it possible for the entire MPM to move to any location. Therefore, this mechanism also functions as a six-DOF MPM.

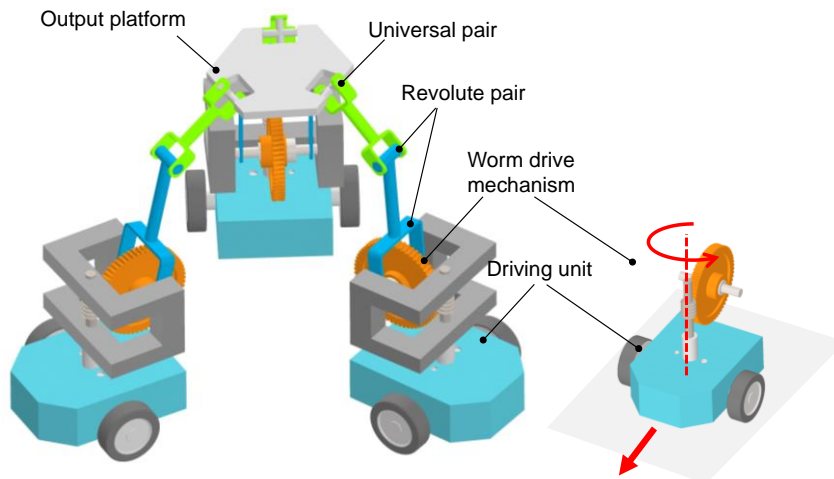


Fig. 3.15 3-RRU MPM.

Fig. 3.16 shows an example of MPM that integrates the connecting chain in Group B as shown in Fig. 3.5(a) with the driving unit shown in Fig. 3.12(e). An active omni wheel, which can move freely in the forward and lateral directions, is applied as the driving unit. The end pair of the connecting chain is directly connected with the driving unit because the spherical pair and revolute pair form a four-system chain twist without overconstraint. As a result, when the driving units move in the lateral direction, the output platform realizes the $RxRyTz$ spatial motion. Additionally, by cooperatively moving the driving units forward or backward, the entire MPM can move in any desired direction. Therefore, this MPM has six DOFs, including three-DOF spatial mobility and three-DOF planar mobility.

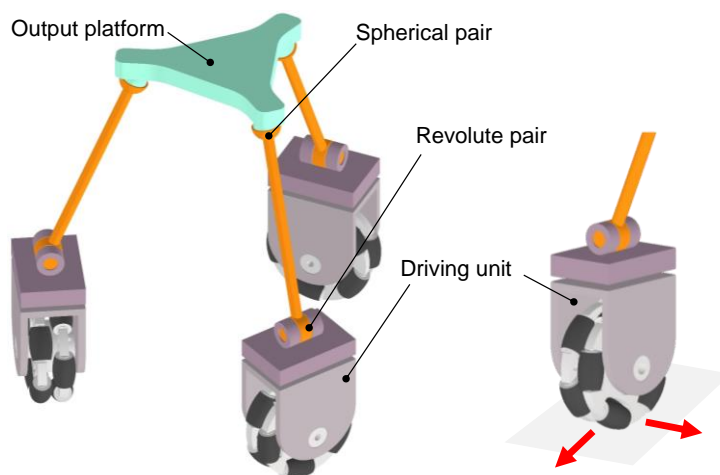


Fig. 3.16 3-RS MPM.

An example of MPM applying the structure in Group C is shown in Fig. 3.17, in which the connecting chain shown in Fig. 3.8(b) is integrated with the driving unit shown in Fig. 3.12(a). Here, an additional chain is added to limit the undesired motions. The connecting chain is composed of a

prismatic pair, a spherical pair, and a universal pair. The additional chain uses the combination of a prismatic pair and a universal pair to connect the mobile base with the output platform. The driving unit is the same as that shown in Fig. 3.14. Under the limitation of the additional chain, the spatial motion and planar motion of the output platform are achieved in the same way as the MPM shown in Fig. 3.14.

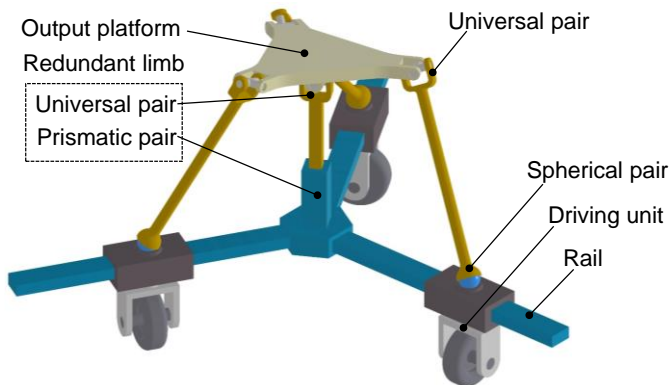


Fig. 3.17 MPM with an additional chain.

3.6 Summary

The MPM was proposed to solve the limited workspace issue of conventional parallel mechanisms. However, previous investigations about MPMs focused primarily on the kinematic of some specified MPMs and rarely addressed their type synthesis methods. With this in mind, this chapter tried to find out the possible six-DOF MPM structures by constructing a type synthesis method. The following results were obtained.

- A type synthesis method of six-DOF MPMs based on the screw theory was proposed. Based on the consideration that six-DOF mobility of MPM was divided into three-DOF planar motion and three-DOF spatial motion, and that the planar motions of the driving units were transmitted to realize these motions through the connecting chains, the type synthesis of the entire MPM was divided into the type synthesis of the mobile base and connecting chain.
- Two solutions for achieving three-DOF spatial motions were proposed to construct the type synthesis method of the connecting chain: applying singularity configuration to reduce DOFs and adding an additional chain to restrict undesired motions. Next, the possible connecting chain structures were enumerated and analyzed based on both solutions, and 14 types of feasible connecting chains were selected for further review.

- The type synthesis method proposed in Chapter 2 is applied to achieve the type synthesis of the driving unit. As a result of this synthesis, a total of 10 types of driving units matching the mobility requirement were obtained.
- The way of integrating the driving units and the connecting chains was revealed. The connecting chain structures were classified into three groups based on the DOF analysis. From the results, it was proved that the end pairs of connecting chain structures in two groups should be powered by driving units via the actuating mechanism, and then discussed the possible actuating mechanisms based on connecting chain structures and the motion of the driving unit used as the driving source. Ultimately, 284 possible types of MPM structures were suggested based on the proposed type synthesis method.
- Four MPMs were introduced as examples. All of these MPMs were theoretically capable of realizing the six-DOF mobility, in which the planar motion and spatial motion of the output platform were realized by the planar motions and relative motions of the driving units, respectively, as intended.

Chapter 4

Analysis of Traveling Strategies for Driving Vehicle around a Corner

4.1 Introduction

Chapters 2 and 3 focused on the type synthesis problem in the design stage of wheeled mobile robots regarding kinematics. For the next step, the motion of the wheeled locomotion vehicle, primarily the omnidirectional-wheeled vehicle, when traveling on a path is studied with respect to not only the statics but also the dynamics. Concerning the conventional-wheeled vehicles, various approaches regarding their path planning issue have been proposed to search the desired trajectory as introduced in Chapter 1 based on their dynamics characteristics. On the other hand, most of the studies about the path planning of the omnidirectional-wheeled vehicles are based on the kinematics, while there are few studies considering the dynamics. It is important to consider the dynamics when the omnidirectional-wheeled vehicle is required to travel at a high speed. Additionally, an omnidirectional wheeled vehicle can move forward/backward, to the left/right, and rotate. Therefore, various traveling strategies are possible even for a simple task, such as turning a corner. It has not been fully explored about choosing the suitable traveling strategy with consideration of dynamics according to the path condition. Especially, the omnidirectional-wheeled vehicle can move at a relatively high speed when its three-DOF mobility is used efficiently. Therefore, it is necessary to consider the dynamics characteristics of the omnidirectional-wheeled vehicle regarding the path planning.

With this in mind, this chapter intends to find out the feasible traveling strategy of the omnidirectional-wheeled vehicle when it travels at a specified path as the first step of the research about path planning. An angled path with one corner is chosen as the most fundamental situation because many different environments can be described by combining angled paths. The omnidirectional-wheeled vehicle (OWV) is chosen as research subject because the structure of omni wheel with passive rollers is relatively simple. The possible traveling forms of the OWV are proposed according to the timing of changing the orientation, where the traveling patterns are set for each form. Simulations are conducted to analyze the advantages of each traveling pattern when the path conditions are varied and figure out the time-optimal traveling strategies for various path conditions. As the comparison object of the OWV, the same investigation is also conducted on the conventional-wheeled vehicle (CWV). The time cost of the CWV and OWV is compared to figure out which types of vehicles are useful in various situations.

4.2 Modeling of Vehicles and Traveling Area

This section describes the kinetic model of the vehicle and defines the traveling area. Because this thesis focused on discussing and comparing the fundamental characteristics of traveling strategies, a simplified situation is considered. The driving motors were assumed to be ideal. In other words, the motor torque is large enough to rotate the wheels without delay, including at high speed. In addition, the maximum driving force of each wheel is considered to be equal to the maximum static friction force between the wheel and ground regardless of the rotation speed of the wheel.

4.2.1 Kinetic Model of Conventional Wheeled Vehicle

The CWV is a four-wheel-drive and four-wheel-steering type with conventional wheels. The structure is point-symmetric as shown in Fig. 4.1(a). The distance between the wheels at diagonal positions is d . A coordinate system x_c - y_c is constructed with the origin located at the center of the CWV.

On the assumption that the speed in the forward direction does not change during turning motion, the dynamic model of the CWV can be considered as a two-wheel-drive vehicle like Fig. 4.1(b), where the lateral force of the front and rear wheels are F_f and F_r , respectively [88-89]. The steering angle of each wheel α is sufficiently small in general, so that the directions of F_f and F_r can be approximated to be parallel with the x_c axis. Therefore, the equation of linear motion can be defined as:

$$F_{cy} = m\dot{v}_{cy}, F_{cx} = 0, \dot{v}_{cx} = 0, \dot{\omega}_c = 0, \quad (4.1)$$

where m is the mass of the CWV, v_{cx} and F_{cx} are the velocity and driving force in the x_c -axis direction, respectively, ω_c is the rotational angular velocity, and v_{cy} and F_{cy} are the velocity and driving force in the y_c -axis direction, respectively. The nonslip condition of the wheel is given as:

$$|F_{cy}| \leq \mu mg, \quad (4.2)$$

where μ is the friction coefficient between the wheel and ground, and g is the gravity acceleration.

Next, the equation of turning motion is defined as:

$$\begin{cases} m\dot{v}_{cx} = F_f + F_r \\ \dot{v}_{cy} = 0 \\ I\dot{\omega}_c = T_c = \sqrt{2}/4 d(-F_f + F_r) \end{cases}, \quad (4.3)$$

where I is the inertia moment around the center of the vehicle body and T_c is rotation torque. Considering that the load on both of the wheels is equally distributed under the condition of $\dot{v}_{cy} = 0$, the nonslip condition is obtained as:

$$\max(|F_f|, |F_r|) \leq \mu mg. \quad (4.4)$$

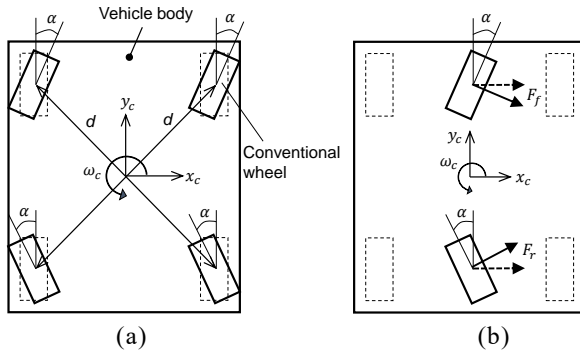


Fig. 4.1 Conventional-wheeled vehicle (CWV) model. (a) Overview, (b) Two-wheel model.

4.2.2 Kinematic Model of Omni-wheeled Vehicle

The OWV model shown in Fig. 4.2(a) consists of a square body and four omni wheels arranged at the center of each side in parallel. The distance between opposite wheels is d . The center of gravity is on the vertical axis passing through the center of the body and does not move relative to the vehicle while the vehicle moving. Each wheel is driven independently and can output driving force in one direction. A coordinate system x_o - y_o is fixed at the center of the vehicle, and its x_o and y_o axes run parallel to the diagonal lines of the body, as shown in Fig. 4.2(a).

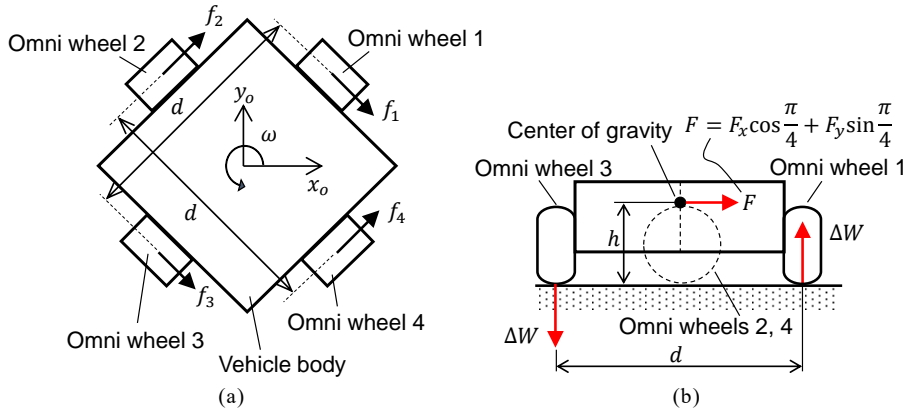


Fig. 4.2 Omni-wheeled vehicle (OWV) model. (a) Top view of OWV. (b) Load transfer between omni wheels 1 and 3

The equations of motion can be calculated as

$$\begin{cases} m\dot{v}_x = F_x = \frac{1}{\sqrt{2}}(f_1 + f_2 + f_3 + f_4) \\ m\dot{v}_y = F_y = \frac{1}{\sqrt{2}}(-f_1 + f_2 - f_3 + f_4) \\ I\dot{\omega} = T_r = \frac{d}{2}(-f_1 - f_2 + f_3 + f_4) \end{cases} \quad (4.5)$$

where f_i ($i = 1, 2, 3, 4$) is the driving force of omni wheel i ; v_x and v_y are the velocities in the x_o -axis and y_o -axis directions, respectively; ω is the rotation velocity; F_x and F_y are the driving

force of the vehicle in the x_o -axis and y_o -axis directions, respectively; T_r is rotation torque; m is the mass of the OWV, and I is the moment of inertia.

Next, the nonslip condition for the OWV is considered. The load on each omni wheel is $mg/4$ when the vehicle is in a static state. However, the load will transfer because of the inertial force while the vehicle is accelerating [20]. When the amount of the load transfer between omni wheels 1 and 3 is set as ΔW , as shown in Fig. 4.2(b), it can be calculated with consideration of the equilibrium of the moment.

$$d\Delta W = h(F_x \cos \frac{\pi}{4} + F_y \sin \frac{\pi}{4}) \quad (4.6)$$

Therefore, $\Delta W = h(F_x + F_y)/(\sqrt{2}d)$ is given, where h is the height of the center of gravity from the floor. The load transfer between omni wheels 2 and 4 is given in the same way. As a result, the nonslip condition for each wheel is written as

$$\begin{cases} |f_1|/\mu \leq \frac{mg}{4} - \frac{h}{\sqrt{2}d}(F_x + F_y) \\ |f_2|/\mu \leq \frac{mg}{4} + \frac{h}{\sqrt{2}d}(F_x - F_y) \\ |f_3|/\mu \leq \frac{mg}{4} + \frac{h}{\sqrt{2}d}(F_x + F_y) \\ |f_4|/\mu \leq \frac{mg}{4} - \frac{h}{\sqrt{2}d}(F_x - F_y) \end{cases} \quad (4.7)$$

4.2.3 Definition of Traveling Area

In the practical use of transportation vehicles, the area where the vehicle can move is usually limited because of obstacles or surrounding constructions. Thus, the area in which the vehicle can move is strictly defined. This thesis focuses on an angled path with one corner as the most fundamental situation because many different environments can be described by combining angled paths. Fig. 4.3 shows the target traveling area, where the x - y coordinate system is placed on the ground. Both edges of the area are straight lines. The position of the vehicle is represented by the center of gravity and the vehicle is constrained to keep its center of gravity within the area while moving. The intersection point of the centerlines is set as reference point O. The initial and terminal points are M and N, respectively. The path width is D and the corner angle is θ , which is set as $0 < \theta \leq \pi/2$ with the consideration of symmetry. The distances from point M to O (first half path) and that from point O to N (second half path) are defined as l_1 and l_2 , respectively. The point at which the inner angles intersect, that is the inside of the corner, is set as point P.

The motion of the vehicle running through the traveling area is divided into two types: linear motion with uniform acceleration and turning of the corner. First, the vehicle starts moving at point M with the velocity $v_m = 0$ and accelerates along the centerline of the path using linear motion. When approaching the corner, the vehicle transits to turning motion. After passing through the corner, the vehicle resumes linear motion. The start and end points of turning are set as S and F, respectively.

The distances between point S and O and between point O and F are set as l_s and l_f , respectively. The direction of the velocity vector at points S and F is parallel to the path edges. Velocities at point S and F are set as v_s and v_f , respectively. The time cost for the first linear motion, turning of the corner, and second linear motion are set as t_{ms} , t_{sf} , and t_{fn} , respectively. The summed time cost T is used to assess the entire motion.

$$T = t_{ms} + t_{sf} + t_{fn}. \quad (4.8)$$

In addition, the vehicle is required to return to the centerline after turning. Thus, the velocity direction at point F is coincident with the centerline. The vehicle can choose to rotate clockwise or counterclockwise to adjust its heading to the velocity direction, which is determined according to the time cost.

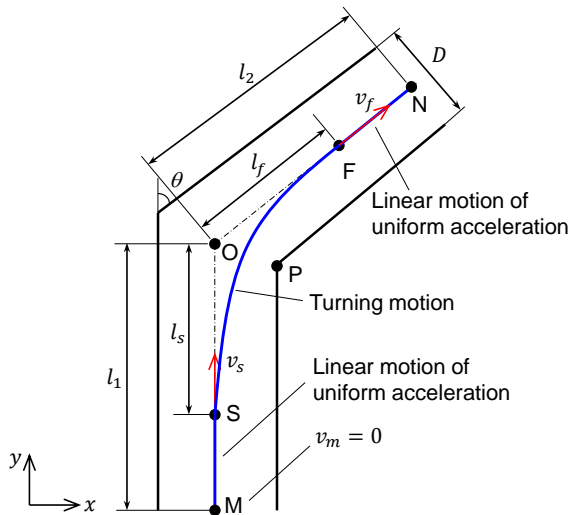


Fig. 4.3 Definition of traveling area and its parameters.

4.3 Motion Patterns of CWV and OVV

This section discusses the possible traveling patterns of vehicles within the defined area.

4.3.1 Motion Patterns of CWV

Regarding the first linear motion between point M and S, the maximum driving force that CWV can output is calculated by Eq. (4.2), and consequently, the maximum acceleration is given as follows:

$$|F_{cy}| = \mu mg \quad (4.9)$$

$$|\dot{v}_{cy}| = |F_{cy}|/m = \mu g. \quad (4.10)$$

The maximum acceleration for the latter linear motion between point F and N is given in the same way.

When the vehicle is turning the corner, the angular acceleration should satisfy the following inequalities according to Eqs. (4.3) and (4.4).

$$\begin{cases} \frac{d}{\sqrt{2}l} \left(-\frac{\mu mg}{2} + \frac{mv_c \omega_c}{2} \right) \leq \dot{\omega}_c \leq \frac{d}{\sqrt{2}l} \left(\frac{\mu mg}{2} - \frac{mv_c \omega_c}{2} \right) & \text{if } \omega_c \geq 0 \\ \frac{d}{\sqrt{2}l} \left(-\frac{\mu mg}{2} - \frac{mv_c \omega_c}{2} \right) \leq \dot{\omega}_c \leq \frac{d}{\sqrt{2}l} \left(\frac{\mu mg}{2} + \frac{mv_c \omega_c}{2} \right) & \text{if } \omega_c < 0 \end{cases} \quad (4.11)$$

where v_c is the velocity of the CWV. Eq. (4.11) gives the maximum and minimum angular acceleration of the CWV.

If the traveling area is not restricted, the total time cost of finishing the path becomes the minimum when the acceleration of the vehicle in the linear motion and turning motion are both the maximum, namely, when the linear acceleration is $|\dot{v}_{cmax}| = \mu g$ and the angular acceleration is

$$\dot{\omega}_c = \begin{cases} \frac{d}{\sqrt{2}l} \left(-\frac{\mu mg}{2} - \frac{mv_c \omega_c}{2} \right) & \text{for } 0 \leq \int(-\omega_c) dt \leq \frac{\theta}{2} \\ \frac{d}{\sqrt{2}l} \left(\frac{\mu mg}{2} + \frac{mv_c \omega_c}{2} \right) & \text{for } \frac{\theta}{2} < \int(-\omega_c) dt \leq \theta \end{cases} \quad (4.12)$$

This style of motion is named pattern R0.

With the restriction of the traveling area, on the other hand, the vehicle may deviate from the area at the corner when the acceleration is too large. Then, it is necessary to discuss how to avoid the deviation. The simplest way is to decelerate. If the vehicle decelerates before turning, the turning radius becomes smaller, which prevents the vehicle from the deviation even in the narrower width of the path. However, the time cost may become larger when the vehicle decelerates too much. It is beneficial to keep the deceleration as small as possible, namely, make the turning radius as large as possible. The turning radius takes the maximum value when the trajectory of the CWV passes through point P, as shown in Fig. 4.4(a). This style of motion is named pattern R1.

Another way is to return to the centerline of the path after approaching the outer edge. In this case, the vehicle is permitted to cross the centerline once and then turns back to reach point F as shown in Fig. 4.4(b). In this situation, if the turning is finished quickly, i.e., point F is kept close to point O, more space to accelerate in the latter linear motion is supplied. Then, this moving method also can be a candidate for optimal motion. In the case where the vehicle deviates from the outer edge of the traveling area, deceleration should be put before turning like in pattern R1. This style of motion is named pattern R2.

One of the above traveling patterns R0, R1, and R2 that requires the smallest time cost without deviation from the traveling area is considered to be the optimal motion strategy of the CWV.

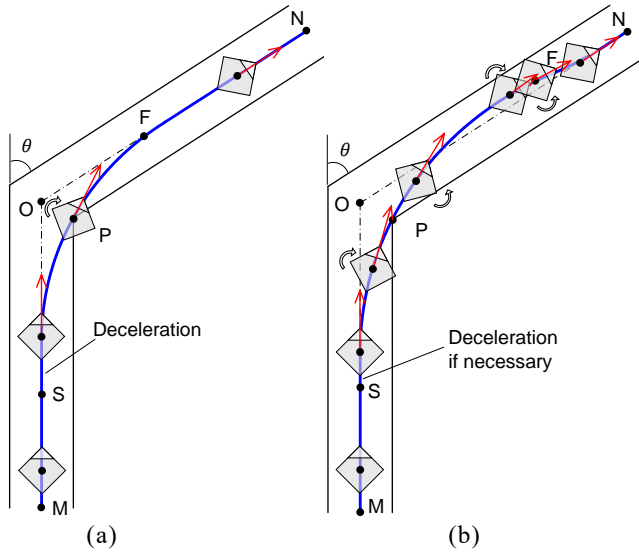


Fig. 4.4 Traveling approach of CWV. (a) Pattern R1, (b) Pattern R2

4.3.2 Motion Patterns of OWV

The traveling direction of the conventional vehicle is fixed relative to the vehicle body, but OWV can move in any direction. According to (4.5) and (4.7), the driving force of the OWV should satisfy the following equation:

$$|F_x| + |F_y| \leq \frac{\mu mg}{\sqrt{2}}. \tag{4.13}$$

Therefore, the maximum value of the driving force varies depending on the direction, as shown in Fig. 4.5. The driving force takes the largest value on the boundaries of a quadrangular area. The four boundaries are called modes I, II, III, and IV.

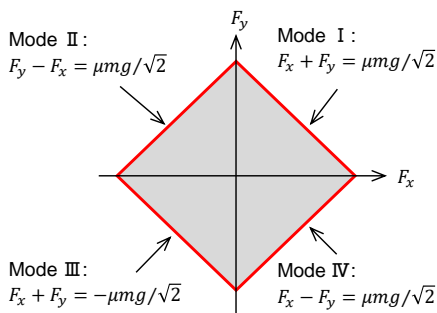


Fig. 4.5 Distribution of driving force in the x_o - y_o coordinate system.

The OWV can perform turning, during which the vehicle travels with a changing velocity vector, and rotation, during which the vehicle changes its orientation with respect to the traveling direction. The order and timing of these motions, which are performed independently, determine the traveling

form. Here, three traveling forms are considered according to the order of the above motions as follows:

Form A: Changing the vehicle orientation after changing the velocity vector direction, namely, rotation after turning.

Form B: Changing the vehicle orientation before changing the velocity vector direction, namely, rotation before turning.

Form C: Changing the vehicle orientation and velocity vector direction at the same time, namely, rotation during turning.

The kinetic model of each form is discussed below.

4.3.2.1 Form A: Rotation after Turning

Without the restriction of the traveling area, the acceleration during the first linear motion and during the turning motion should take the maximum value to reduce the time cost, which can be calculated as

$$\begin{cases} |\dot{v}_y| = \frac{\mu g}{\sqrt{2}}, \dot{v}_x = 0 & \text{for the first linear motion} \\ |\dot{v}_x| = \frac{\mu g}{\sqrt{2}}, \dot{v}_y = 0 & \text{for the turning motion} \end{cases} \quad (4.14)$$

After turning, the vehicle can accelerate and rotate either independently or at the same time. Therefore, there are three possible operating modes: rotation before acceleration, rotation after acceleration, and rotation during acceleration. When the vehicle rotates and accelerates independently, assuming that the translational acceleration is zero and the rotation torque takes the maximum value during rotation, the time cost of the rotation t_r can be calculated by the following equation:

$$\begin{cases} I \frac{d\omega}{dt} = \frac{1}{2} \mu m g d \\ \min \left(\theta, \frac{\pi}{2} - \theta \right) = \omega t_r \end{cases} \quad (4.15)$$

As a result, the equations of motion for independent acceleration and rotation can be written as

$$\begin{cases} v_f t_r + v_f (t_{fn} - t_r) + \frac{\mu g}{2\sqrt{2}} (t_{fn} - t_r)^2 = l_2 - l_f & \text{for acceleration after rotation} \\ v_f (t_{fn} - t_r) + \frac{\mu g (t_{fn} - t_r)^2}{2\sqrt{2}(\cos\theta + \sin\theta)} + \left[v_f + \frac{\mu g (t_{fn} - t_r)}{\sqrt{2}(\cos\theta + \sin\theta)} \right] t_r = l_2 - l_f & \text{for rotation after acceleration} \end{cases} \quad (4.16)$$

When the vehicle accelerates and rotates at the same time, there is a trade-off between rotation torque and translational driving force. The situation is considered where the angular velocity at both points F and N is zero, the angular acceleration is distributed symmetrically between the first and

second halves, and the driving force takes the maximum value that satisfies the nonslip condition. The equations of motion are given as follows:

$$\begin{cases} I\dot{\omega} = T_{r1}, & \frac{1}{2}\dot{\omega}t_h^2 = \frac{\beta}{2} & \text{for } 0 \leq \varphi \leq \frac{\beta}{2} \\ I\dot{\omega} = T_{r2}, & \dot{\omega}t_h(t_{fn} - t_h) + \frac{1}{2}\dot{\omega}(t_{fn} - t_h)^2 = \frac{\beta}{2} & \text{for } \frac{\beta}{2} < \varphi \leq \beta \\ \iint_0^{t_{fn}/2} \frac{F_{t1}}{m} dv dt + \iint_{t_{fn}/2}^{t_{fn}} \frac{F_{t2}}{m} dv dt = l_2 - l_f & & \\ F_{t1}, F_{t2} = \max(F_x \sin(\theta - \varphi) + F_y \cos(\theta - \varphi)) & \text{if } 0 \leq \theta \leq \pi/4 \\ F_{t1}, F_{t2} = \max(F_x \sin(\theta + \varphi) + F_y \cos(\theta + \varphi)) & \text{if } \pi/4 < \theta \leq \pi/2 \\ t_{fn} = 2t_h, T_{r1} = -T_{r2}, \beta = \min\left(\theta, \frac{\pi}{2} - \theta\right) & & \end{cases} \quad (4.17)$$

where T_{r1} and T_{r2} are the driving torques of the first and second halves of the rotation, respectively; F_{t1} and F_{t2} are the driving force of the first and second halves of the translation, respectively; t_h is the time cost of the first half of the rotation; φ is the rotation angle of the vehicle body. t_{fn} is obtained with the combination of Eqs. (4.5), (4.7), and (4.17).

Of these three forms, the one that has the smallest time cost is chosen as the motion after turning. The resulting motion is defined as pattern A0.

When taking the restriction of the traveling area into account, the traveling pattern discussed above can be the optimal motion if there is no deviation from the traveling area. Otherwise, the vehicle should decelerate in the y -axis direction before turning. However, the OWV can accelerate in the x -axis direction and decelerate in the y -axis direction at the same time. To use the path width maximally, the trajectory should pass through point P. Then, the time cost from point S to point P t_{sp} can be calculated by the following equation:

$$\begin{cases} F_x - F_y = \frac{\mu mg}{\sqrt{2}} \\ \frac{1}{2} \frac{F_x}{m} t_{sp}^2 = \frac{D}{2} \\ v_s t_{sp} - \frac{1}{2} \frac{F_y}{m} t_{sp}^2 = l_s - \frac{D}{2} \tan \frac{\theta}{2} \end{cases} \quad (4.18)$$

where l_s is a variable whose suitable value will be determined to minimize the time cost.

Here, the u - w coordinate system shown in Fig. 4.6 is employed to discuss the movement after point P conveniently. The u and w axes are perpendicular and parallel to the second half of the path, respectively. The velocity in the u -axis direction at point P v_{pu} must be negative to avoid the departure from the path.

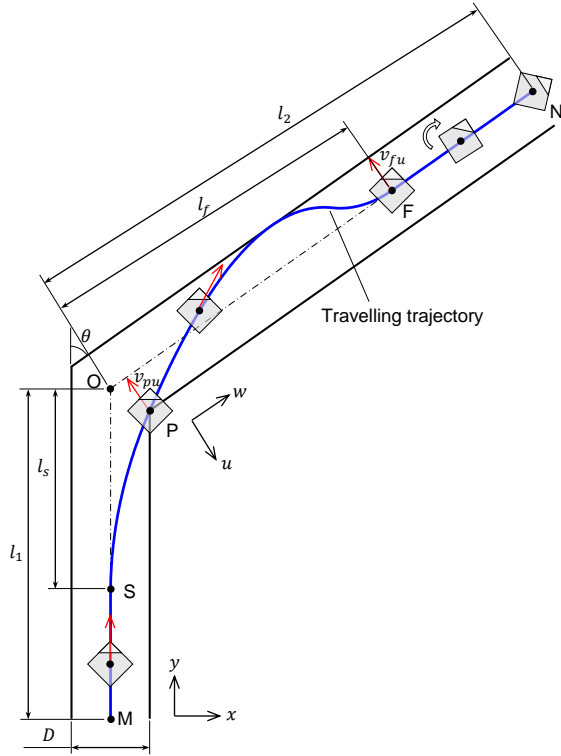


Fig. 4.6 Motion trajectory of form A.

The driving force relation is translated from the x - y coordinate system to the u - w coordinate system as shown in Fig. 4.7. The driving forces in the u -axis and w -axis directions are set as F_u and F_w , respectively. When $0 < \theta \leq \pi/4$, it is inferred from Fig. 4.7(a) that mode I is the most suitable because both F_u and F_w can take large values. In this situation, the acceleration in the u -axis direction should lie within the following range:

$$-\frac{\mu g \sin \theta}{\sqrt{2}} \leq \ddot{u} \leq \frac{\mu g \cos \theta}{\sqrt{2}}. \quad (4.19)$$

It is necessary to make the velocity in the u -axis direction at point F, v_{fu} , equal to zero. When the trajectory of the vehicle converges with the centerline, the relation of the acceleration and velocity between point P and F can be obtained as follows:

$$v_{pu} t_{pf} - \frac{\ddot{u} t_{pf}^2}{2} \leq \frac{D}{2} \quad \wedge \quad v_{fu} = v_{pu} - \ddot{u} t_{pf} = 0 \Leftrightarrow \ddot{u} \geq \frac{v_{pu}^2}{D} \quad (4.20)$$

where t_{pf} is the time cost between points P and F. As a result, when $v_{pu}^2/D \leq \mu g \cos \theta/\sqrt{2}$, the acceleration should be set as $\ddot{u} = -\mu g \sin \theta/\sqrt{2}$ to let the vehicle travel toward the centerline from the inner edge and then change to $\ddot{u} = \mu g \cos \theta/\sqrt{2}$ to let the vehicle converge with the centerline. This series of motions is defined as pattern A1.

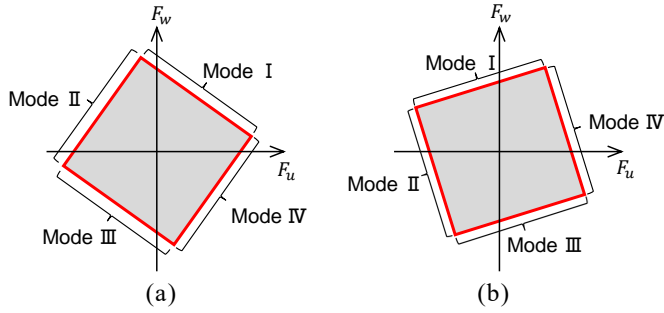


Fig. 4.7 Distribution of driving force in the u - w coordinate system. (a) $0 < \theta \leq \pi/4$, and (b) $\pi/4 < \theta \leq \pi/2$.

When v_{pu} is too large to make the trajectory converge with the centerline, the vehicle should travel toward the outer edge within the limitation of the path width.

$$v_{pu}t_{po} - \frac{\dot{u}t_{po}^2}{2} \leq D \wedge v_{ou} = v_{pu} - \dot{u}t_{po} = 0 \wedge t_{pf} = t_{po} + t_{of} \Leftrightarrow \dot{u} \geq \frac{v_{pu}^2}{2D} \quad (4.21)$$

where t_{po} is the time cost from point P to the point nearest to the outer edge, t_{of} is the time cost from that point to point F, and v_{ou} is the velocity in the u -axis direction at that point. In summary, when $v_{pu}^2/D > \mu g \cos \theta / \sqrt{2}$, the acceleration should be set as $\dot{u} = \mu g \cos \theta / \sqrt{2}$ to let the vehicle cross the centerline to the outer edge and then change to $\dot{u} = -\mu g \sin \theta / \sqrt{2}$ to let the vehicle converge with the centerline. These series of motions are defined as pattern A2.

When $\pi/4 < \theta \leq \pi/2$, Fig. 4.7(b) shows that F_u in mode IV is larger than that in mode I. As a result, it is necessary to use mode IV with mode I in some cases. In this situation, the acceleration in the u -axis direction should lie within the following range:

$$-\frac{\mu g \sin \theta}{\sqrt{2}} \leq \dot{u} \leq \frac{\mu g \sin \theta}{2}. \quad (4.22)$$

The basic idea to finish the path is the same as when using only mode I, as described above. When using mode IV, the traveling patterns are defined as patterns A3, A4, and A5. Pattern A3 aims at turning the corner without crossing the centerline under the condition $v_{pu}^2/D \leq \mu g \sin \theta / \sqrt{2}$. When the vehicle cannot travel by pattern A3, that is, when $v_{pu}^2/D > \mu g \sin \theta / \sqrt{2}$, the vehicle is permitted to cross the centerline in pattern A4. When $v_{pu}^2/2D > \mu g \cos \theta / \sqrt{2}$, the vehicle travels to touch the outer edge so that the deceleration in the u -axis direction is minimized, which is defined as pattern A5.

The trajectories of patterns A0-A5 from point P are shown in Fig. 4.8. The flowchart of determining the optimal motion for the traveling strategy of form A is shown in Fig. 4.9.

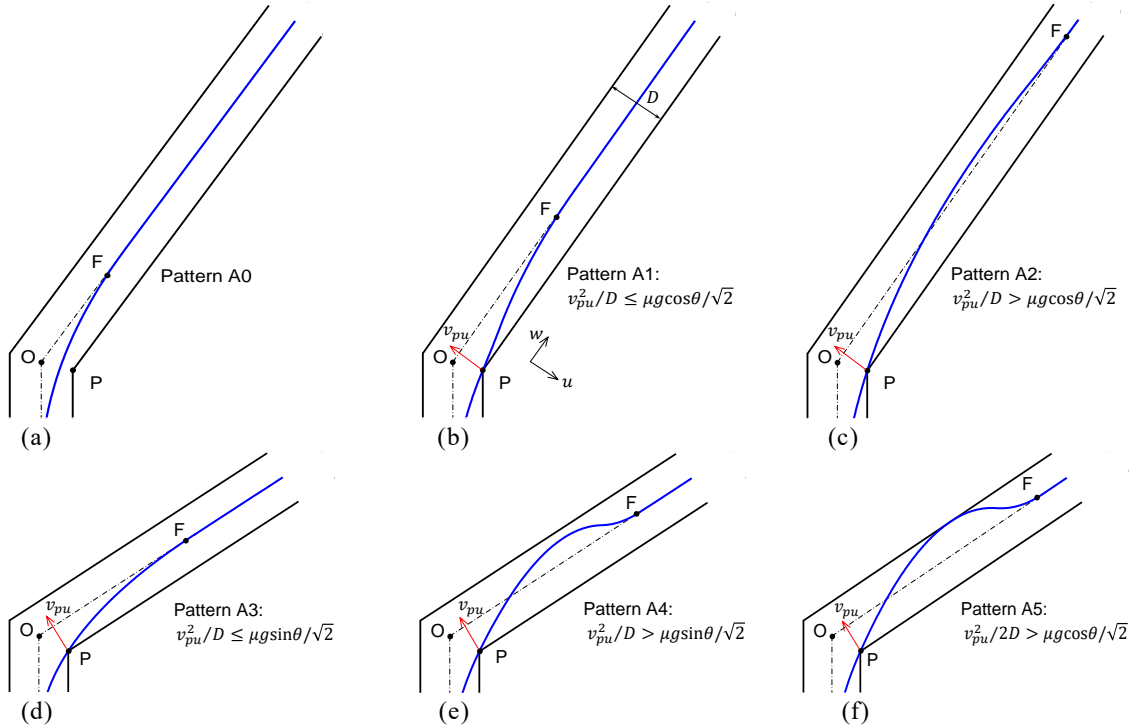


Fig. 4.8 Traveling patterns of form A. (a) Pattern A0, (b) Pattern A1, (c) Pattern A2, (d) Pattern A3, (e) Pattern A4 and (f) Pattern A5.

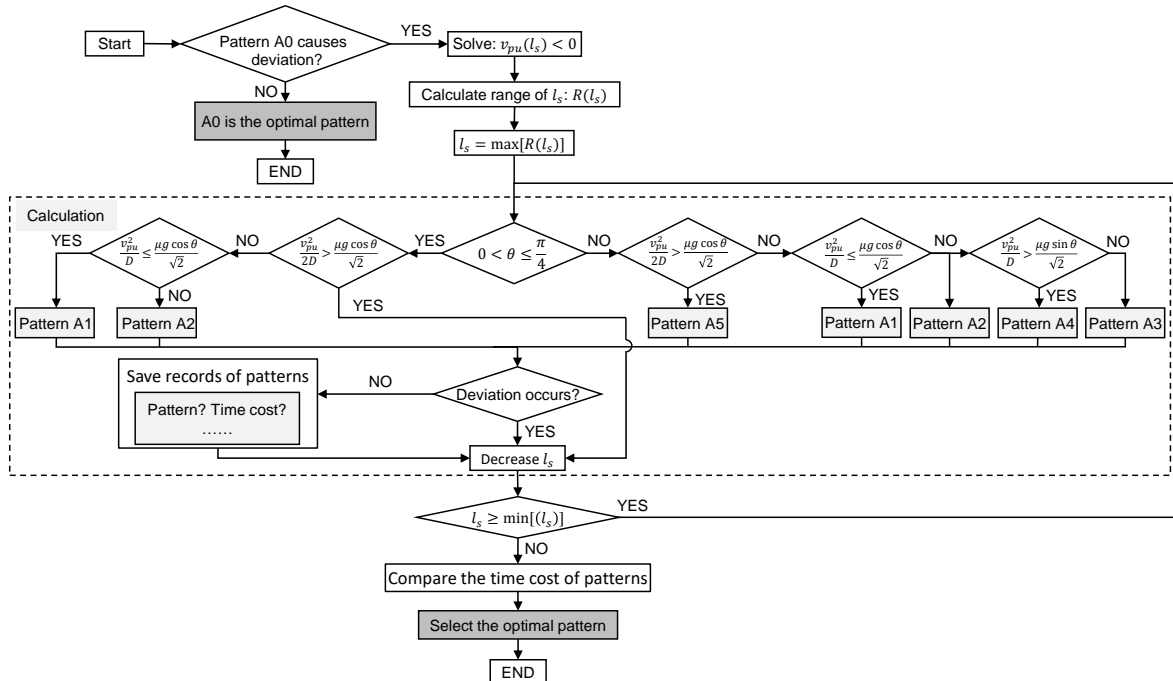


Fig. 4.9 Flowchart of determining optimal motion for form A

4.3.2.2 Form B: Rotation before Turning

When traveling with form B, the OWV first rotates, which changes the vehicle's orientation to direct the front toward the w -axis direction, and then turns, as shown in Fig. 4.10.

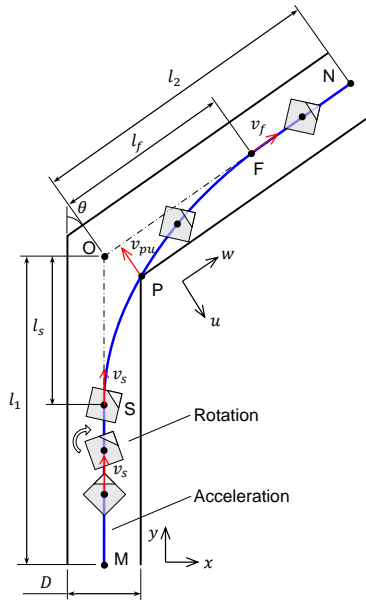


Fig. 4.10 Motion trajectory of form B

Without the restriction of the traveling area, assuming that rotational torque takes the maximum value and the translational velocity stays constant during the rotation, the equations of motion can be written as follows:

$$\begin{cases} \frac{1}{2} \dot{v}_y (t_{ms} - t_r)^2 + v_s t_r = l_1 - l_s, \dot{v}_y = \frac{\mu g}{\sqrt{2}}, \dot{v}_x = 0 \text{ for motion before rotation} \\ I \frac{d\omega}{dt} = \frac{1}{2} \mu m g d, \min\left(\theta, \frac{\pi}{2} - \theta\right) = \omega t_r, \text{ for motion during rotation} \\ v_s \sin\theta = \ddot{u} t_{sf}, \ddot{u} = \frac{\mu g}{\sqrt{2}}, \ddot{w} = 0 \text{ for motion during turning} \end{cases} \quad (4.23)$$

The traveling way for the turning motion is the same as that in form A. In the second linear motion, the vehicle travels straight at the maximum acceleration. The above series of motions are defined as pattern B0.

When the restriction of the traveling area is taken into account, the trajectory should pass through point P to obtain the maximal turning radius. Therefore, the equation of motion from point S to point P is as follows:

$$\begin{cases} F_x - F_y = \frac{\mu m g}{\sqrt{2}} \\ \frac{1}{2} \frac{F_x}{m} t_{sp}^2 = \frac{D}{2} \\ v_s t_{sp} - \frac{1}{2} \frac{F_y}{m} t_{sp}^2 = l_s - \frac{D}{2} \tan \frac{\theta}{2} - v_s t_r \end{cases} \quad (4.24)$$

A suitable value of l_s will be determined to minimize the time cost.

After passing through point P, acceleration in the w -axis direction should be positive. Fig. 4.11 shows the driving force relation in the u - w coordinate system when $\theta > \pi/4$. According to Fig. 4.11, modes I and IV are suitable because the value of F_w stays positive. When a combination of modes I and IV is used, the boundary of acceleration in the u -axis direction is given as follows:

$$-\frac{\mu g}{\sqrt{2}} \leq \ddot{u} \leq \frac{\mu g}{\sqrt{2}} . \tag{4.25}$$

When $\theta \leq \pi/4$, modes I and II instead of modes I and IV should be chosen, but the traveling way is the same.

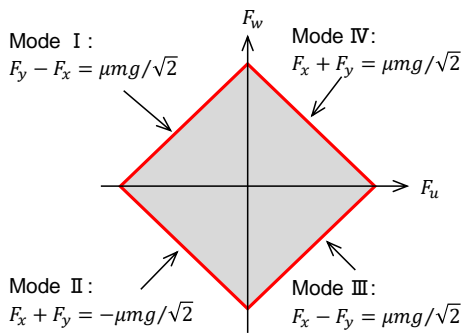


Fig. 4.11 Distribution of driving force for form B in u - w coordinate system when $\theta > \pi/4$.

It is also necessary for the vehicle to converge with the centerline as quickly as possible, namely, to minimize l_f to gain the space needed to accelerate during the second linear motion. The conditions of Eq. (4.25) allow three patterns of motion: B1, B2, and B3. In the case of $v_{pu}^2/D \leq \mu g/\sqrt{2}$, the vehicle simply approaches the centerline, which is defined as pattern B1. When v_{pu} is larger, that is, $\mu g/\sqrt{2} < v_{pu}^2/D \leq \sqrt{2}\mu g$, the vehicle crosses the centerline, which is defined as pattern B2. When the width of the path is so limited that $v_{pu}^2/D > \sqrt{2}\mu g$ is satisfied, the vehicle can travel only if it touches the outer edge of the path, which is pattern B3.

The trajectories of patterns B0-B3 from point P are shown in Fig. 4.12. The flowchart of determining the optimal pattern for the traveling strategy of form B is shown in Fig. 4.13.

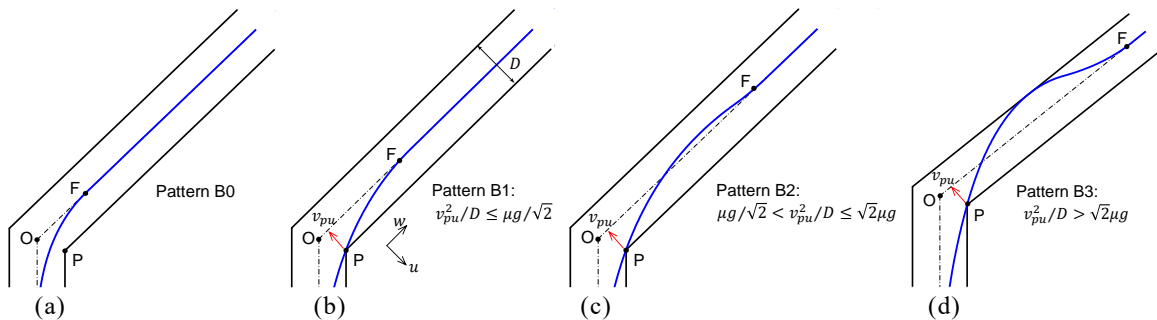


Fig. 4.12 Motion patterns of form B. (a) Pattern B0, (b) Pattern B1, (c) Pattern B2 and (d) Pattern B3.

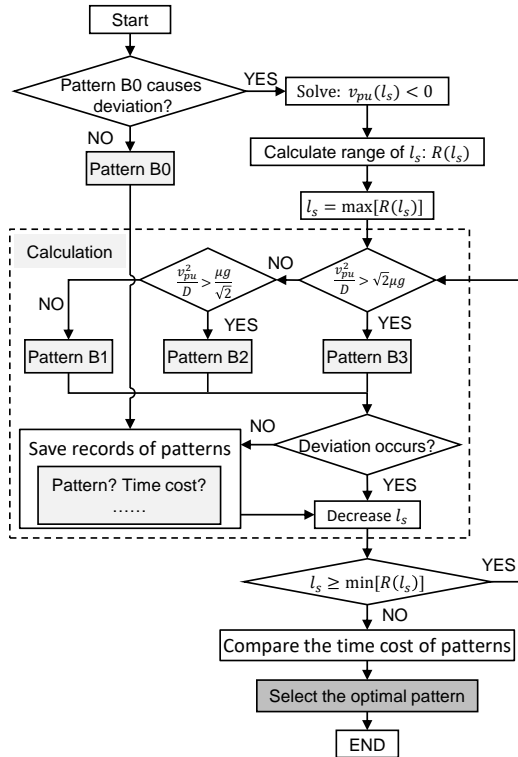


Fig. 4.13 Flowchart of determining optimal motion for form B

4.3.2.3 Form C: Rotation during Turning

With traveling form C, the vehicle rotates and turns at the same time. In the first and second linear motions, the vehicle can run with the maximum acceleration $\mu g/\sqrt{2}$. According to Eqs. (4.5) and (4.6), the rotational angular acceleration during turning can be calculated as follows:

$$\begin{cases} \frac{d}{2l}(-\mu mg + \sqrt{2}mv\omega) \leq \dot{\omega} \leq \frac{d}{2l}(\mu mg - \sqrt{2}mv\omega) & \text{if } \omega \geq 0 \\ \frac{d}{2l}(-\mu mg - \sqrt{2}mv\omega) \leq \dot{\omega} \leq \frac{d}{2l}(\mu mg + \sqrt{2}mv\omega) & \text{if } \omega < 0 \end{cases} \quad (4.26)$$

When the restriction of the traveling area is not considered, the summary time cost of finishing the path is minimized if the acceleration of the linear motion and turning motion takes the maximum values. At this time, the linear acceleration is equal to $\sqrt{2}\mu g/2$, while the angular acceleration is as follows:

$$\dot{\omega} = \begin{cases} \frac{d}{2l}(-\mu mg - \sqrt{2}mv\omega) & \text{for } 0 \leq \int(-\omega) dt \leq \frac{\theta}{2} \\ \frac{d}{2l}(\mu mg + \sqrt{2}mv\omega) & \text{for } \frac{\theta}{2} < \int(-\omega) dt \leq \theta \end{cases} \quad (4.27)$$

This style of motion is defined as pattern C0.

The limited width of the path may cause the vehicle to deviate from the traveling area during turning. To avoid this, deceleration before turning is necessary, similar to that needed in forms A and B. In this case, there are two motion patterns depending on whether the vehicle is permitted to cross the centerline or not, which are defined as patterns C1 and C2, respectively. The trajectories of patterns C0-C2 are shown in Fig. 4.14.

All motion patterns for forms A, B, and C are summarized in Table 4.1.

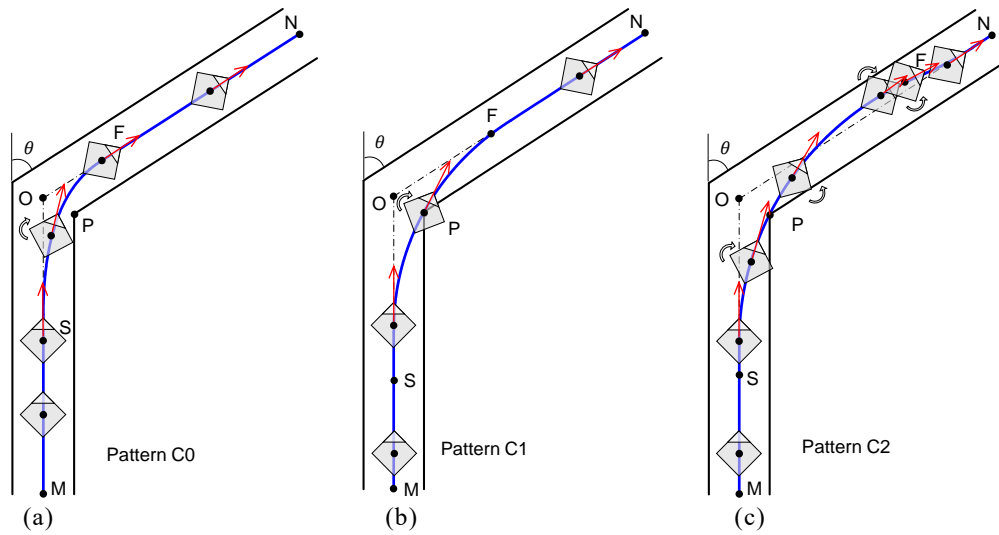


Fig. 4.14 Traveling approach of form C. (a) Pattern C0, (b) Pattern C1, and (c) Pattern C2

Table 4.1 Traveling patterns of OWV from point P with respect to route centerline.

Form	Pattern	Trajectory of pattern	Form	Pattern	Trajectory of pattern
Form A (rotation after turning)	A0		Form B (rotation before turning)	B0	
	A1			B1	
	A2			B2	
	A3		B3		
	A4		Form C (rotation during turning)	C0	
A5		C1			
				C2	

4.4 Analysis and Comparison of Traveling Strategies

The proposed traveling patterns of both types of vehicles are analyzed and compared through simulations in this section. The parameters of vehicles used in the simulation are listed in Table 4.2.

Table 4.2 Parameters of CWV and OWV

Symbol	Description
m	3.0 kg
g	9.8 m/s ²
d	0.3 m
μ	0.3
I	0.045 kg·m ²

4.4.1 Traveling Strategies Analysis of CWV

Some examples of the traveling patterns of the CWV when the curve angle θ and path width D are varied under the condition of $l_1 = 10$ m and $l_2 = 10$ m are shown in Fig. 4.15. The figure shows that pattern R0 causes deviation from the path when the curve angle gets close to $\pi/2$ with $D = 2$ m. Also, the vehicle deviates from the path even at $\theta = 4\pi/16$ with $D = 0.5$ m. This means that it becomes difficult for the vehicle to output the maximum acceleration when the path becomes sharp and narrow.

In contrast, there is no solution of pattern R1 or R2 with $D = 2.0$ m and $\theta = \pi/16$. The reason is that the requirement of passing through point P leads to too large turning radius. In the other cases with $D = 2.0$ m, Pattern R1 lets the vehicle travel the path smoothly because of the deceleration before turning. On the other hand, pattern R2 fails to make the path cross the centerline at $\theta = 4\pi/16$ because the deceleration is too much. When the curve angle is still sharper, at $\theta = 7\pi/16$, pattern R2 can be achieved. With $D = 0.5$ m, both patterns R1 and R2 are completed at $\theta = 4\pi/16$ and $\theta = 7\pi/16$.

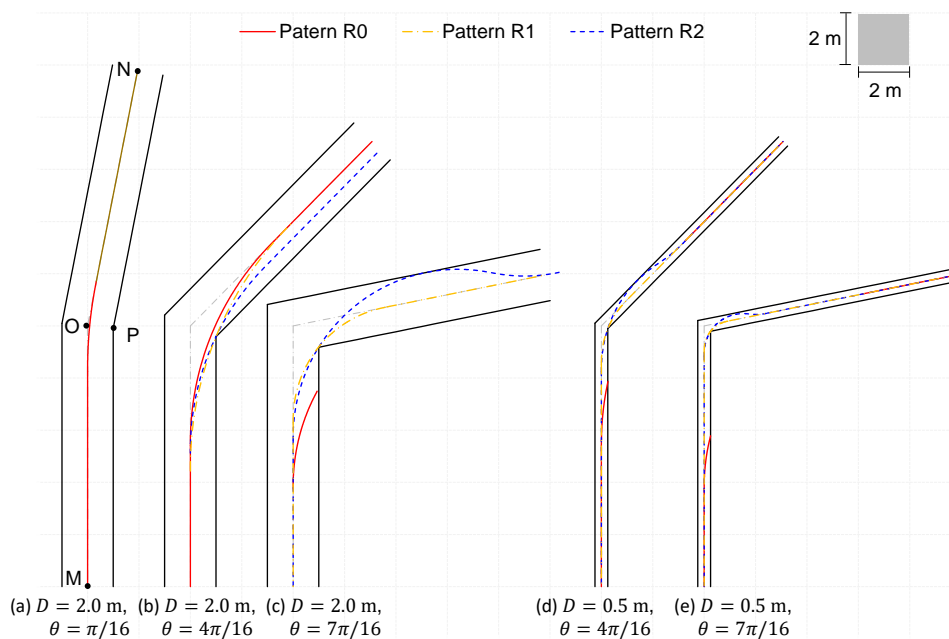


Fig. 4.15 Traveling patterns of CWV at $l_1 = 10$ m and $l_2 = 10$ m

Fig. 4.16 shows time-optimal patterns when the curve angle θ and the distance from point M to O l_1 vary with $D = 2.0$ m and $l_2 = 10$ m. The time-optimal pattern changes along with the alteration of θ and l_1 . Pattern R0 is advantageous when l_1 or θ is relatively small as shown in the graph. When l_1 is increased and θ becomes larger, pattern R0 is no longer the time-optimal one because it becomes impossible for the vehicle to travel the path without deceleration to avoid the deviation. In this case, pattern R2 costs less time than pattern R1 because pattern R2 requires

less deceleration. However, when θ gets close to $\pi/2$, less deceleration causes deviation from the outer edge or longer moving distance in pattern R2. In this situation, pattern R1 is optimal. Due to the appropriate deceleration, pattern R1 enables the vehicle to get tangent to the centerline sooner, which contributes to supplying more space for linear acceleration.

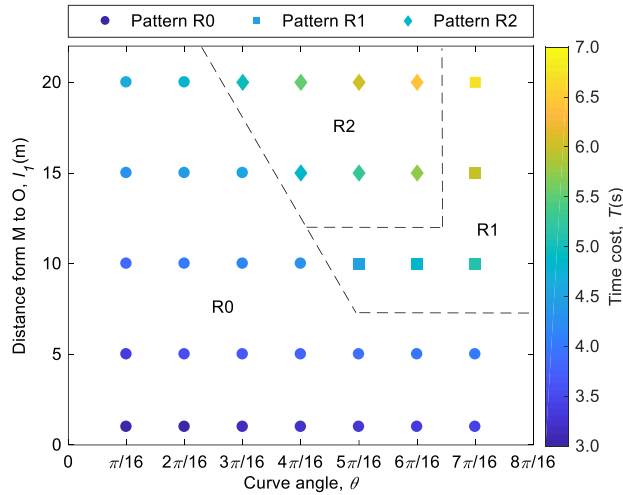


Fig. 4.16 Least time cost for different curve angle at $l_2 = 10$ m and $D = 2.0$ m

Fig. 4.17 indicates the time-optimal patterns when the width of the path D varies instead of l_1 with $l_1 = 8.0$ m and $l_2 = 10$ m. In general, the vehicle traveled by pattern R0 costs the least time when θ is relatively small and D is large enough. However, traveling by pattern R2 costs the least time when both D and θ are relatively small. Along with the increment of D and θ , the vehicle traveled by pattern R1 wins the others. When the curve angle is relatively small, less deceleration is required in pattern R2 and the vehicle can move faster than by pattern R1. When the curve angle becomes larger, the larger moving distance of pattern R2 leads to the increment of the time cost. The figure shows that pattern R1 is advantageous even in the narrow width and large curve angle. Although the deceleration before turning may cost more time in pattern R1, the deceleration makes the vehicle get close to the centerline earlier than pattern R2, which brings more space for the linear acceleration.

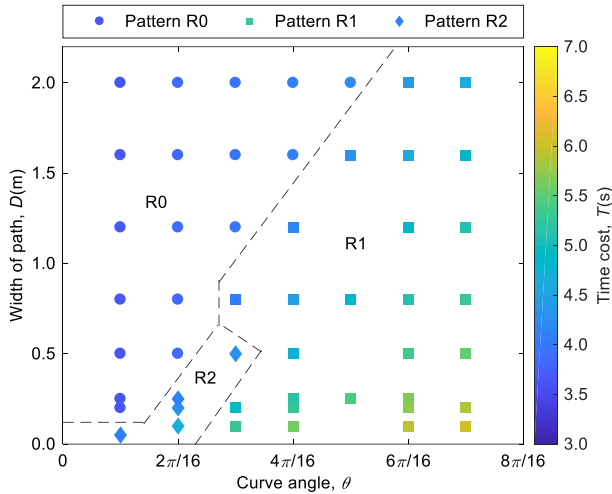


Fig. 4.17 Least time cost for different widths of path at $l_1 = 8.0$ m and $l_2 = 10$ m

4.4.2 Traveling Strategies Analysis of OWV

4.4.2.1 Characteristics of Form A

First, the characteristics of the trajectories in the six motion patterns for form A are discussed. Fig. 4.18 shows examples of the trajectories calculated under the condition of $l_1 = l_2 = 10$ m. The figure shows that the variation of the corner angle θ and path width D affects the pattern features. The trajectories cut off in the middle indicate that a deviation occurs at that point. In pattern A0, where the vehicle runs at the largest acceleration without considering the restriction of the traveling area, the vehicle can stay on the path only when θ is small and D is large [Fig. 4.18(a)]. Comparison of patterns A1 and A2 shows that, although their trajectories are similar to each other in Fig. 4.18(b), the trajectory crosses the centerline in pattern A2 but not in pattern A1, as shown in Fig. 4.18(c), (d), and (e). The trajectory of pattern A2 has the advantage of less deceleration before turning the corner, but at the same time, it has the disadvantage of a larger travel distance. Pattern A1 has the opposite effects. For patterns A3, A4, and A5, their trajectories reach the centerline after turning in the order of A4, A3, and A5 in both Fig. 4.18(c) and (e). This means that the trajectory of pattern A4 goes over the centerline slightly and the trajectory of A5 travels well past the centerline, while pattern A3 establishes a track somewhere in the middle without crossing over the centerline. With respect to D , a narrow path makes turning the corner difficult in general, but it contributes to decreased travel distance in patterns A2 and A5, as shown by comparing Fig. 4.18(c) and (e).

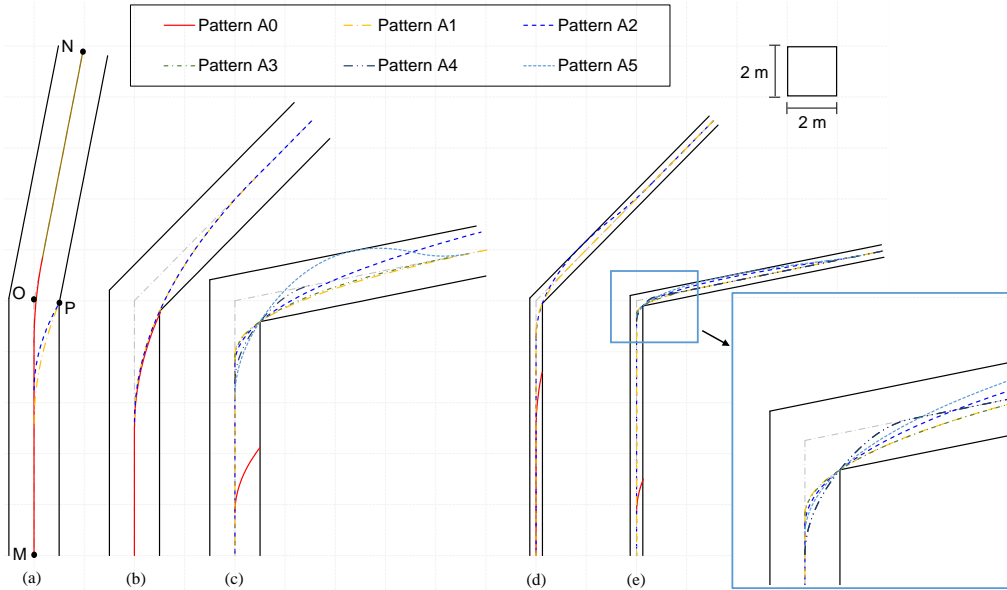


Fig. 4.18 Trajectories of six motion patterns of form A with $l_1 = 10$ m and $l_2 = 10$ m. (a) $D = 2.0$ m, $\theta = \pi/16$ (b) $D = 2.0$ m, $\theta = 4\pi/16$ (c) $D = 2.0$ m, $\theta = 7\pi/16$ (d) $D = 0.5$ m, $\theta = 4\pi/16$ (e) $D = 0.5$ m, $\theta = 7\pi/16$.

Next, the traveling time cost is compared according to the variation of the path conditions. Fig. 4.19 shows the calculation results of the least-time cost when the corner angle θ varies with $l_2 = 10$ m and $D = 2.0$ m. The name of the least-time pattern is shown beside each sampling point. In the graph, as θ becomes larger, the time cost tends to increase and the optimal patterns change. When θ is small, the vehicle can travel by pattern A0 and the time cost increases only a little. Then, after pattern A0 is no longer feasible due to the large θ , the optimal pattern switches to pattern A2 and finally A3. At this point, the time cost shows stronger growth because the OWV must decelerate before turning. When l_1 is large enough, for example, $l_1 = 20$ m, pattern A1 also appears between A0 and A2.

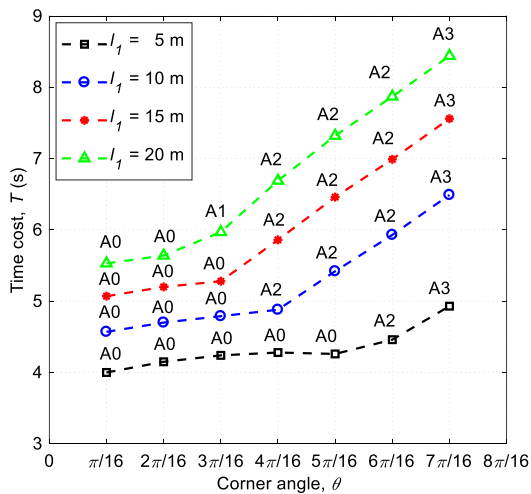


Fig. 4.19 Least-time cost of form A when corner angle varies with $l_2 = 10$ m and $D = 2.0$ m

Fig. 4.20 shows the time cost when the width of the path D varies with $l_1 = 8.0$ m and $l_2 = 10$ m. The graph shows that the time cost tends to decrease as D increases and that the least-time pattern changes due to the variation and consequently converges to pattern A0. Once pattern A0 becomes feasible, the time cost remains constant even when D is changed. When D is relatively small, the time cost decreases strongly, for the same reasons seen in Fig. 4.19.

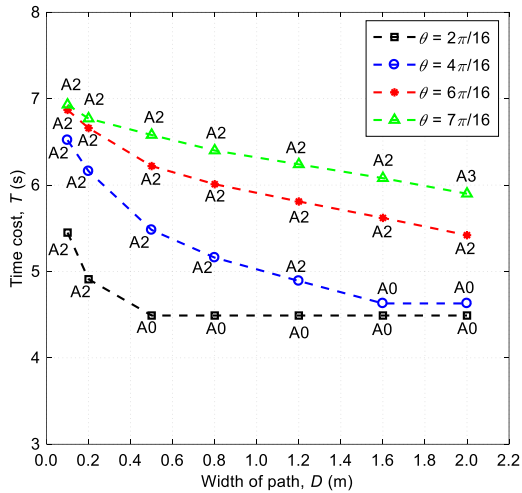


Fig. 4.20 Least-time cost of form A when path width varies with $l_1 = 8.0$ m and $l_2 = 10$ m.

By expanding the calculation results, the traveling strategy is explored according to various configurations of the traveling area. Fig. 4.21 shows the regions of the least-time patterns when the corner angle θ and the first half path length l_1 are varied with $l_2 = 10$ m and $D = 2.0$ m. When θ or l_1 is relatively small, the vehicle can always travel with pattern A0, so that pattern A0 should be chosen. However, when θ and l_1 become larger, pattern A0 is no longer feasible because of the limited path width and then pattern A1 or A2 takes its place. The trajectories of patterns A1 and A2 are close to each other under the specific corner angle, for example, $\theta = \pi/4$ shown in Fig. 4.18(b). When θ becomes larger, in other words, when the corner angle is severe, pattern A2 is advantageous because its trajectory can obtain a large turning radius, which contributes to minimizing deceleration. In contrast, pattern A1 is faster than pattern A2 when θ is smaller because it has a sufficiently large turning radius without crossing the centerline. When θ is still larger, that is, $\theta = 7\pi/16$, it becomes difficult for the vehicle to return to the centerline quickly after turning the corner in pattern A2. That leads to an increase in the moving distance and time cost. In this case, pattern A3, which draws a turning radius larger than the radius of pattern A4 and smaller in length than that of pattern A5, becomes the fastest.

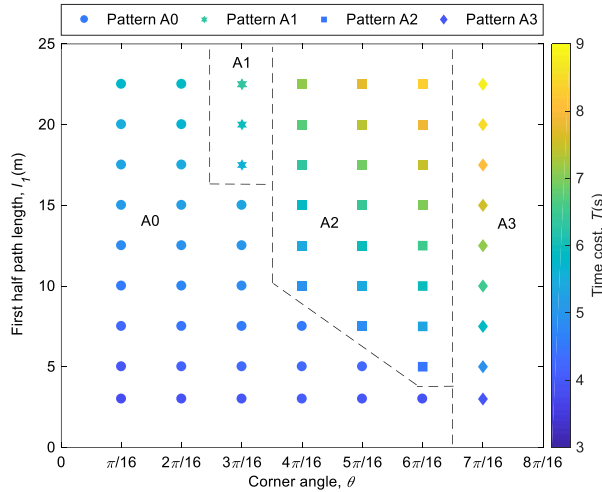


Fig. 4.21 Distribution of least-time patterns of form A with $l_2 = 10$ m and $D = 2.0$ m

Fig. 4.22 shows the distribution of the least-time patterns when D and θ are varied with $l_1 = 8.0$ m and $l_2 = 10$ m. As shown in the graph, pattern A0 is feasible when D is large enough with reference to θ . Otherwise, it is basically advantageous for the vehicle to travel by pattern A2, as shown in Fig. 4.21. In contrast to the distribution shown in Fig. 4.21, pattern A2 has superiority even when θ is large and D is small in Fig. 4.22. This might be because a small D minimizes the divergence of the trajectory from the centerline, and then the traveling distance is decreased. Consequently, pattern A3 becomes the fastest when D is large at the same time that θ approaches $\pi/2$.

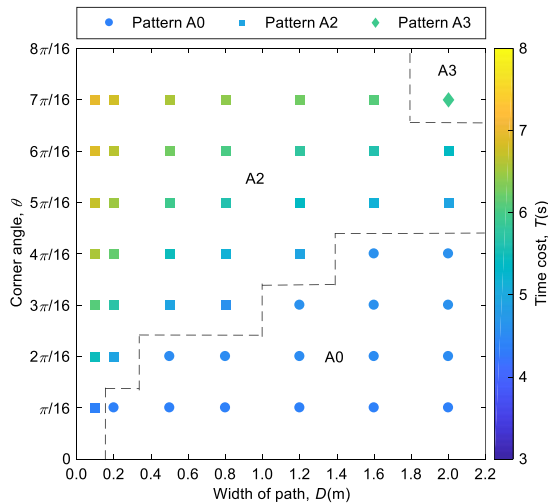


Fig. 4.22 Distribution of least-time patterns of form A with $l_1 = 8.0$ m and $l_2 = 10$ m

In summary, the optimal pattern A0 is feasible when θ or l_1 is small and D is large. Otherwise, pattern A2 is the next best candidate. As an exception, pattern A3 is quickest when θ approaches $\pi/2$ and D is large, and pattern A1 is quickest when l_1 is large and θ is somewhat small.

4.4.2.2 Characteristics of Form B

Fig. 4.23 shows the trajectories for form B with $l_1 = 20$ m and $l_2 = 10$ m. The trajectory of pattern B0 deviates from the path when its width is small [Fig. 4.23(d) and (e)]. In contrast, when the path is relatively wide, the trajectory deviates only when the corner angle is around $\pi/4$ [Fig. 4.23(b)], whereas no deviation occurs when the corner angle is smaller or larger than $\pi/4$ [Fig. 4.23(a) and (c)]. Before point P, the vehicle has to decelerate in the y -axis direction and accelerate in the x -axis direction. Therefore, when the corner angle is large, the acceleration in the x -axis direction becomes large relative to the deceleration in the y -axis direction, and this causes a deviation. When the corner angle is still larger, however, the vehicle accelerates in the x -axis direction slowly because the driving force is almost entirely consumed by the deceleration in the y -axis direction. As a result, the turning maneuver proceeds gradually and the trajectory can avoid deviation from the path.

In these conditions, the trajectory of patterns B1 and B2 are close to each other. It should be noted that the trajectory of pattern B1 is shorter than that of pattern B0 when the corner angle is somewhat large as shown in [Fig. 4.23(c)], which suggests the possibility for pattern B1 to perform better than pattern B0 in form B. Pattern B3 fails to converge to the centerline when the path width is large [Fig. 4.23(b) and (c)]. In contrast, the trajectory stays within the path when its width is small [Fig. 4.23(d) and (e)]. Note that the trajectories that are not shown in the figure, specifically, patterns B1–B3 in Fig. 4.23(a) and pattern B2 in Fig. 4.23(c), do not have a solution.

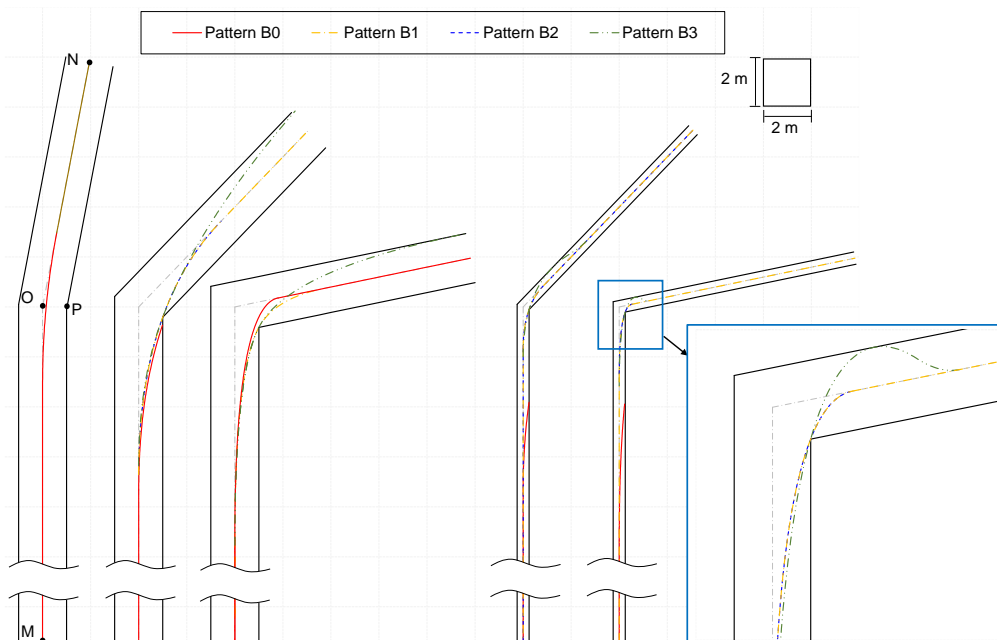


Fig. 4.23 Trajectories of form B when $l_1 = 20$ m, $l_2 = 10$ m, and $D = 2.0$ m. (a) $D = 2.0$ m, $\theta = \pi/16$ (b) $D = 2.0$ m, $\theta = 4\pi/16$ (c) $D = 2.0$ m, $\theta = 7\pi/16$ (d) $D = 0.5$ m, $\theta = 4\pi/16$ (e) $D = 0.5$ m, $\theta = 7\pi/16$.

Here the calculation results are used to discuss the choice of motion patterns. Fig. 4.24 shows the distribution of the least-time patterns of form B when the corner angle θ and the first-half path length l_1 vary with $l_2 = 10$ m and $D = 2.0$ m. Here, pattern B0 costs the least time in most cases. However, when l_1 increases, pattern B0 deviates from the path around $\theta = \pi/4$, as shown in Fig. 4.23(b). In this case, pattern B1 becomes the least-time pattern instead of pattern B0. When l_1 becomes even larger, pattern B2 costs less time than the others. This is thought to be because a larger l_1 increases the initial velocity and consequently requires larger deceleration before turning in pattern B1.

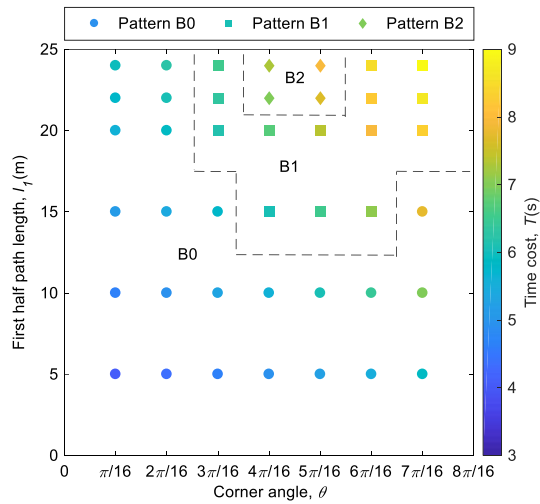


Fig. 4.24 Distribution of least-time patterns of form B with $l_2 = 10$ m and $D = 2.0$ m.

Fig. 4.25 shows the distribution of the least-time patterns when D and θ vary with $l_1 = 8.0$ m and $l_2 = 10$ m. Basically, the time cost of pattern B0 is lower than that of the others when D is sufficiently large. However, when D becomes small, pattern B1 costs the least because the trajectory of pattern B0 leaves the path. Pattern B0 becomes disadvantageous especially when θ approaches $\pi/4$, which is the same result shown in Fig. 4.24. Conversely, when D is small, pattern B2 has the lowest time cost because the effect of the longer moving distance stays relatively small. However, when θ increases under small D , most of the driving force is consumed to adjust the velocity in the u -axis direction in pattern B2, so that pattern B1 becomes the least-time pattern.

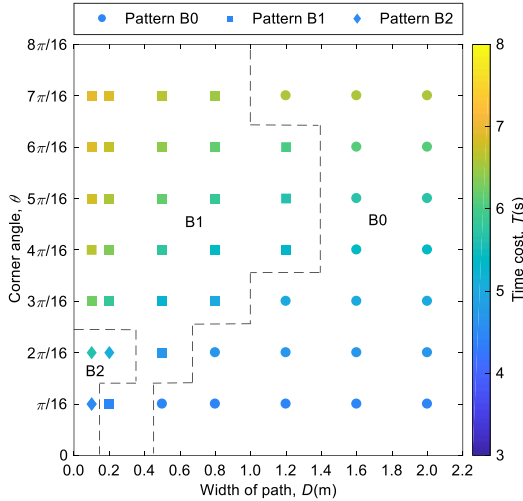


Fig. 4.25 Distribution of least-time patterns of form B with $l_1 = 8.0$ m and $l_2 = 10$ m

In summary, pattern B0 is feasible except around $\theta = \pi/4$ when D is large and l_1 is not. In other cases, pattern B1 has the lowest time cost. When l_1 is large or θ and D are small, pattern B2 shows its advantage.

4.4.2.3 Characteristics of Form C

The traveling motion of form C and its simulation results are similar to those of CWV. When the curve angle is small and the width of the path is large enough, pattern C0 is feasible as far as the vehicle does not deviate from the path. In the other cases, pattern C1 or C2 takes its place. Pattern C1 is better in the shorter moving distance after crossing the centerline, while pattern C2 is better in the less deceleration before turning.

4.4.3 Comparison between CWV and OWV

Based on the results shown in the previous sections, the time cost of the CWV and OWV is compared. As explained above, the width D , length l_1 , l_2 , and the curve angle θ affect the choice of motion patterns. Therefore, the least time cost is compared when these parameters are varied as shown in Fig. 4.26.

First of all, the CWV can travel faster than any form of the OWV as shown in all graphs in Fig. 4.26. This is because the acceleration of the CWV in linear motion is $\sqrt{2}$ times larger than that of the OWV according to Eqs. (4.4) and (4.13), which enables the CWV to travel faster than the OWV. However, the CWV cannot go through the path under some conditions as shown in Fig. 4.26(c). In this situation, the limited l_2 made the CWV unable to finish the rotation during turning by the proposed motion patterns. On the other hand, only form B of the OWV is completed under all path conditions. Form B of the OWV, in which the vehicle adjusts the orientation before turning the

cornering, takes more time costs than other forms, but is suitable to avoid the deviation even under the severe condition of limited l_2 .

The OWV traveled by form A achieves the time cost almost close to that of the CWV in some cases, e.g., at $\theta = 6\pi/16$ in Fig. 4.26(d). This is partly because l_1 is rather smaller than l_2 . When l_1 is small, the linear acceleration before turning is limited. The smaller velocity before turning enables the vehicle to finish traveling without deceleration during turning motion even the curve angle is relatively large. Then, the acceleration in the x -axis direction can be used to the maximum, which contributes to suppressing time cost and getting close to the CWV. However, the CWV fails to travel in this manner when the curve angle becomes still larger, and then the time cost increases again.

In summary, the CWV can travel faster than the OWV because of the higher acceleration capability, while the OWV shows the flexible mobility to go through even the severe curve and the capability to adapt various motion strategies according to various situations.

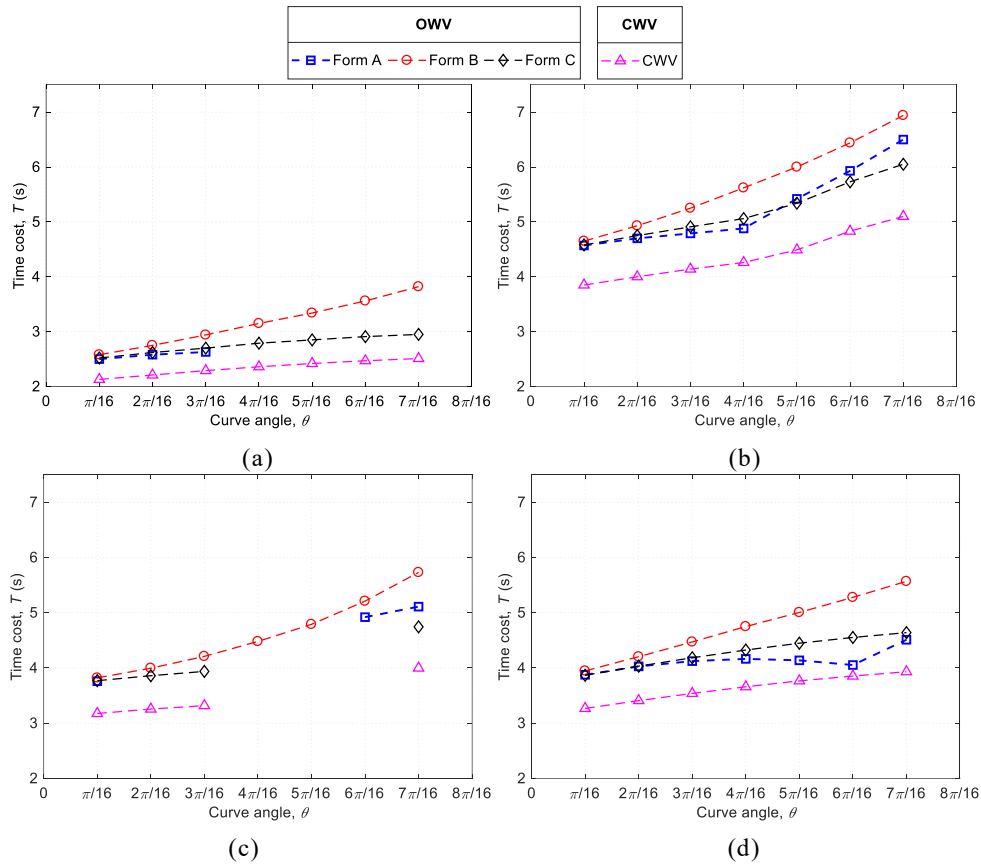


Fig. 4.26 Least time cost comparison between CWV and OWV. (a) $l_1 = 3.0$ m, $l_2 = 3.0$ m, and $D = 2.0$ m, (b) $l_1 = 10$ m, $l_2 = 10$ m, and $D = 2.0$ m, (c) $l_1 = 10$ m, $l_2 = 4.0$ m, and $D = 2.0$ m, (d) $l_1 = 4.0$ m, $l_2 = 10$ m, and $D = 2.0$ m.

4.5 Summary

Previous studies about path planning were primarily conducted on the conventional-wheeled vehicles, while the studies about path planning of omnidirectional-wheeled vehicles are very few and rarely consider the dynamics. Additionally, the omnidirectional-wheeled vehicle can move in any direction immediately. Therefore, various traveling forms are available even for turning a corner according to the timing of changing the vehicle orientation. The characteristics of each traveling form have not yet been explored to detect what kind of traveling form is suitable for what path conditions for what reasons with the consideration of dynamics. To answer this problem, the OWV was chosen as the research subject. The numerical model of the OWV was constructed, based on which analytical motion patterns were set for each traveling form. Then, the time cost was compared through simulation to analyze the advantages of these patterns when the vehicles travel along a designated path with one corner. The above studies were also conducted on the CWV, which was compared with the OWV finally. The following results were gained.

- Three traveling forms for an OWV were proposed based on their kinetic models by considering the order of rotation and turning: form A, rotation after turning; form B, rotation before turning; and form C, rotation during turning. The possible patterns of these traveling forms were set theoretically based on the magnitude of acceleration and the necessity of deceleration.
- The motion patterns of each traveling form were analyzed when the traveling area conditions, including the corner angle, path width, and path length, were varied. The time-optimal patterns were suggested as the traveling strategy for the OWV. The time cost was the smallest when the vehicle can run without deceleration before turning (A0, B0, and C0), which was available when the path was wide and the corner angle was small. When both the path width and angle were small, the pattern in which the vehicle turned with a large radius (A2, B2, and C2) was optimal because it maintained the highest possible velocity during turning. When the corner angle was large and the path length before the corner was larger than that after the corner, the pattern with the lowest time cost switched to the one in which the vehicle turned with a small radius by decelerating before turning (A3, B1, and C1).
- Three motion patterns for the CWV were proposed based on its kinetic model including pattern R0 (without deceleration), pattern R1 (with deceleration), and pattern R2 (with small deceleration and overshoot). The characteristics of each pattern were analyzed through the simulation. The time-optimal pattern tended to change from pattern R0 to

R2 and then to R1 as the curve angle became large. When the width of the path was relatively small, pattern R2 cost the least time with a small curve angle, while pattern R1 took its place when the curve angle was close to $\pi/2$.

- The time cost of the CWV was compared with that of the OWV quantitatively. The result showed that the CWV traveled faster than the OWV in most situations. However, the OWV had more available solutions even when the path condition was severe.

Chapter 5

Traveling Stability of Omnidirectional Single-Track Vehicle in Roll Direction

5.1 Introduction

According to the ground track left by the vehicle when it moves forward, it is divided into a double-track vehicle and a single-track vehicle. Compared with three- or four-wheeled automobiles, single-track vehicles have high maneuverability even in a narrow passage or on a winding road. The conventional single-track vehicles equipped with tired wheels need to make turns or switchbacks when moving toward specific directions, for example, left or right, which reduces their maneuvering efficiency when moving in a limited space or avoiding obstacles. In contrast, it is possible for single-track vehicles equipped with omnidirectional-wheeled mechanisms to move in any direction arbitrarily, which makes them move conveniently even on a narrow passage. However, the studies about the omnidirectional-wheeled single-track vehicle were rarely reported. In Chapter 2, the analysis results showed that the two-wheeled vehicle equipped with double AOWs or an AOW and other wheels could realize three-DOF mobility. However, the velocity of the vehicle equipped with an AOW and other wheels is smaller and has a singularity. Therefore, two AOWs are applied to construct the omnidirectional single-track vehicle.

The single-track vehicle equipped with two double-row active omni wheels (DAOW) is chosen as the research object. The DAOW is introduced in the below. During traveling with the conventional AOW, however, vibration in the vertical direction occurs because of the gaps between the outer rollers, which seriously degrades the riding comfort. To solve this problem, Terakawa et al. proposed a novel AOW with double-row outer rollers, which had the same kinematic characteristics as the previous AOW [82]. The structure of the new AOW is shown in Fig. 5.1. The driving mechanism is the same as that of the conventional AOW, while the outer rollers are changed to a barrel shape, which realizes a seamless periphery. The barrel-shaped outer rollers are staggered on the left and right sides, which eliminates the gaps created by the roller support. Consequently, the new AOW can travel smoothly without vertical vibration. Because of the above merits, the proposed double-row AOW (DAOW) is a good solution for a single-track vehicle to realize omnidirectional mobility.

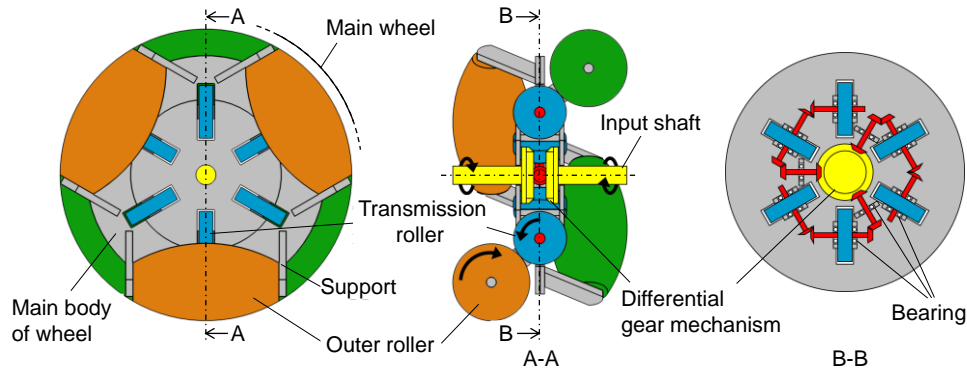


Fig. 5.1 Structure of new AOW with double row of outer rollers [82].

Since the single-track vehicle itself is unstable and easy to fall down in the roll direction, traveling stability is an important problem of the single-track vehicle. Previous studies tried to keep a bicycle or motorcycle equipped with conventional tired wheels stable through a stability controller by using steering adjustments [91-92]. On the other hand, the steering function is not necessary for a single-track vehicle with the DAOWs, so that the existing stabilization method is no longer available. The flywheel devices can be used for the stabilization control, but it leads the vehicle structure to a complicated and large one [93]. Therefore, a novel stabilization method for the single-track vehicle with the DAOWs is required. The structure of DAOW is special, because of which its effect on the rolling stability is unknown.

With these issues in mind, this chapter investigates the dynamical behavior of the DAOW. The DAOW has a double-row structure so that the ground contact point switches between the right and left sides alternately during traveling just like a bipedal motion. This phenomenon may enable the single-track vehicle with two DAOWs to travel stably without active balance control. Then, the possibility and stabilization conditions are verified and clarified. As the first step, the present study focuses on stability in the roll direction when the vehicle travels forward. The kinetic contact model of a vehicle with two DAOWs is discussed first. Next, a simulation based on the contact model is conducted to elucidate the effect of the switching mechanism of the double-row structure. Finally, a prototype vehicle is developed and used for experiments to verify the simulation results and the feasibility of stable travel.

5.2 Kinetic Contact Model of Single-track vehicle

This section discusses the kinetic contact model of a single-track vehicle with two DAOWs.

5.2.1 Model of Vehicle

The basic structure of the single-track vehicle with two DAOWs is shown in Fig. 5.2. The front and rear DAOWs are identical. In the analysis, it is assumed that the wheels always rotate with the same phase.

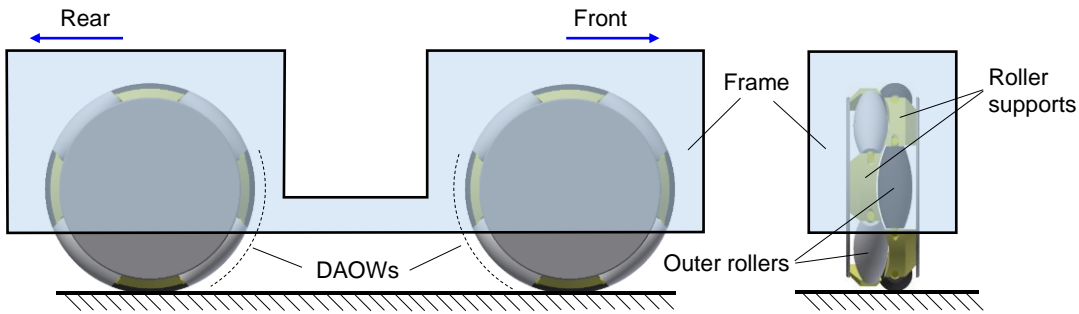


Fig. 5.2. Model of single-track vehicle with two DAOWs

To explain the DAOW kinetic model more simply, it is assumed that the outer roller acts like a blade without width or mass, as shown in Fig. 5.3(a). The outer roller is considered to be a spring-damper system, as shown in Fig. 5.3(b), where the spring constant and damping coefficient are k and c , respectively. The deformation of the outer roller at the contact point is defined as p , whose positive direction is the extension direction. The outer roller is assumed to deform only in the vertical direction, while the horizontal deformation is ignored, even when the vehicle leans to any side. The outer rollers are assumed to contact the ground at a point instead of a surface.

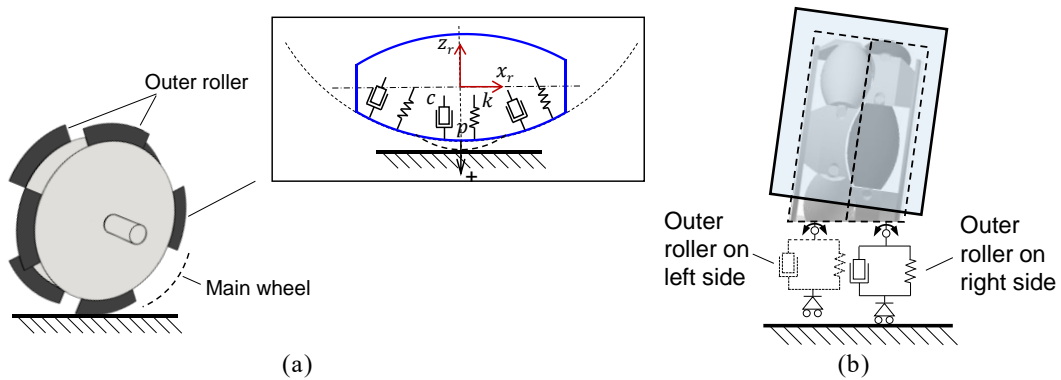


Fig. 5.3 Viscoelasticity model of the outer roller. (a) Spring-damper system of the outer roller, (b) Spring-damper system of the whole wheel

Next, the displacement analysis is discussed. A right-hand orthogonal coordinate system Σ_0 is set with the origin at the projected point of the center of gravity (COG) on the ground, as shown in Fig. 5.4(a), where the XY plane coincides with the ground and the X -axis is parallel to the forward/backward direction of the vehicle when both DAOWs contact the ground. A coordinate system Σ_r is established for the outer roller that is currently in contact with the ground, and its

origin is set to be the center of the outer roller, as shown in Fig. 5.4(b). The x_r axis is the central axis of the outer roller. The z_r axis is parallel to the radial direction of the main wheel. At this time, the coordinates for the contact point in Σ_r can be written as

$$\begin{bmatrix} x \\ y \\ z \end{bmatrix} = \begin{bmatrix} R \sin \delta \\ 0 \\ R(1 - \cos \delta) - r_0 \end{bmatrix} \quad \left(-\frac{\pi}{N} \leq \delta \leq \frac{\pi}{N}\right), \quad (5.1)$$

where r_0 is the maximum radius of the outer roller, R is the radius of the main wheel, N is the number of the outer rollers, and δ is the central angle between the contact point and the maximum radius section of the outer roller.

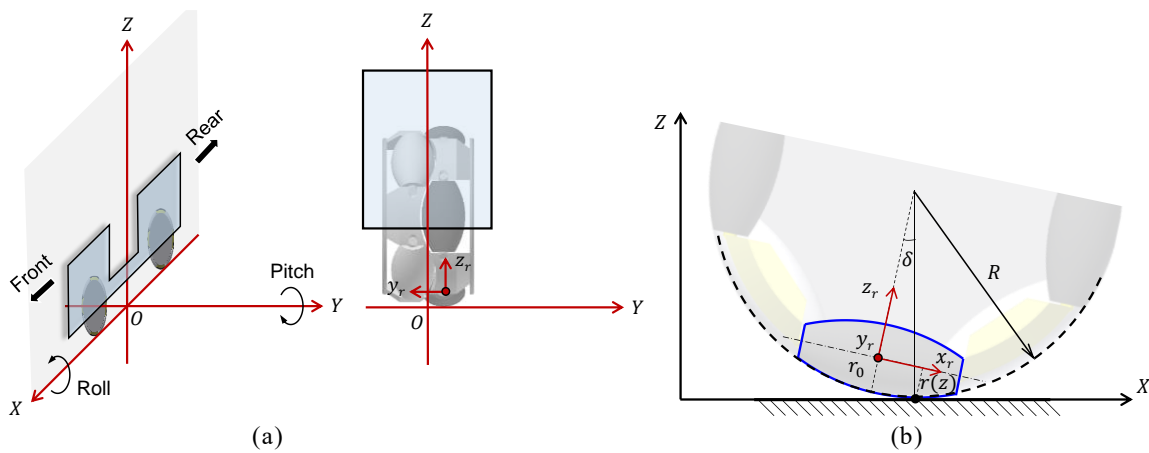


Fig. 5.4 Coordinate systems for analysis. (a) Coordinate system of vehicle, (b) Coordinate system of outer roller.

The tilt of the vehicle in the pitch and roll directions is considered as shown in Fig. 5.5. The distance from the axis of the outer roller to the center plane of the main wheel is defined as d_w . The distance from the axle of the main wheel to the COG of the vehicle in the vertical state is h_0 . The distance between the centers of the front wheel and rear wheel is ρ . The displacements of the COG in the X -, Y -, and Z -axis directions are C , K , and H , respectively. The angular displacements of the vehicle in the roll and pitch directions are ϕ and ψ , respectively. The rotational velocity of the main wheel is $\dot{\theta}$, which is assumed to be the same for the front and rear wheels at all times.

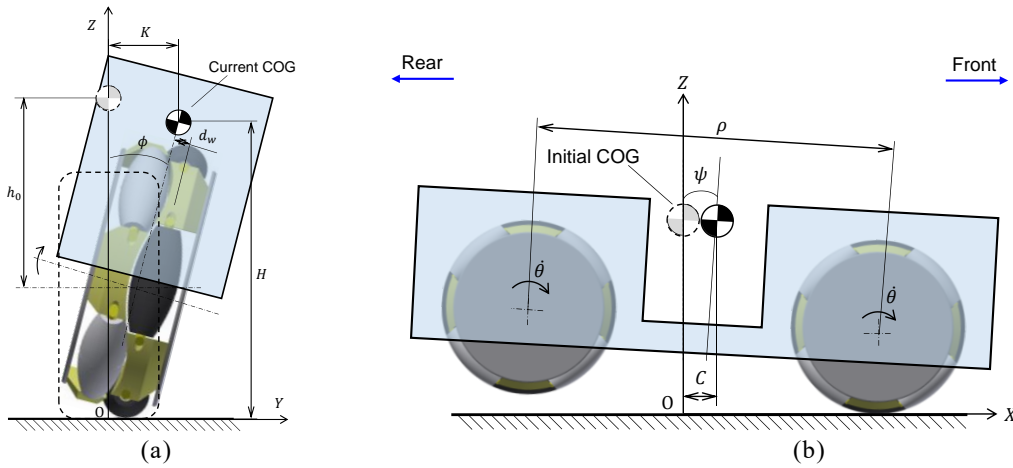


Fig. 5.5 Tilt of the vehicle. (a) Rear view, (b) Lateral view.

5.2.2 Kinetic Contact Model of Vehicle

As the main wheel rotates, the contact state between the wheel and the ground changes. Namely, the right-side and left-side outer roller have alternating contact with the ground either at the outer surface or end surface, as shown in Fig. 5.6(a). The kinetic contact model of the vehicle is discussed in this section. When contact happens at the outer surface of the outer roller, the number of contact points can be one or two per DAOW, as shown in Fig. 5.6(b). At this time, the contact point is either on the right-side or left-side outer roller. Here, the displacement of the COG is represented as follows:

$$\begin{cases} \text{if the right - side outer roller contacts the ground:} \\ C = C_{ri}, K = K_{ri}, H = H_{ri}, i = 1, 2 \\ \text{if the left - side outer roller contacts the ground:} \\ C = C_{li}, K = K_{li}, H = H_{li}, i = 1, 2 \end{cases} \quad (5.2)$$

where C_{ri} , K_{ri} , and H_{ri} are the displacements of the COG when the right-side outer roller contacts the ground, and C_{li} , K_{li} , and H_{li} are the displacements of the COG when the left-side outer roller contacts the ground. The index $i = 1$ represents the situation where the front wheel contacts the ground, while $i = 2$ represents the situation where the rear wheel contacts the ground.

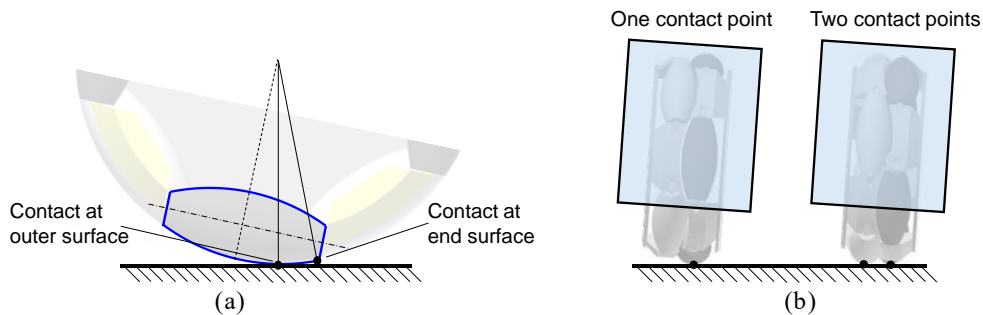


Fig. 5.6 Contact points between the roller and ground. (a) Position of contact point, (b) Number of contact points.

5.2.2.1 Situation with One Contact Point

In most cases, one contact point exists between the front or rear wheel and the ground. When this contact point is on the right-side outer roller, the displacement of the COG can be calculated as follows (see Appendix A):

$$\begin{cases} C_{r1} = \{h_0 \cos \phi + d_w \sin \phi\} \sin \psi + (R - r_0) \sin \delta + \frac{\rho}{2}(1 - \cos \psi) - X_r + R \left(\dot{\theta}_0 t + \frac{\ddot{\theta}}{2} t^2 \right) \\ C_{r2} = \{h_0 \cos \phi + d_w \sin \phi\} \sin \psi + (R - r_0) \sin \delta - \frac{\rho}{2}(1 - \cos \psi) - X_r + R \left(\dot{\theta}_0 t + \frac{\ddot{\theta}}{2} t^2 \right) \\ K_{r1} = K_{r2} = -h_0 \sin \phi + d_w (\cos \phi - 1) - (R - r_0) \sin \phi \cos \delta \\ H_{r1} = \{h_0 \cos \psi + (R - r_0) \cos \delta\} \cos \phi + d_w \sin \phi \cos \psi + \frac{\rho}{2} \sin \psi + p_{r1} - Z_r \\ H_{r2} = \{h_0 \cos \psi + (R - r_0) \cos \delta\} \cos \phi + d_w \sin \phi \cos \psi - \frac{\rho}{2} \sin \psi + p_{r2} - Z_r \end{cases}, \quad (5.3)$$

where X_r and Z_r are the distances from the contact point to the origin of the coordinate system Σ_r in the x_r -axis and z_r -axis directions, respectively. $\dot{\theta}_0$ is the initial rotational velocity of the main wheel, $\ddot{\theta}$ is the rotational acceleration of the main wheel, t is the elapsed time, and p_{r1} and p_{r2} are the deformations of the contacting right-side outer rollers of the front and rear wheels, respectively. When the contact point is on the left-side outer roller, the displacement of the COG can be calculated similarly. In this case, the index l is used instead of r for each parameter. $H_{r1} = H_{r2}$ and $H_{l1} = H_{l2}$ are assumed to be true all the time.

If there is no slip between the outer rollers and the ground, then $K_{r1} = K_{l2}$, $K_{l1} = K_{r2}$, $C_{r1} = C_{r2}$, and $C_{l1} = C_{l2}$. The angular displacement in the roll direction is uniquely defined by the rotation angular of main wheel under this condition, which contradicts conditions during actual operation. Therefore, either the front wheel or rear wheel should be considered to be slipping. Here, the normal force is evaluated. The normal force on the contacting outer roller can be calculated by

$$\begin{cases} F_{ri} = -c\dot{p}_{ri} - kp_{ri} & i = 1, 2 \\ F_{li} = -c\dot{p}_{li} - kp_{li} & i = 1, 2' \end{cases} \quad (5.4)$$

where F_{ri} and F_{li} represent the normal force applied to the right-side and left-side outer rollers, respectively. The outer roller with a smaller normal force is considered to be slipping. The conditions for the non-slipping outer roller are used to calculate the equation of motion. The friction force is ignored because the slipping distance is small.

Therefore, the Lagrange function can be written as follows:

$$\begin{cases}
\frac{d}{dt} \left(\frac{\partial L}{\partial \dot{\phi}} \right) - \left(\frac{\partial L}{\partial \phi} \right) = 0 \\
\frac{d}{dt} \left(\frac{\partial L}{\partial \dot{p}_1} \right) - \left(\frac{\partial L}{\partial p_1} \right) + \left(\frac{\partial G}{\partial p_1} \right) = 0 \\
\frac{d}{dt} \left(\frac{\partial L}{\partial \dot{p}_2} \right) - \left(\frac{\partial L}{\partial p_2} \right) + \left(\frac{\partial G}{\partial p_2} \right) = 0 \\
L = \frac{M}{2} \left[\left(\frac{dC}{dt} \right)^2 + \left(\frac{dK}{dt} \right)^2 + \left(\frac{dH}{dt} \right)^2 \right] + \frac{I_{XX}}{2} \dot{\phi}^2 + \frac{I_{YY}}{2} \dot{\psi}^2 - Mgh - \frac{k}{2} (p_1^2 + p_2^2) \\
G = \frac{c}{2} (\dot{p}_1^2 + \dot{p}_2^2) \\
p_1 = p_{r1} \text{ if } F_{r1} > F_{l1}, \quad p_1 = p_{l1} \text{ if } F_{r1} < F_{l1} \\
p_2 = p_{r2} \text{ if } F_{r2} > F_{l2}, \quad p_2 = p_{l2} \text{ if } F_{r2} < F_{l2}
\end{cases} \quad (5.5)$$

where L is the Lagrangian, G is a dissipation function, M is the mass of the vehicle, I_{XX} and I_{YY} are the inertia moments around the COG about the X -axis and Y -axis, respectively, p_1 and p_2 are the deformations of the front wheel and rear wheel, respectively. The parameters C , K , and H for the non-slipping outer roller are applied in the equation.

For simplicity, the wheel is assumed to receive an impulsive force from the ground during the switching of the slipping outer rollers. According to the conservation of momentum, the variation of the translational velocity and tilt angular velocity in the X -axis and Y -axis directions is given by the following equation:

$$\begin{cases}
\int F_X dt = M(\dot{C}_A - \dot{C}_B) \\
\int F_X \cdot H dt = I_{XX}(\dot{\psi}_A - \dot{\psi}_B) \\
\int F_Y dt = M(\dot{K}_A - \dot{K}_B) \\
\int F_Y \cdot H dt = I_{YY}(\dot{\phi}_A - \dot{\phi}_B)
\end{cases}, \quad (5.6)$$

where F_X and F_Y are the impulsive forces in the X -axis and Y -axis directions, respectively, \dot{C}_B and \dot{K}_B are the translational velocities before switching in the X -axis and Y -axis directions, respectively, \dot{C}_A and \dot{K}_A are the translational velocities after switching in the X -axis and Y -axis directions, respectively, $\dot{\psi}_B$ and $\dot{\phi}_B$ are the angular velocities before switching in the pitch and roll directions, respectively, and $\dot{\psi}_A$ and $\dot{\phi}_A$ are the angular velocities after switching in the pitch and roll directions, respectively.

5.2.2.2 Situation with Two Contact Points

When the outer roller contacts the ground on one side, the roller on the other side, which has no ground contact at that time, eventually contacts the ground because of rotation of the main wheel. The number of contact points becomes two at this moment. The situation where either or both of the front and rear wheels has two contact points is discussed in this section.

When the right-side outer roller of the front wheel contacts the ground at one point and that of the rear wheel contacts the ground at two points, the Lagrangian and dissipation functions are as follows:

$$\begin{cases} L = \frac{M}{2} \left[\left(\frac{dH}{dt} \right)^2 + \left(\frac{dK}{dt} \right)^2 + \left(\frac{dC}{dt} \right)^2 \right] + \frac{I_{XX}}{2} \dot{\phi}^2 + \frac{I_{YY}}{2} \dot{\psi}^2 - Mgh - \frac{k}{2} (p_{r1}^2 + p_{r2}^2 + p_{l2}^2) \\ G = \frac{c}{2} (\dot{p}_{r1}^2 + \dot{p}_{r2}^2 + \dot{p}_{l2}^2) \end{cases} \quad (5.7)$$

Conditions in which three points are in contact with the ground can be handled in the same way.

When both of the front and rear wheels contact the ground at two points, the Lagrangian and dissipation functions are as follows:

$$\begin{cases} L = \frac{M}{2} \left[\left(\frac{dH}{dt} \right)^2 + \left(\frac{dK}{dt} \right)^2 + \left(\frac{dC}{dt} \right)^2 \right] + \frac{I_{XX}}{2} \dot{\phi}^2 + \frac{I_{YY}}{2} \dot{\psi}^2 - Mgh - \frac{k}{2} (p_{r1}^2 + p_{r2}^2 + p_{l1}^2 + p_{l2}^2) \\ G = \frac{c}{2} (\dot{p}_{r1}^2 + \dot{p}_{r2}^2 + \dot{p}_{l1}^2 + \dot{p}_{l2}^2) \end{cases} \quad (5.8)$$

Similar to the situation with one contact point discussed in the previous section, the outer roller on one side, whose normal force is smaller, is assumed to be slipping. For instance, when the right-side outer roller of the front wheel contacts the ground at one point and the rear wheel contacts the ground at two points, the Lagrange function can be written as:

$$\begin{cases} \frac{d}{dt} \left(\frac{\partial L}{\partial \dot{\phi}} \right) - \left(\frac{\partial L}{\partial \phi} \right) + \left(\frac{\partial G}{\partial \dot{\phi}} \right) = 0 \\ \frac{d}{dt} \left(\frac{\partial L}{\partial \dot{p}_{r1}} \right) - \left(\frac{\partial L}{\partial p_{r1}} \right) + \left(\frac{\partial G}{\partial \dot{p}_{r1}} \right) = 0 \\ \frac{d}{dt} \left(\frac{\partial L}{\partial \dot{p}_{l2}} \right) - \left(\frac{\partial L}{\partial p_{l2}} \right) + \left(\frac{\partial G}{\partial \dot{p}_{l2}} \right) = 0 \quad \text{if } F_{r2} < F_{l2} \\ \frac{d}{dt} \left(\frac{\partial L}{\partial \dot{p}_{r2}} \right) - \left(\frac{\partial L}{\partial p_{r2}} \right) + \left(\frac{\partial G}{\partial \dot{p}_{r2}} \right) = 0 \quad \text{if } F_{r2} > F_{l2} \end{cases} \quad (5.9)$$

When both wheels contact the ground at two points, the Lagrange function is given in the same way as above. The parameters applied in the Lagrange function are determined by comparing the normal force. Calculating the switching of the slipping side is done in the same way as described in section 5.2.2.1.

5.2.2.3 Situation with No Contact Points

The displacement of the outer roller due to viscoelasticity changes rapidly as the rotational velocity of the main wheel increases, which leads to a large normal force. At this time, the deformation due to viscoelasticity cannot catch up with the rising acceleration of the COG, and then the wheel floats in the air very briefly. Such a situation is discussed in this section.

The outer roller with a negative normal force is considered to lose contact with the ground. The distance of the outer roller from the nearest point to the ground is defined as s in the suspended state, as shown in Fig. 5.7.

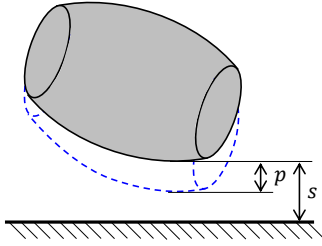


Fig. 5.7 Status of suspended outer roller

The height of the COG when the wheel leaves the ground is given as follows:

$$\begin{cases} \text{if the front wheel is suspended:} \\ H_{r1} = \{h_0 \cos \psi + (R - r_0) \cos \delta\} \cos \phi + d_w \sin \phi \cos \psi + \frac{\rho}{2} \sin \psi + s_1 - Z_r \\ \text{if the rear wheel is suspended:} \\ H_{r2} = \{h_0 \cos \psi + (R - r_0) \cos \delta\} \cos \phi + d_w \sin \phi \cos \psi - \frac{\rho}{2} \sin \psi + s_2 - Z_r \end{cases} \quad (5.10)$$

When either the front or rear wheel leaves the ground and the other contacts the ground at one point, the Lagrangian and dissipation functions are as follows:

$$\begin{cases} L = \frac{M}{2} \left[\left(\frac{dH}{dt} \right)^2 + \left(\frac{dK}{dt} \right)^2 + \left(\frac{dC}{dt} \right)^2 \right] + \frac{I_{XX}}{2} \dot{\phi}^2 + \frac{I_{YY}}{2} \dot{\psi}^2 - MgH - \frac{k}{2} (p_1^2 + p_2^2) \\ G = \frac{c}{2} (\dot{p}_1^2 + \dot{p}_2^2) \end{cases} \quad (5.11)$$

The displacement of the COG of the contacting wheel is applied to the equation of motion. Therefore, the Lagrange function can be written as

$$\begin{cases} \frac{d}{dt} \left(\frac{\partial L}{\partial \dot{\phi}} \right) - \left(\frac{\partial L}{\partial \phi} \right) = 0 \\ \frac{d}{dt} \left(\frac{\partial L}{\partial \dot{p}_1} \right) - \left(\frac{\partial L}{\partial p_1} \right) + \left(\frac{\partial G}{\partial p_1} \right) = 0 \\ \frac{d}{dt} \left(\frac{\partial L}{\partial \dot{p}_2} \right) - \left(\frac{\partial L}{\partial p_2} \right) + \left(\frac{\partial G}{\partial p_2} \right) = 0 \\ \frac{d}{dt} \left(\frac{\partial L}{\partial \dot{s}_1} \right) - \left(\frac{\partial L}{\partial s_1} \right) + \left(\frac{\partial G}{\partial s_1} \right) = 0 \quad \text{if the front wheel is suspended} \\ \frac{d}{dt} \left(\frac{\partial L}{\partial \dot{s}_2} \right) - \left(\frac{\partial L}{\partial s_2} \right) + \left(\frac{\partial G}{\partial s_2} \right) = 0 \quad \text{if the rear wheel is suspended} \end{cases} \quad (5.12)$$

When both the front and rear wheels leave the ground at the same time, the COG cannot move in the X -axis or Y -axis direction because there is no external force. Therefore, the transfer velocity \dot{C} , \dot{K} , and angular velocity $\dot{\phi}$, $\dot{\psi}$ remain unchanged. Then, the Lagrange function can be written as

$$\begin{cases} \frac{d}{dt} \left(\frac{\partial L}{\partial \dot{p}_1} \right) - \left(\frac{\partial L}{\partial p_1} \right) + \left(\frac{\partial G}{\partial p_1} \right) = 0 \\ \frac{d}{dt} \left(\frac{\partial L}{\partial \dot{p}_2} \right) - \left(\frac{\partial L}{\partial p_2} \right) + \left(\frac{\partial G}{\partial p_2} \right) = 0 \\ \frac{d}{dt} \left(\frac{\partial L}{\partial \dot{s}_1} \right) - \left(\frac{\partial L}{\partial s_1} \right) + \left(\frac{\partial G}{\partial s_1} \right) = 0 \\ \frac{d}{dt} \left(\frac{\partial L}{\partial \dot{s}_2} \right) - \left(\frac{\partial L}{\partial s_2} \right) + \left(\frac{\partial G}{\partial s_2} \right) = 0 \\ s_0 = p_0, \dot{s}_0 = \dot{p}_0 \end{cases} \quad (5.13)$$

where s_1 and s_2 are the smallest distance from the ground to the outer roller of the front and rear wheels, respectively, and s_0 and p_0 are the initial height and deformation at the moment that the wheels start to leave the ground, respectively. Here, $s_0 = p_0$ and $\dot{s}_0 = \dot{p}_0$ are given because it is assumed that H and \dot{H} remain unchanged at the beginning and end of the suspended state.

When either the front or rear wheel leaves the ground and the other contacts the ground at two points, for instance, when only the front wheel contacts the ground at two points, the Lagrangian and dissipation functions are as follows:

$$\begin{cases} L = \frac{M}{2} \left[\left(\frac{dH}{dt} \right)^2 + \left(\frac{dK}{dt} \right)^2 + \left(\frac{dC}{dt} \right)^2 \right] + \frac{I_{XX}}{2} \dot{\phi}^2 + \frac{I_{YY}}{2} \dot{\psi}^2 - MgH - \frac{k}{2} (p_2^2 + p_{r1}^2 + p_{l1}^2) \\ G = \frac{c}{2} (\dot{p}_2^2 + \dot{p}_{r1}^2 + \dot{p}_{l1}^2) \end{cases} \quad (5.14)$$

The displacement of the non-slipping outer roller is applied to establish the Lagrange equation. Therefore, the Lagrangian under this condition is as follows:

$$\begin{cases} \frac{d}{dt} \left(\frac{\partial L}{\partial \dot{\phi}} \right) - \left(\frac{\partial L}{\partial \phi} \right) + \left(\frac{\partial G}{\partial \dot{\phi}} \right) = 0 \\ \frac{d}{dt} \left(\frac{\partial L}{\partial \dot{p}_{r2}} \right) - \left(\frac{\partial L}{\partial p_{r2}} \right) + \left(\frac{\partial G}{\partial \dot{p}_{r2}} \right) = 0 \\ \frac{d}{dt} \left(\frac{\partial L}{\partial \dot{s}_2} \right) - \left(\frac{\partial L}{\partial s_2} \right) + \left(\frac{\partial G}{\partial \dot{s}_2} \right) = 0 \\ \frac{d}{dt} \left(\frac{\partial L}{\partial \dot{p}_{l1}} \right) - \left(\frac{\partial L}{\partial p_{l1}} \right) + \left(\frac{\partial G}{\partial \dot{p}_{l1}} \right) = 0 & \text{if } -c\dot{p}_{r1} - kp_{r1} < -c\dot{p}_{l1} - kp_{l1} \\ \frac{d}{dt} \left(\frac{\partial L}{\partial \dot{p}_{r1}} \right) - \left(\frac{\partial L}{\partial p_{r1}} \right) + \left(\frac{\partial G}{\partial \dot{p}_{r1}} \right) = 0 & \text{if } -c\dot{p}_{r1} - kp_{r1} > -c\dot{p}_{l1} - kp_{l1} \end{cases} \quad (5.15)$$

It is assumed that the wheel receives an impulsive force from the ground when it is in contact with the ground. Therefore, the velocities after contacting the ground can be calculated similarly to Eq. (5.6).

5.3 Motion Simulation of Single-track Vehicle

The model described in Section 5.2 is used to conduct a simulation and investigate the stability of a single-track vehicle with two DAOWs in the roll direction. In the simulation, the following conditions are assumed: the right-side outer rollers of the front and rear wheels initially contact the ground. The vehicle travels at a specific velocity without acceleration, and the front and rear wheels rotate with the same phase. When $|\phi| > \pi/8$ rad, the vehicle is considered to fall over and the calculation is ended. The time interval Δt for the calculation is 0.0001 s. The simulations are performed by using MATLAB R2018b on a workstation with Intel Xeon E-2174G CPU and 24 GB RAM. The parameters applied in the simulation are shown in Table 5.1. The spring and damper coefficients were calculated with the assumption that the outer roller acts according to the Voigt model [93-94]. The flowchart of the simulation is shown in Fig. 5.8.

Table 5.1 Simulation parameters

Symbol	Value	Symbol	Value
M	85 kg	d_w	0.0175 m
I_{XX}	31.1421 kg · m ²	ρ	0.912 m
I_{YY}	36.0157 kg · m ²	k	5.0×10^7 N/m
R	0.15 m	c	2.5×10^5 N · s/m
r_0	0.025 m	N	8
$\ddot{\theta}$	0 rad/s ²	Δt	0.0001 s
h_0	0.1 m	g	9.81 m/s ²

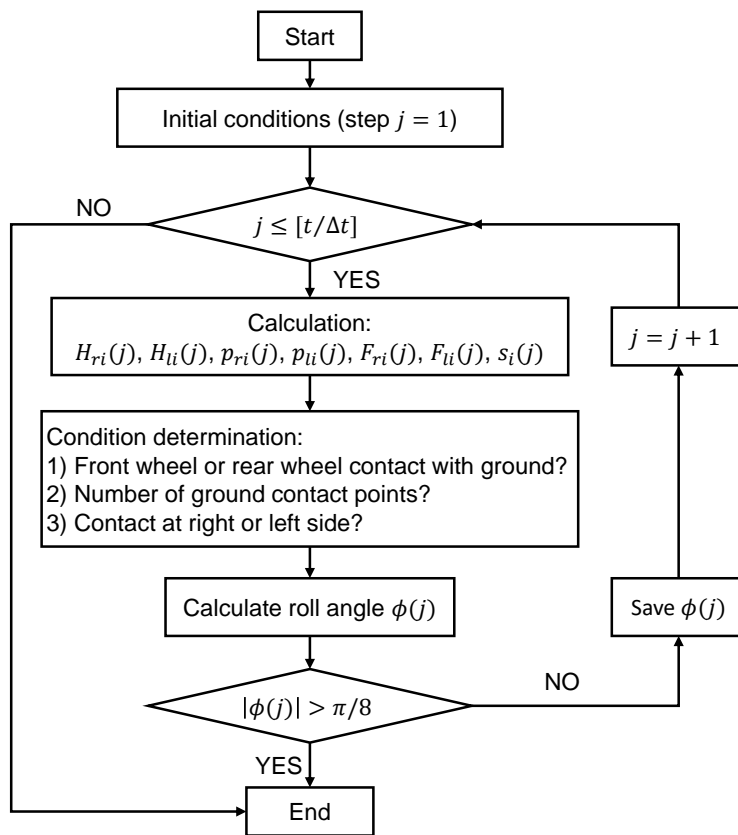


Fig. 5.8 Flowchart of simulation

5.3.1 Traveling Stability

Fig. 5.9 shows the variation of the roll angle ϕ of the vehicle when it travels at $\dot{\theta} = 5$ rad/s. A positive value of the roll angle represents the vehicle leaning to the right, while a negative value indicates a left lean. The initial roll angle ϕ_0 is varied as $\phi_0 = 0, -0.005,$ and -0.01 rad.

The result shows that the vehicle with DAOWs can keep traveling without falling down for at least 10 s. It should be noted that no control is applied to the vehicle to prevent it from tipping over. In addition, the vehicle remains stable even if it starts traveling under a tilted state ($\phi_0 \neq 0$ rad).

This means that the vehicle has an intrinsic function of generating dynamic stability when traveling. In the case of a single-track vehicle with conventional tired wheels, it is difficult to keep traveling without falling over for such a long time without balancing control. Therefore, the result indicates that the single-track vehicle with DAOWs could have traveling stability higher than that of a vehicle with conventional tired wheels. DAOWs contact the ground discontinuously because the left-side and right-side outer rollers contact the ground alternately during wheel rotation. At first glance, this discontinuous contact of the DAOWs seems to have a negative impact on stability, but it actually has a positive effect.

As shown in Fig. 5.9, the roll angle alternates between positive and negative values in each case, which is shown as a composition of the large and small waveforms. This means that the vehicle repeatedly returns to one side after leaning to the other side with small swings. At this time, the roll angle remains within the range of $|\phi| < 0.02$ rad.

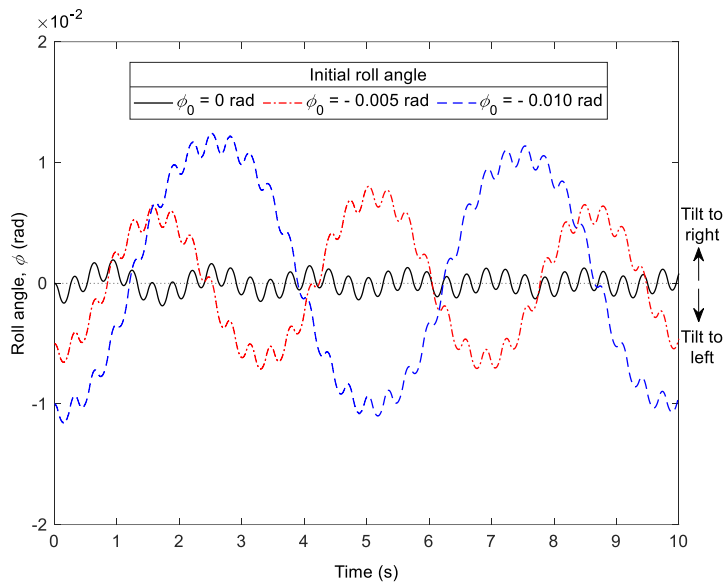


Fig. 5.9 Roll angle of the vehicle when it travels at $\dot{\theta} = 5$ rad/s

5.3.2 Analysis of Traveling Stability Mechanism

To identify the factors that affect traveling stability, the detailed analyses are conducted. Fig. 5.10 shows the variation of the roll angle when the vehicle travels at different velocities, where the tilt angle of the vehicle is set to $\phi_0 = 0$ rad in the initial state. The result indicates that the vehicle travels stably for 5 s except for $\dot{\theta} = 80$ rad/s, in which the vehicle tilts to one side and never returns to the normal position. Based on this result, the mechanism of traveling stability is discussed in this section.

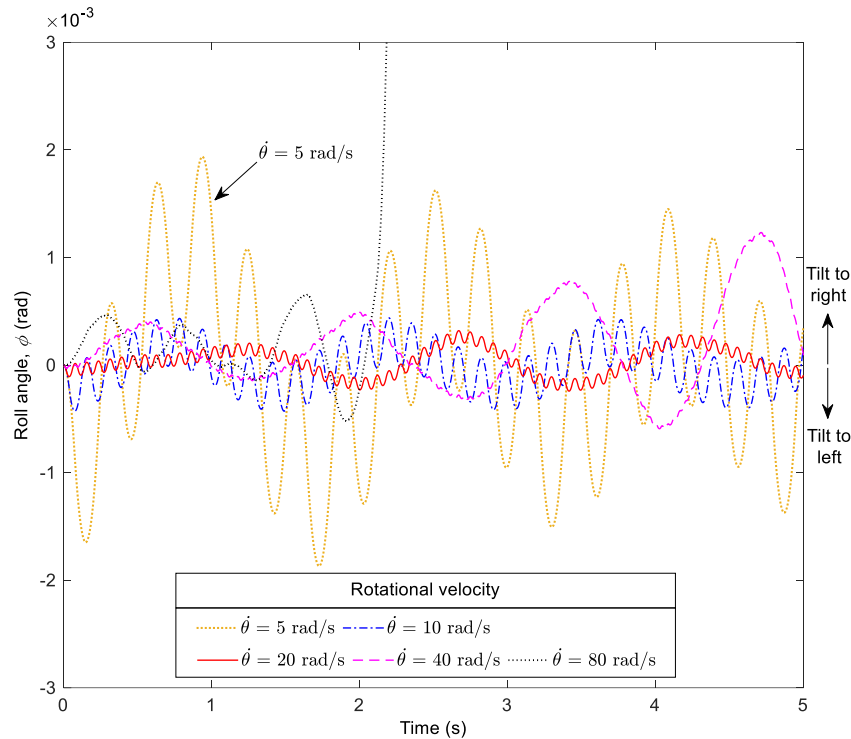


Fig. 5.10 Roll angle of vehicle when it travels at different velocities

As in Fig. 5.9, the variation of the roll angle in Fig. 5.10 contains small and large waveforms in each case. The small waveforms are thought to represent the alternating roller-ground contact on each wheel, while the large waveforms mean that the vehicle's main body swinging from side to side. Fig. 5.11 shows the contact status of the outer rollers in the case of $\dot{\theta} = 5 \text{ rad/s}$ in Fig. 5.10. Note that only the simulation results for the front wheel are discussed because the phases of the front and rear wheels are identical. The red bands represent the state where the right-side outer roller contacts the ground, while the blue bands represent the state where the left-side outer roller contacts the ground. The figure shows that the small waveform has an upward convex shape when the right-side outer roller contacts the ground, while it has a downward convex shape when the left-side outer roller contacts the ground. This behavior can be explained as follows. The right-side outer roller contacts the ground first, namely, the contact point exits on the right of the COG of the vehicle, so that the rotation torque around the COG due to the normal force makes the vehicle tilt to the left side. Subsequently, as the wheel continues to rotate, the left-side outer roller contacts the ground. Then, the rotation torque generated by the normal force pushes the vehicle toward the right side. This type of rotation torque is called restoring torque in this thesis. After that, the right-side outer roller starts to contact the ground again. As a result of these repeated processes, the small waveform is considered to be generated. In fact, as shown in Fig. 5.10, the period and amplitude of the small waveform become small as $\dot{\theta}$ becomes large. This can be explained by the alternating roller contact occurring at smaller intervals when the vehicle travels at a faster velocity.

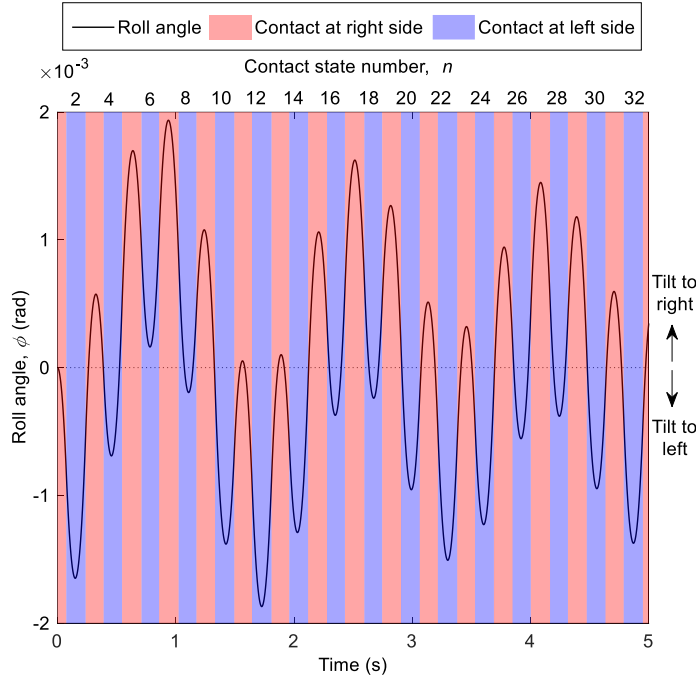


Fig. 5.11 Variation of contact state and roll angle at $\dot{\theta} = 5$ rad/s

Next, the behavior of the large waveform is discussed. Here, the contact duration of the outer rollers is investigated. The contact duration means the period from the moment when the outer roller starts to contact the ground to the moment it leaves the ground, which corresponds to the period of one red or blue band shown in Fig. 5.11. The contact state number n is given at the top of Fig. 5.11. The right-side outer roller contacts the ground when n is odd, while the left-side outer roller contacts the ground when n is even. The contact duration of the front wheel at $\dot{\theta} = 5$ rad/s is shown in Fig. 5.12, where the abscissa axis shows the contact state number n . The contact duration of the n -th contact is set as t_{rn} or t_{ln} ($n = 1, 2, 3, \dots$). Here, t_{rn} is the contact duration of the right-side outer roller, while t_{ln} is that of the left-side roller. When the initial contact ($n = 1$) is ignored, the variation of the contact duration of the right-side and left-side outer rollers has the appearance of two phase-shifted sine waves. Comparison of Figs. 5.11 and 5.12 shows that when the vehicle tilts to the left side, as shown by the black solid curve in the negative region in Fig. 5.11, the contact duration of the right-side outer rollers is high and that of the left side is low, as shown in Fig. 5.12. The opposite situation occurs when the vehicle leans to the right side.

The difference in the contact duration summation at $\dot{\theta} = 5$ rad/s is investigated, which is shown as a histogram in Fig. 5.13. The difference in the contact duration summation is defined as $t_{dm} = \sum_{n \in \text{odd}} t_{rn} - \sum_{n \in \text{even}} t_{ln}$ ($m = 1, 2, 3, \dots$), where the index m is the number of times the right-side and left-side outer rollers are switched. For instance, $t_{d1} = t_{r1}$, $t_{d2} = t_{r1} - t_{l2}$, and $t_{d3} = t_{r1} + t_{r3} - t_{l2}$. The positive value of t_{dm} means the contact duration of the right-side outer roller is longer in total, while the negative value of t_{dm} means the contact duration of the left-side outer roller is longer in total. To show the variation of t_{dm} clearly, the moving average of t_{dm} is defined as $t_{sm} =$

$(t_{d(m-1)} + t_{dm})/2$, which is shown as a curve in Fig. 5.13. By combining the results of Fig. 5.13 with the large waveforms of the roll angle shown in Fig. 5.11, it shows that the vehicle tends to lean to the right side when the contact duration of the left-side outer roller is longer, i.e., when $t_{sm} < 0$, while the vehicle tends to lean to the left side when the contact duration of the right side is longer, i.e., when $t_{sm} > 0$. This might be because the change in the angular momentum, or the angular impulse, is given by the product of the contact duration of the outer roller and the restoring torque generated by the normal force. When the right-side outer rollers contact the ground, the restoring torque acts to make the vehicle lean to the left side. In contrast, it is opposite when the left-side outer rollers contact the ground. Then, when the contact duration is longer, the resultant angular impulse becomes larger. Thus, the difference in the angular impulse from the right-side and left-side outer rollers generates the large waveform.

Additionally, as shown in Fig. 5.10, the amplitude of the large waveform becomes small as the rotational velocity increases for $\dot{\theta} = 5$ rad/s, 10 rad/s, and 20 rad/s. This might be because the contact duration becomes short when the rotational velocity becomes large, which weakens the angular impulse.

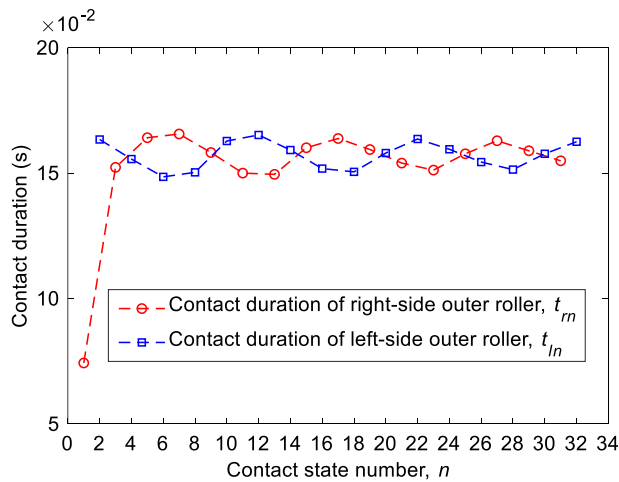


Fig. 5.12 Variation of contact duration of each outer roller at $\dot{\theta} = 5$ rad/s

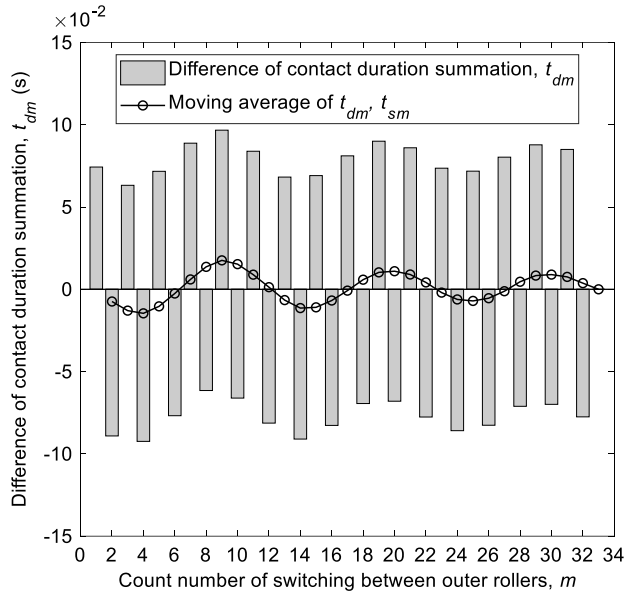


Fig. 5.13 Difference of contact duration summation at $\dot{\theta} = 5$ rad/s

In contrast, the swing amplitude of the vehicle, namely, the amplitude of the large waveforms, increases at $\dot{\theta} = 40$ rad/s, and the vehicle falls over after 2.5 s at $\dot{\theta} = 80$ rad/s. The variation of the roll angle and the moving average of t_{dm} in these cases are shown in Fig. 5.14. Both graphs show that t_{sm} almost constantly decreases, which means that the contact duration of the left-side outer roller is always longer than that of the right-side roller. Normally, the contact duration of the right-side outer roller increases when the vehicle tilts to the right side. However, when the rotational velocity of the wheel is high, the state with no contact points becomes more likely at one side, which reduces the contact duration. For this reason, although the period when the vehicle tilts to the right side is longer than that when it tilts to the left side, as shown in Fig. 5.14, the contact duration summation of the left-side outer roller is longer than that of the right-side outer roller. Therefore, the larger angular impulse generated by the left-side outer roller makes the swing amplitude at the right side become large at $\dot{\theta} = 40$ rad/s, while it makes the vehicle fall to the right side finally at $\dot{\theta} = 80$ rad/s.

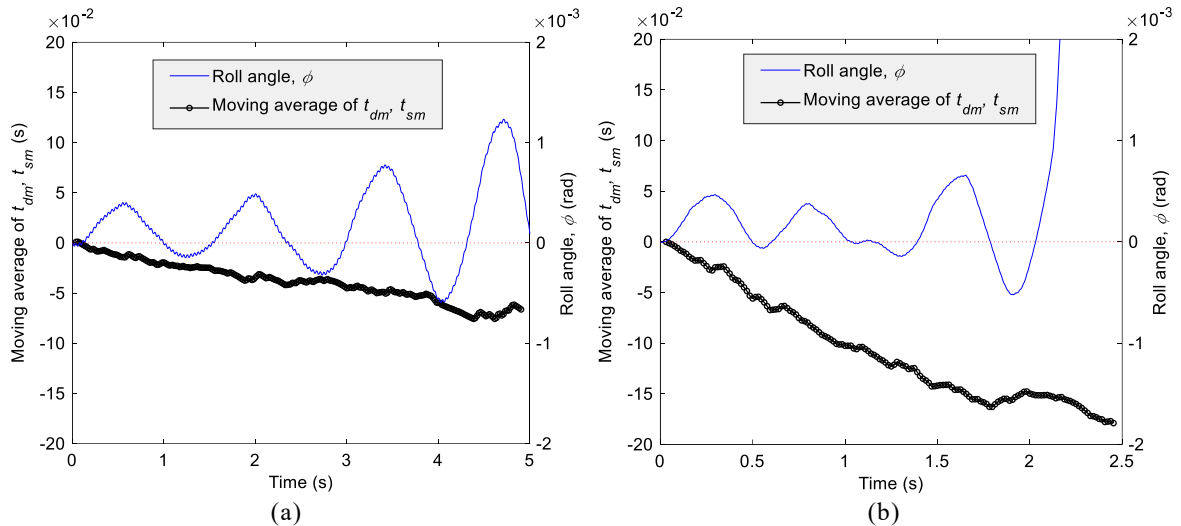


Fig. 5.14 Variation of contact duration summation and roll angle. (a) $\dot{\theta} = 40$ rad/s, (b) $\dot{\theta} = 80$ rad/s.

5.3.3 Effective Range of Traveling Stability

As explained in the previous section, the vehicle with two DAOWs travels while tilting to the right and left sides alternately according to the difference of the contact duration summation. The main factor is that the restoring torque generated by the normal force of the outer rollers makes the vehicle return to the right side when it leans to the left side, as shown in Fig. 5.15(a), or return to the left side when it leans to the right side. However, the rotation torque generated by the contacting outer roller can cause the vehicle to tilt too far and fall when the roll angle is too large, i.e., when the COG of the vehicle moves to the outside of the contact point, as shown in Fig. 5.15(b). Therefore, it is necessary to figure out the range of the roll angle for which the restoring torque is effective.

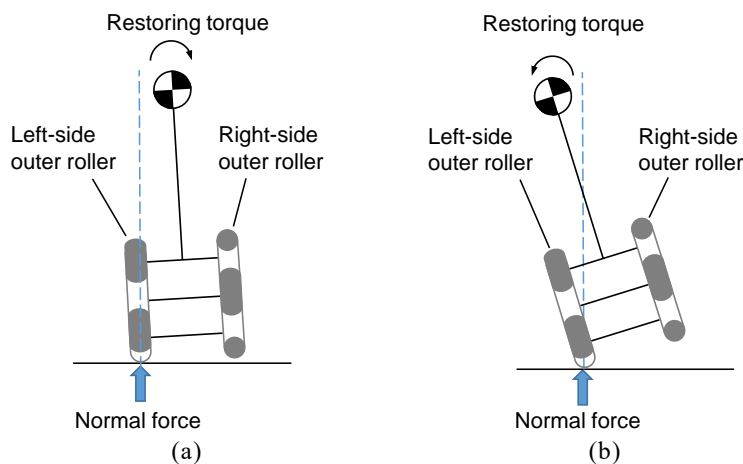


Fig. 5.15 Restoring torque generated by the normal force

Fig. 5.16 shows the variation of the average torque generated by the normal force in one rotation of the wheel when the roll angle is changed. The static situation is considered here, namely, $\dot{\phi} = 0$ and $\dot{p}_{ri} = \dot{p}_{li} = 0$ are assumed during wheel rotation. In addition, the normal force F_r or F_l is equivalent to half of the gravity of the vehicle under the state of one contact point, while F_r and F_l are equivalent to quarter of the gravity in the case of two contact points. The other parameters are determined by Eqs. (5.3) and (5.4). Several spring coefficients are considered here, while the damper coefficient is set to zero for simplicity. The calculation results for the spring coefficient $k = 5.0 \times 10^7$ N/m in Table 5.1 are shown as a thick solid red curve. The graph shows that the torque is negative for $k = 5.0 \times 10^7$ N/m when $0 \leq \phi \leq 0.024$ rad. At this time, the torque acts as a restoring torque to make the vehicle return to the horizontal position. This is also true for the positive torque when $-0.024 \leq \phi < 0$ rad. Actually, in Fig. 5.10, the roll angle variation in all cases of stable traveling remains within the range of $-0.024 \leq \phi \leq 0.024$ rad. However, the torque fails to keep the vehicle stable when $\phi < -0.024$ rad or $\phi > 0.024$ rad, which agrees with the supposition that the vehicle falls when the COG moves outside the contact point.

Next, the torque in one rotation when the spring coefficient is varied is discussed. Fig. 5.16 indicates that the variation in torque at $k = 5.0 \times 10^6$ N/m shows a tendency similar to that for $k = 5.0 \times 10^7$ N/m. In the cases of $k = 5.0 \times 10^5$ N/m and $k = 5.0 \times 10^4$ N/m, the torque works in a direction that makes the vehicle fall at any roll angle. This might be because the displacement of the outer roller is large when the spring coefficient is small, which leads to an increase in the duration of the state with two contact points, as shown in the right of Fig. 5.6(b), for each wheel. Therefore, a normal force is generated at both sides of the outer rollers, which eliminates the effect of the restoring torque.

When the vehicle stands in a horizontal position statically, to avoid falling down, it is advantageous that both the right- and left-side outer rollers contact the ground at the same time. However, this has a negative effect on the stability when the vehicle travels. This means that a vehicle with two DAOWs does not necessarily have an advantage even when both right- and left-side outer rollers contact the ground at the same time. Namely, contact at two points has different effects on stability when the vehicle travels and when the vehicle stands still.

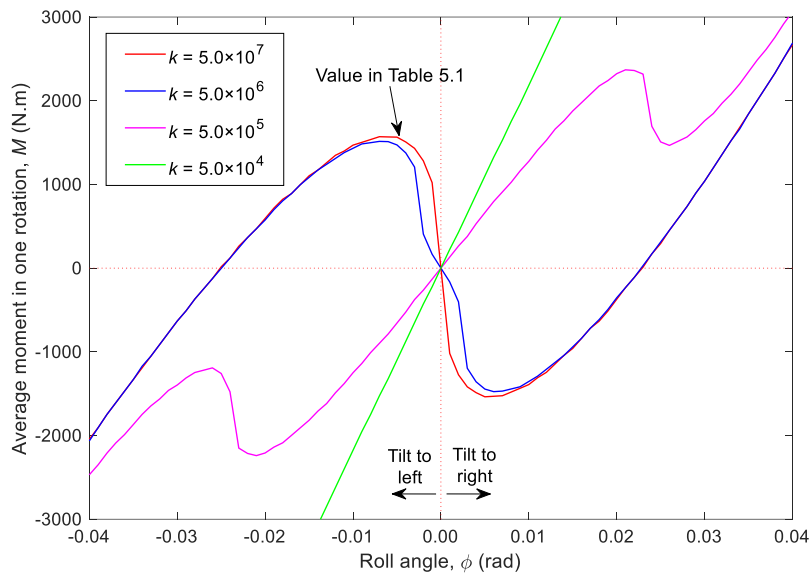


Fig. 5.16 Torque in one rotation for different roll angles and spring coefficients

5.3.4 Summary of Simulation Results

The traveling stability of the single-track vehicle with two DAOWs in the roll direction is discussed in the above sections. The vehicle can keep traveling without falling while swinging from side to side even without stability control. When the vehicle leans to one side, the rotation torque generated by the outer roller of that side makes the vehicle return to the opposite side. As a result, the vehicle acquires traveling stability by swinging from side to side. This is different from a single-track vehicle with conventional tired wheels because the conventional vehicle quickly falls down without stability control.

The variation of the roll angle contains small waveforms and large waveforms. The small waveforms are generated because of the switching of the contact point between the right- and left-side outer rollers. The large waveforms are thought to be the result of differences in the contact duration. When the vehicle tilts to one side, the contact duration of the outer roller on that side becomes long. The outer roller that contacts the ground for a longer time generates a larger angular impulse to make the vehicle tilt to the opposite side. The side with longer contact duration alternates, which is thought to be the reason for the large waveforms.

The vehicle can travel stably at low velocity but falls to the ground quickly when the rotational velocity of the wheel is high. This is because the wheel bounds into the air due to the impact of ground contact, which disrupts the balance of the restoring torque generated by the right- and left-side outer rollers. The vehicle can remain stable in a certain range of roll angles when the spring coefficient of the outer roller is sufficiently large. However, the vehicle fails to maintain stability when the roll angle is too large or the spring coefficient of the outer roller is small. When the roll

angle is too large, the COG of the vehicle moves outside the contact point and the torque from the contacting outer roller causes the vehicle to fall. A small spring coefficient of the outer roller weakens the restoring effect because it becomes easier for the outer rollers on both sides to contact the ground at the same time. Although two points having contact simultaneously contribute to stability when the vehicle is standing still, it has a negative effect on vehicle stability during traveling.

Finally, the possible ways to improve the traveling stability of the vehicle are discussed. First, a small viscoelasticity for the outer rollers may contribute to avoiding wheel bounce even when the traveling velocity is large, which would help to maintain the balance of the restoring torque of the right- and left-side outer rollers. Another approach would be to make the distance large between the outer rollers on the two sides. This is expected to be effective both in keeping the COG of the vehicle within the contact point and in preventing the outer rollers on both sides from contacting the ground at the same time.

5.4 Traveling Experiment

To validate the simulation results, a prototype vehicle equipped with two DAOWs was developed, and experiments were conducted.

5.4.1 Experimental Setup

Fig. 5.17 shows the developed prototype vehicle, whose size and mass parameters are basically the same as those in Table 5.1. Two DAOWs were installed along the centerline of the vehicle. Each DAOW had eight outer rollers made of polyether urethane rubber. Although the structure of the DAOW of the prototype was different from that of Fig. 5.1, the fundamental principle and function were the same. The front and rear wheels were driven separately, each by two motors, according to the kinematic constraints (see Appendix B). Note that both wheels were controlled to move only forward with the same phase and velocity in the experiment. The vehicle was equipped with batteries for a power supply. To measure the roll angle variation, a wireless gyro acceleration sensor (NGIMU, X-IO Technologies Ltd.) was fixed to an acrylic plate just above the center of the front DAOW, as shown in the figure. The sampling frequency of the gyro sensor was set to 50 Hz. The movement of the vehicle was controlled by using a three-axis joystick and program interface. Four auxiliary wheels were installed symmetrically at the corners of the vehicle to restrict the maximum roll angle of the vehicle to $\pm 4^\circ$. Two parallel rails were fixed on the ground for the auxiliary wheels to prevent the vehicle body from roll over until the vehicle reached the desired moving speed. The length of each rail was 2 m. The rails were used only during acceleration in the initial stage. The vehicle was commanded to continue to move 10 m after exiting the rail section. The structure of the control system hardware for the prototype vehicle is shown in Fig. 5.18 and Table 5.2.

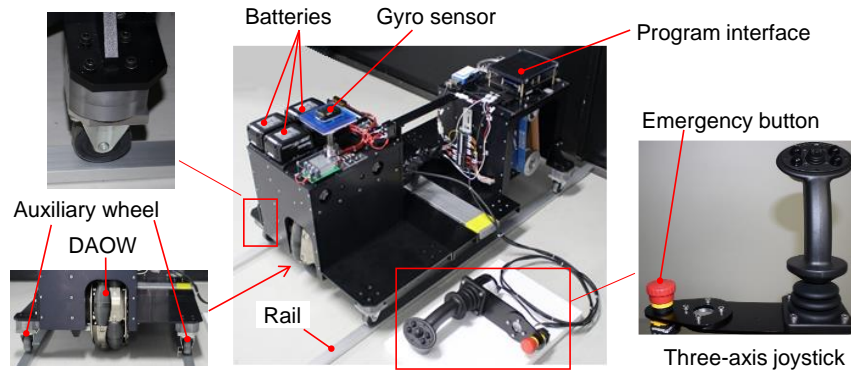


Fig. 5.17 Prototype vehicle with two DAOWs

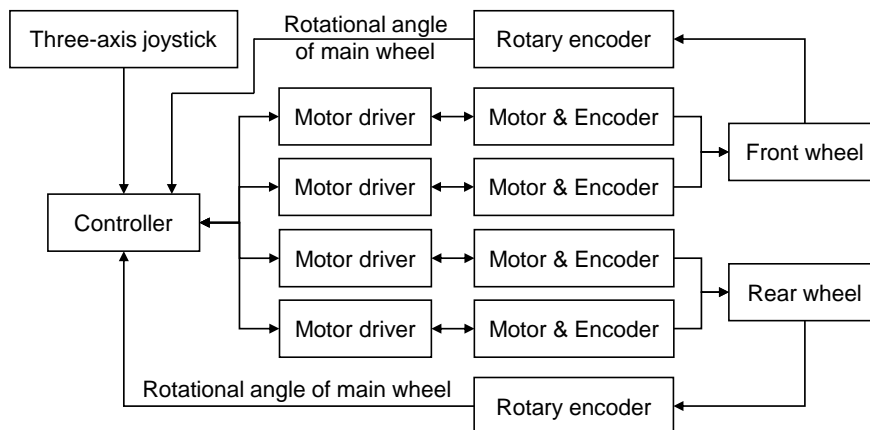


Fig. 5.18 Control system hardware for the experimental vehicle

Table 5.2 Components of control system

Name	Model	Quantity
Motor driver	Maxon EPOS4 Compact 50/15	4
Motor	Maxon RE50 (200 W)	4
Motor encoder	Maxon ILEDL 5540	4
Rotary encoder	Lika Electronic, SMRA-GG1-01-L1, MRA/130-110	2
Controller	Intel NUC 617KYK	1
Three-axis joystick	APEM Inc. HG-44M1S000-U-2655	1

5.4.2 Experimental Results

Experiments were conducted at vehicle speeds of $V_x = 1.0$ km/h, 1.2 km/h, 1.4 km/h, and 1.6 km/h. The measured variation of the roll angle is shown in Fig. 5.19, where a median filter with a size of 0.34 s was applied to remove noise from the data. The vertical axis in Fig. 5.19 indicates the roll angle of the vehicle, while the horizontal axis indicates the time during the vehicle traveling the 10-m path. The auxiliary wheels contact the ground when the roll angle is larger than 4° or

smaller than -4° , which is shown as a grey area in the figure. The dashed red rectangles in the figure indicate that the vehicle can keep balance by itself in some period without the support of the auxiliary wheels.

All results show that the vehicle swings frequently. When $V_x = 1.0$ km/h and $V_x = 1.2$ km/h, the vehicle leaned to the right or left side alternately, as shown in Figs. 5.19(a) and 5.19(b). These results suggest that the restoring torque from the right-side outer roller makes the vehicle tilt to the left side, and vice versa. In other words, it was verified that the restoring torque from the outer roller has the potential to make the vehicle return to the horizontal position as expected.

In contrast, the vehicle remained tilting to one side at most times when $V_x = 1.4$ km/h and 1.6 km/h, as seen from overall waveform shown in Figs. 5.19(c) and 5.19(d). This might partly reflect the simulation results that the vehicle falls to one side when the wheel has a high rotational velocity (e.g., in the case of $\dot{\theta} = 80$ rad/s in Fig. 5.10). The small vibration shown in the graphs is considered to be generated by switching between the right-side and left-side outer rollers. When the tilt angle is too large, however, the COG of the vehicle moves outside the contact point, and then the restoring torque from the outer rollers becomes a non-restoring torque that makes the vehicle fall to the ground, as shown in Fig. 5.15(b).

Comparing with Fig. 5.10 and 5.19, some differences were seen between the simulation and experimental results. For example, the range of the roll angle in the experiment tended to be larger than that in the simulation. Besides, the velocity at which the vehicle was no longer able to keep a balance in the simulation was higher than that in the experiment. These might be because the simulation adopts a simplified model as described below.

In Figs. 5.19(b), 5.19(c), and 5.19(d), although the swing of the vehicle is large, some situations where no auxiliary wheels contact the ground for more than 1.0 s are found, as indicated by the dashed red rectangles: 7.1–8.4 s, 13.7–15.0 s, and 36.3–37.6 s in Fig. 5.19(b); 23.3–24.4 s in Fig. 5.19(c); and 6.5–7.5 s in Fig. 5.19(d). In these situations, the roll angle stays within the range of $\pm 2.0^\circ$. A stable traveling situation is more likely to occur at $V_x = 1.2$ km/h than at other speeds. Although the roll angle range and the stable traveling speed are different from that in the simulation, the stable traveling phenomenon is observed also in the experiment. These results verify that a vehicle with two DAOWs can successfully maintain stability under the specific speed and range of the roll angle shown in the simulation results.

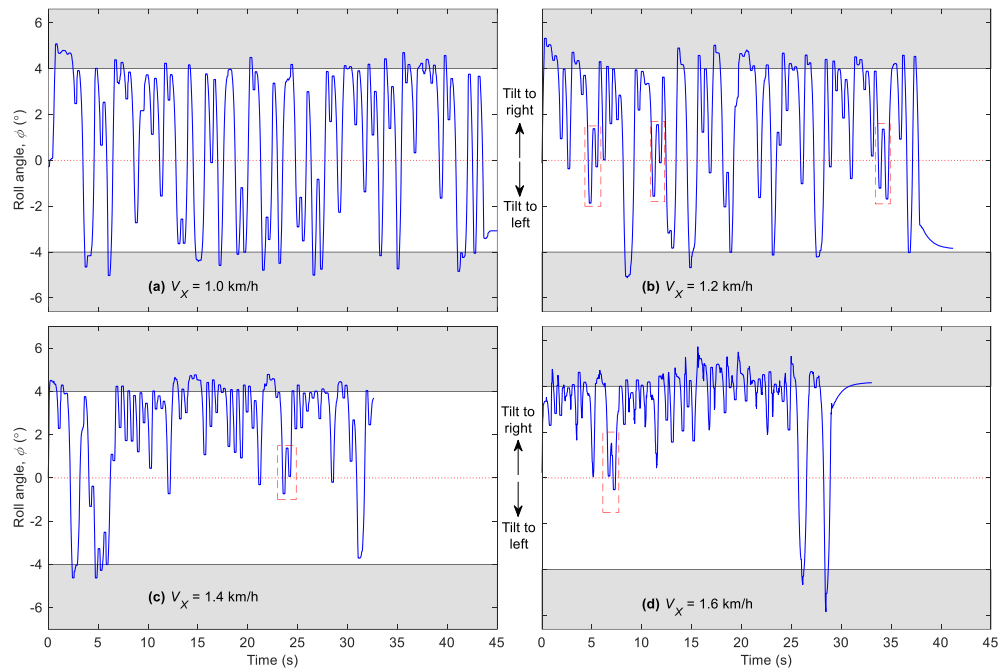


Fig. 5.19 Experimental results on measured roll angle of the prototype at different velocities

In order to verify the validity of the results, the frequency analysis is carried out through the Fourier transform. First, the calculation results with respect to the data of the whole period at each speed are shown in Fig. 5.20(a). The vibration takes the peak amplitude at $f_e = 1.17$ Hz for $V_x = 1.0$ km/h, $f_e = 1.43$ Hz for $V_x = 1.2$ km/h, $f_e = 1.66$ Hz for $V_x = 1.4$ km/h, and $f_e = 1.88$ Hz for $V_x = 1.6$ km/h. Next, the Fourier transform for the sampling data of the stable traveling periods at $V_x = 1.2$ km/h is performed. The transform results are shown in Fig. 5.20(b), which shows that the vibration takes the peak amplitude at the same frequency as in Fig. 5.20(a), $f_e = 1.43$ Hz.

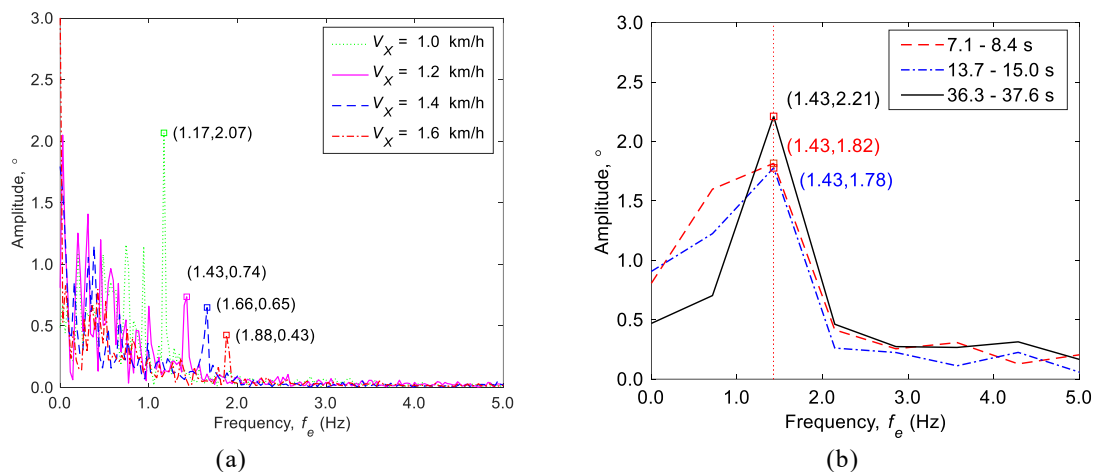


Fig. 5.20 Frequency analysis result of the roll angle variation measured in the experiment. (a) Whole period, (b) Stable traveling period at $v = 1.2$ km/h.

Here, the switching of the contacting outer rollers between the right and left sides is investigated. The switching frequency f_t of the outer rollers is calculated theoretically by

$$f_t = \frac{N}{2} \cdot \frac{1}{2\pi R} \cdot \frac{1000}{60^2} V_X = \frac{5NV_X}{72\pi R} . \quad (5.16)$$

Then, the calculation result of the theoretical switching frequency is compared with the frequency analysis result of the experimental data. As shown in Table 5.3, each peak frequency of the experimental result, whichever the result of the whole period at $V_X = 1.0$ km/h, 1.2 km/h, 1.4 km/h, and 1.6 km/h or the results of the stable traveling periods at $V_X = 1.2$ km/h, almost agrees with the theoretical switching frequency. This result means that the rolling motion of the vehicle is affected mainly by the switching of the outer rollers.

In the experiment, the prototype suffers various factors, such as the deformation of the vehicle or yawing, while the simulation uses a simplified and ideal model that focuses on the contact dynamics between the outer rollers and the ground. As a result, the variation of the roll angle and the stable traveling speed of the vehicle in the simulation are somewhat different from that of the experiment. However, even with this difference, the frequency analysis result almost agrees with the theoretical switching frequency, which shows that the contact dynamics in the switching of outer rollers is the major factor related to the traveling stability. Actually, the same stable traveling phenomenon occurred in both the simulation and experiment. That is, when the vehicle leans to the right or left side, the torque generated during the switching of the outer rollers tries to make the vehicle return to the normal position. When the vehicle travels stably, the direction of the torque switches at appropriate intervals to balance the vehicle. From the above, the experimental results are considered to support the simulation results.

Table 5.3 Comparison of frequency

Traveling speed, V_X	Theoretical switching frequency, f_t	Peak frequency of experimental result, f_e
1.0 km/h	1.18 Hz	1.17 Hz
1.2 km/h	1.41 Hz	1.43 Hz
1.4 km/h	1.65 Hz	1.66 Hz
1.6 km/h	1.89 Hz	1.88 Hz

5.5 Summary

Omnidirectional single-track vehicles have high maneuverability, but the rolling dynamic characteristics are rarely reported. With this in mind, this chapter chosen a single-track vehicle with

two DAOWs as an example. Its traveling stability by focusing on motion behavior in the roll direction was discussed based on simulations and experiments. The following results were obtained.

- The kinetic model of a single-track vehicle with two DAOWs was established considering that the number of contact points between the outer rollers of one wheel and the ground varied from zero to two during traveling due to the double-row outer roller structure.
- Simulations were conducted using the established kinetic model considering the contact dynamics between the outer rollers and ground. The simulation results showed that the vehicle could travel stably for more than 10 s without any balancing control under certain conditions. This stability was significantly different compared with single-track vehicles with conventional tired wheels, which have difficulty in traveling without falling over for such a long time in the absence of balancing control.
- As the vehicle traveled, the roll angle varied within a certain range, and it was composed of small and large waveforms. An analysis of the traveling stability mechanism suggested that the small waveforms of the roll angle were caused by ground contact alternating from outer rollers on one side to that on the other side of the wheel. The large waveforms occurred due to the balance of the angular impulse as a result of differences in the contact duration between the right-side and left-side outer rollers.
- A prototype of a vehicle equipped with two DAOWs was developed and used for experiments. The results showed that the vehicle could travel stably in some periods.

Chapter 6

Conclusions and Future Work

6.1 Conclusions

Wheeled mobile robots including locomotion vehicles and MPMs are widely used in human life and industry production. In order to obtain the feasible wheel compositions of vehicles (including wheel types, combinations, and layouts) and structures of MPMs, this thesis proposed a screw-theory-based synthesis method to obtain the possible wheel compositions and MPM structures. On the other hand, the feasible traveling strategy of omnidirectional-wheeled vehicle are investigated when it travels at high speed on an angled path. Additionally, the dynamic characteristics in roll direction are studied based on the subject of the single-track vehicle equipped with DAOWs. Based on these discussion and analysis, some methods and suggestions were proposed for the issue of wheeled mobile robots with respect to the kinematics and dynamics.

Chapter 2 proposed a screw-theory-based method to synthesize the feasible wheel types and combinations according to the requirement of mobility. It was based on the consideration that the wheel was seen as the combination of the revolute pairs and the prismatic pairs. Additionally, a kinematic modeling method was proposed based on the screw theory to establish the kinematic equation. An example of synthesizing an omnidirectional two-wheeled vehicle was performed based on the proposed method. The vehicles with respect to synthesis results were modeled and analyzed to verify validity of the proposed methods.

Based on the same consideration of the wheel as that in Chapter 2, Chapter 3 constructed a type synthesis method to obtain the possible six-DOF MPM structures. The type synthesis of the entire MPM was divided into those of the mobile base and connecting chain. Two solutions, applying singularity configuration and adding an additional chain, were revealed as ways to restrict undesired motions for the synthesis of the connecting chain. The mobile base was synthesized via the same type-synthesis method as introduced in Chapter 2. The method used to integrate the driving unit and the connecting chain was constructed based on whether the end pair of the connecting chain should be connected with the driving unit directly or driven by it through an actuating mechanism. Finally, 284 possible types of MPM structures were obtained and four examples of these MPMs with six DOFs were analyzed to verify the feasibility of the proposed method.

Chapter 4 focused on the traveling strategies of the omnidirectional-wheeled vehicle when they were required to travel on a specified path with one corner. The OWV was chosen as the research subject. Its kinetic model was established first based on the assumption of nonslip. The traveling

forms of OWV were proposed by referring to the timing of changing the orientation of the vehicle, for which the possible traveling patterns were discussed and set additionally. Simulations were conducted on the OWV to analyze the advantages of each pattern and compare the traveling strategies for various path conditions. Feasible traveling strategies were suggested. It showed that it is advantageous for OWV to change the orientation after turning the corner when the corner angle or the path width is small. When both of them become larger, the traveling strategy that changing orientation during turning the corner costs less time than the other forms. The traveling strategy that changing the orientation before turning the corner is advantageous when the path length after the corner is small. The same investigations were also conducted on the conventional-wheeled vehicle. Finally, the time cost was compared and discussed based on the above analysis when the path conditions were varied.

Chapter 5 chosen an omnidirectional single-track vehicle equipped with two DAOWs as the research subject and analyzed the effect of the double-row structure on the traveling stability in the rolling direction. A kinetic model considering the contact state between the outer rollers and ground was established first. Next, a simulation based on the contact model was conducted to elucidate the effect of the switching mechanism of the double-row structure. It showed that the vehicle could travel stably for more than 10s even without balance control. The roll angle varied as the composition of small and large waveforms. The small waveforms were caused by alternating contact of the outer rollers at two sides, while the large waveforms were considered to be generated because of the angular impulse. Finally, a prototype vehicle was developed and used for experiments, which confirmed that the switching of the outer rollers contributed to the traveling stability of vehicle in roll direction.

6.2 Future Work

The work referring to the following aspects should be explored in the future:

- With respect to the MPM, the kinematic analysis, stiffness analysis, and controller design should be conducted. Some novel MPM structures were obtained in Chapter 3, which were not analyzed and verified in detail. Therefore, the kinematic model is needed to be constructed to analyze the singularity, workspace, velocity characteristics, and so on. Although the stiffness of a certain MPM was proved to be higher than the conventional Stewart platform, the load capacity is also needed to be analyzed. Based on the analysis results, a prototype should be developed to verify the kinematic characteristics. A feedback controller should be designed by considering these errors, whose feasibility can be verified on the same prototype.

- Regarding the traveling strategy, a time-optimal controller will be designed and verified through experiments for the omnidirectional-wheeled robot based on the features of proposed traveling strategies in this thesis.
- With respect to the traveling stability of the single-track vehicle with two DAOWs, the effect of the design parameters of the DAOW should be investigated in more detail. According to the analysis results in Chapter 5, the effect of the double-row structure on stability resulted in the difference of angular impulse, which may be affected by the design parameters of the DAOW including the width, the radius, and the number of outer rollers. The prototype should be remodeled to conduct advanced experiments.

Appendix

Appendix A.

Equation (5.3) is calculated as follows: It is assumed that the vehicle is left-right and front-rear symmetry about the COG. When the right-sided outer roller of the front wheel contacts the ground, the position vector of the COG before tilting is calculated as shown in Fig. A1.

$$\overline{OA} = \overline{OQ} + \overline{QE} + \overline{ES} + \overline{BA} - \overline{BS} \quad (\text{A.1})$$

where point Q is the ground contact point of the right side of the front wheel, point S is the intersection point of the axle of the DAOW and the vertical line passing through point Q, point B is directly below the COG, and point E is the origin of the coordinate system of the outer roller. It is set that $|\overline{QS}| = R$ and $|\overline{BA}| = h_0$.

When the vehicle tilts around the roll and pitch directions, the rotation matrices around the X-axis and Y-axis in Fig. 5.4(a) are defined as $\mathbf{R}_X(\phi)$ and $\mathbf{R}_Y(\psi)$, respectively. The yawing effect is ignored in this chapter. Then, the position vector of the COG \overline{OA} can be written as follows:

$$\overline{OA} = \overline{OQ} + \overline{QE} + \mathbf{R}_X(\phi)\overline{ES} + \mathbf{R}_Y(\psi)\mathbf{R}_X(\phi)(\overline{BA} - \overline{BS}) \quad (\text{A.2})$$

$$\mathbf{R}_X(\phi) = \begin{pmatrix} 1 & 0 & 0 \\ 0 & \cos\phi & -\sin\phi \\ 0 & \sin\phi & \cos\phi \end{pmatrix}, \quad \mathbf{R}_Y(\psi) = \begin{pmatrix} \cos\psi & 0 & \sin\psi \\ 0 & 1 & 0 \\ -\sin\psi & 0 & \cos\psi \end{pmatrix} \quad (\text{A.3})$$

where $\overline{BA} = (0 \ 0 \ h_0)^T$, $\overline{BS} = (\rho/2 \ -d_w \ 0)^T$, $\overline{ES} = ((R - r_0)\sin\delta \ 0 \ (R - r_0)\cos\delta)^T$, $\overline{QE} = (-X_r \ 0 \ -Z_r + p_{r1})^T$, $\overline{QE} = (\rho/2 + R(\dot{\theta}t + \ddot{\theta}t^2/2), -d_w, 0)^T$, $X_r = X_Q - X_E$, $Z_r = Z_Q - Z_E$, X_Q and X_E are the X coordinate values of point Q and point E in the coordinate system Σ_o , respectively, and Z_Q and Z_E are the Z coordinate values of point Q and point E in the coordinate system Σ_o , respectively. Therefore, the displacement of the COG in Eq. (5.3) is given by $\overline{OA} = (C_{r1} \ K_{r1} \ H_{r1})$. The displacement of the COG is obtained in a similar way when the ground contact point varies.

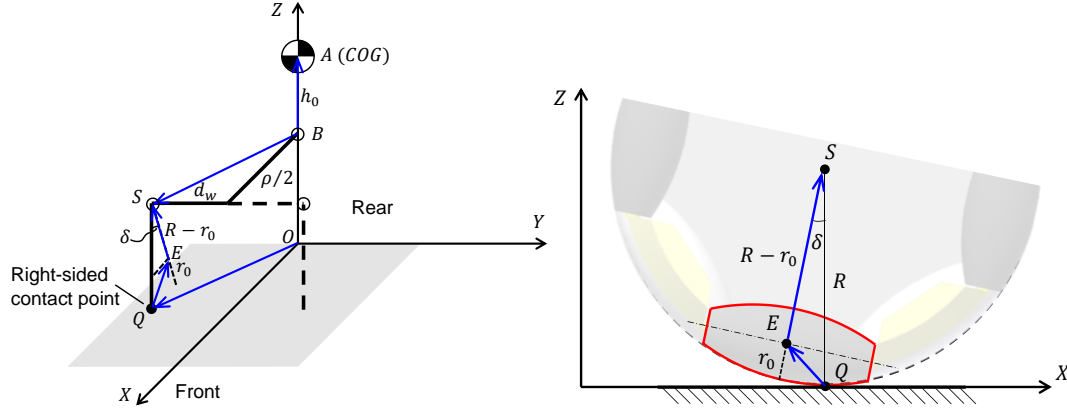


Fig. A1 Parameters for calculation of COG

Appendix B.

The relationship between the moving direction of the vehicle and the rotation velocities of the input shafts is explained. For the single DAOW, the moving velocities in X-axis and Y-axis directions can be calculated as follows:

$$\begin{pmatrix} V_{iX} \\ V_{iY} \end{pmatrix} = \begin{pmatrix} R/2 & R/2 \\ r/2k_d & -r/2k_d \end{pmatrix} \begin{pmatrix} \omega_{iu} \\ \omega_{ip} \end{pmatrix}, \quad i = 1, 2 \quad (\text{B.1})$$

where k_d is the reduction ratio between the differential gear mechanism and the outer rollers, r is the radius of the outer roller at the contact point, V_{iX} and V_{iY} are the moving velocities in the X-axis direction and Y-axis direction, respectively, and ω_{iu} and ω_{ip} are the rotation velocities of the input shaft 1 and the input shaft 2, respectively. The index $i = 1$ represents the front DAOW, while the index $i = 2$ represents the rear DAOW. Therefore, the traveling velocity vector of the vehicle is calculated as follows:

$$\begin{pmatrix} V_X \\ V_Y \\ \Omega \end{pmatrix} = \begin{pmatrix} \frac{1}{2} & 0 & \frac{1}{2} & 0 \\ 0 & \frac{1}{2} & 0 & \frac{1}{2} \\ 0 & -\frac{1}{\rho} & 0 & \frac{1}{\rho} \end{pmatrix} \begin{pmatrix} V_{1X} \\ V_{1Y} \\ V_{2X} \\ V_{2Y} \end{pmatrix} = \begin{pmatrix} R/4 & R/4 & R/4 & R/4 \\ r/4k_d & -r/4k_d & r/4k_d & -r/4k_d \\ -r/2k_d\rho & r/2k_d\rho & r/2k_d\rho & -r/2k_d\rho \end{pmatrix} \begin{pmatrix} \omega_{1u} \\ \omega_{1p} \\ \omega_{2u} \\ \omega_{2p} \end{pmatrix}. \quad (\text{B.2})$$

where V_X is the velocity in the forward direction, V_Y is the velocity in the left direction, Ω is the rotational velocity.

Reference

- [1] Siegwart, R., Nourbakhsh, I. R., & Scaramuzza, D., “Introduction to autonomous mobile robots”, MIT press, 2011.
- [2] Tadakuma, K., Tadakuma, R., Nagatani, K., Yoshida, K., Peters, S., Udengaard, M., Iagnemma, K., “Crawler vehicle with circular cross-section unit to realize sideways motion”, *IEEE/RSJ International Conference on Intelligent Robots and Systems*, pp. 2422-2428, 2008.
- [3] Kakogawa, A. & Ma, S., “Design of an underactuated parallelogram crawler module for an in-pipe robot”, *2013 IEEE International Conference on Robotics and Biomimetics (ROBIO)*, pp. 1324-1329, 2013.
- [4] Sokolov, M., Afanasyev, I., Lavrenov, R., Sagitov, A., Sabirova, L., & Magid, E., “Modelling a crawler-type UGV for urban search and rescue in Gazebo environment”, *Artificial Life and Robotics (ICAROB 2017)*, pp. 360-362, 2017.
- [5] Takemori, T., Tanaka M., & Matsuno, F., “Gait Design for a Snake Robot by Connecting Curve Segments and Experimental Demonstration”, *IEEE Transactions on Robotics*, vol. 34, no. 5, pp. 1384-1391, 2018.
- [6] Yim, J. K., Singh, B. R. P., Wang, E. K., Featherstone, R., & Fearing, R. S., “Precision robotic leaping and landing using stance-phase balance”, *IEEE Robotics and Automation Letters*, vol. 5, no. 2, pp. 3422-3429, 2020.
- [7] Yim, J. K., & Fearing, R. S., “Precision Jumping Limits from Flight-phase Control in Salto-1P”, *IEEE/RSJ International Conference on Intelligent Robots and Systems (IROS)*, pp. 2229-2236, 2018.
- [8] Morimoto, J. & Atkeson, C. G., “Learning Biped Locomotion”, *IEEE Robotics & Automation Magazine*, vol. 14, no. 2, pp. 41-51, 2007.
- [9] Chevallereau, C., Wenger, P., Aoustin, Y., Mercier, F., Delanoue, N., & Lucidarme, P., “Leg design for biped locomotion with mono-articular and bi-articular linear actuation”, *Mechanism and Machine Theory*, 156, 104138, 2021.
- [10] Valsecchi, G., Grandia, R., Hutter, M., “Quadrupedal Locomotion on Uneven Terrain With Sensorized Feet”, *IEEE Robotics and Automation Letters*, vol. 5, no. 2, pp. 1548-1555, 2020.
- [11] Lee, J., Hwangbo, J., Wellhausen, L., Koltun, V., & Hutter, M., “Learning quadrupedal locomotion over challenging terrain”, *Science Robotics*, vol. 5, no.47, 2020.
- [12] Zhong, G., Chen, L., Jiao, Z., Li, J., & Deng, H., “Locomotion Control and Gait Planning of a Novel Hexapod Robot Using Biomimetic Neurons”, *IEEE Transactions on Control Systems Technology*, vol. 26, no. 2, pp. 624-636, 2018.
- [13] Zhong, B., Zhang, S., Xu, M., Zhou, Y., Fang, T., & Li, W., “On a CPG-Based Hexapod Robot: AmphiHex-II With Variable Stiffness Legs”, *IEEE/ASME Transactions on Mechatronics*, vol. 23, no. 2, pp. 542-551, 2018.
- [14] Shojaei, K., Shahri, A. M., Tarakameh, A., & Tabibian, B., “Adaptive trajectory tracking control of a differential drive wheeled mobile robot”, *Robotica*, vol. 29, no. 3, pp. 391-402, 2011.
- [15] Ji, M., Zhang, Z., Biswas, G., & Sarkar, N., “Hybrid fault adaptive control of a wheeled mobile robot”, *IEEE/ASME Transactions on Mechatronics*, vol. 8, no. 2, pp. 226-233, 2003.
- [16] Kanayama, Y., Kimura, Y., Miyazaki, F., & Noguchi, T., “A stable tracking control method for

- an autonomous mobile robot”, *Proceedings IEEE International Conference on Robotics and Automation*, vol.1, pp. 384-389, 1990.
- [17] Saha, S. K., Angeles, J., & Darcovich, J., “The design of kinematically isotropic rolling robots with omnidirectional wheels”, *Mechanism and Machine Theory*, vol. 30, no.8, pp. 1127-1137, 1995.
- [18] Joshi, V. A., Banavar, R. N., & Hippalgaonkar, R., “Design and analysis of a spherical mobile robot”, *Mechanism and Machine Theory*, vol. 45, no. 2, pp. 130-136, 2010.
- [19] Conceição, A. G. S., Dórea, C. E., Martinez, L., & de Pieri, E. R. “Design and implementation of model-predictive control with friction compensation on an omnidirectional mobile robot”, *IEEE/ASME Trans. Mechatronics*, vol. 19, no. 2, pp. 467-476, 2013.
- [20] Grimminger, F., Meduri, A., Khadiv, M., Viereck, J., Wüthrich, M., Naveau, M., ... & Righetti, L., “An Open Torque-Controlled Modular Robot Architecture for Legged Locomotion Research”, *IEEE Robotics and Automation Letters*, vol. 5, no. 2, pp. 3650-3657, 2020.
- [21] Orozco-Magdaleno, E. C., Gómez-Bravo, F., Castillo-Castañeda, E., & Carbone, G., “Evaluation of Locomotion Performances for a Mecanum-Wheeled Hybrid Hexapod Robot”, *IEEE/ASME Transactions on Mechatronics*, vol. 26, no. 3, pp. 1657-1667, 2021.
- [22] Smith, J. A., Sharf, I., & Trentini, M., “PAW: a hybrid wheeled-leg robot”, *Proceedings 2006 IEEE International Conference on Robotics and Automation*, pp. 4043-4048, 2006.
- [23] Bruzzone, L. and Quaglia, G., “Review article: locomotion systems for ground mobile robots in unstructured environments”, *Mechanical Science*, vol. 3, pp. 49–62, 2012.
- [24] Yun, X. & Yamamoto, Y., “Internal dynamics of a wheeled mobile robot”, *Proceedings of 1993 IEEE/RSJ International Conference on Intelligent Robots and Systems (IROS 1993)*, vol.2, pp. 1288-1294, 1993.
- [25] Ishigami, G., Iagnemma, K., Overholt, J., & Hudas, G., “Design, development, and mobility evaluation of an omnidirectional mobile robot for rough terrain”, *Journal of Field Robotics*, vol. 32, no. 6, pp. 880-896, 2015.
- [26] Chung, W., Moon, C. B., Jung, C., & Jin, J., “Design of the dual offset active caster wheel for holonomic omni-directional mobile robots”, *International Journal of Advanced Robotic Systems*, vol. 7, no.4, 2010.
- [27] Loh, W. K., Low, K. H., & Leow, Y. P., “Mechatronics design and kinematic modelling of a singularityless omni-directional wheeled mobile robot”, In *IEEE International Conference on Robotics and Automation*, vol. 3, pp. 3237-3242, 2003.
- [28] Zobova, A. A., & Tatarinov, Y. V., “The dynamics of an omni-mobile vehicle”, *Journal of Applied Mathematics and Mechanics*, vol. 73, no. 1, pp. 8-15, 2009.
- [29] Gferrer, A., “Geometry and kinematics of the Mecanum wheel”, *Computer Aided Geometric Design*, vol. 25, no. 9, 784-791, 2008.
- [30] Li, Y., Dai, S., Zheng, Y., Tian, F., & Yan, X., “Modeling and kinematics simulation of a Mecanum wheel platform in RecurDyn”, *Journal of Robotics*, vol. 2018, 2018.
- [31] Chen, W. H., Chen, C. P., Tsai, J. S., Yang, J., Lin, P. C., “Design and implementation of a ball-driven omnidirectional spherical robot”, *Mechanism and Machine Theory*, vol.68, pp. 35-48, 2013.
- [32] Weiss, A., Langlois, R. G., Hayes, M. J. D., “The effects of dual row omnidirectional wheels on the kinematics of the Atlas spherical motion platform”, *Mechanism and Machine Theory*, vol. 40, no. 2, pp.349-358, 2009.

- [33] Saha, S. K., & Angeles, J., “Kinematics and dynamics of a three-wheeled 2-DOF AGV”, *Proceedings 1989 International Conference on Robotics and Automation*, vol. 3, pp. 1572-1577, 1989.
- [34] Cardarelli, E., Digani, V., Sabattini, L., Secchi, C., & Fantuzzi, C., “Cooperative Cloud Robotics Architecture for the Coordination of Multi-AGV Systems in Industrial Warehouses,” *Mechatronics*, vol. 45, pp. 1–13, 2017.
- [35] Debenest, P., & Guarnieri, M., “Expliner - From prototype towards a practical robot for inspection of high-voltage lines”, *2010 1st International Conference on Applied Robotics for the Power Industry*, pp. 1-6, 2010.
- [36] Jiang, L., Wang, S., Xie, Y., Meng, J., Zheng, S., Zhang, X., & Wu, H., “Anti-disturbance direct yaw moment control of a four-wheeled autonomous mobile robot”, *IEEE Access*, vol. 8, pp. 174654-174666, 2020.
- [37] Li, Y., Xu, Q., & Liu, Y., “Novel design and modeling of a mobile parallel manipulator”, *Proceedings 2006 IEEE International Conference on Robotics and Automation*, pp. 1135-1140, 2006.
- [38] Horin, P. B., Djerassi, S., Shoham, M., & Horin, R. B., Dynamics of a six degrees-of-freedom parallel robot actuated by three two-wheel carts, *Multibody System Dynamics*, vol. 16, no. 2, pp. 105-121, 2006.
- [39] Mukai, T., Hirano, S., Nakashima, H., Kato, Y., Sakaida, Y., Guo, S., & Hosoe, S., “Development of a nursing-care assistant robot RIBA that can lift a human in its arms”, *IEEE/RSJ International Conference on Intelligent Robots and Systems*, pp. 5996-6001, 2010.
- [40] Chong, Z., Xie, F., Liu, X. J., Wang, J., & Niu, H., “Design of the parallel mechanism for a hybrid mobile robot in wind turbine blades polishing”, *Robotics and Computer-Integrated Manufacturing*, vol. 61, 101857, 2020.
- [41] Silwal, A., Davidson, J. R., Karkee, M., Mo, C., Zhang, Q., & Lewis, K., “Design, integration, and field evaluation of a robotic apple harvester”, *Journal of Field Robotics*, vol. 34, no. 6, pp. 1140-1159, 2017.
- [42] Yamamoto, T., Terada, K., Ochiai, A., Saito, F., Asahara, Y., & Murase, K., “Development of the research platform of a domestic mobile manipulator utilized for international competition and field test”, *IEEE/RSJ International Conference on Intelligent Robots and Systems (IROS)*, pp. 7675-7682, 2018.
- [43] Kelly, A., & Seegmiller, N. “A vector algebra formulation of mobile robot velocity kinematics”, *Field and Service Robotics*, pp. 613-627, 2014.
- [44] Kim, D. S., Kwon, W. H., & Park, H. S., “Geometric kinematics and applications of a mobile robot”, *International Journal of Control, Automation, and Systems*, vol. 1, no. 3, pp. 376-384, 2003.
- [45] Muir, P. F., & Neuman, C. P., “Kinematic modeling of wheeled mobile robots”, *Journal of robotic systems*, vol. 4, no. 2, pp. 281-340, 1987.
- [46] Chakraborty, N., & Ghosal, A., “Kinematics of wheeled mobile robots on uneven terrain”, *Mechanism and machine theory*, vol. 39, no. 12, pp. 1273-1287, 2004.
- [47] Chang, Y., Tan, D., Wang, H., & Ma, S., “Kinematics Analysis of a Six-Wheeled Mobile Robot”, *IEEE/RSJ International Conference on Intelligent Robots and Systems*, pp. 4169-4174, 2006.
- [48] Campion, G. Bastin, G., & Dandrea-Novel, B., “Structural properties and classification of kinematic and dynamic models of wheeled mobile robots”, *IEEE Transactions on Robotics and*

- Automation*, vol. 12, no. 1, pp. 47-62, 1996.
- [49] Gracia, L., & Tornero, J., "Kinematic modeling and singularity of wheeled mobile robots. *Advanced Robotics*, vol. 21, no. 7, pp. 793-816, 2007.
- [50] Kim, S., & Kim, H., "Isotropy analysis of caster wheeled omnidirectional mobile robot", *IEEE International Conference on Robotics and Automation*, vol.3, pp. 3093-3098, 2004.
- [51] Chung, Y., Park, C., & Harashima, F., "A position control differential drive wheeled mobile robot", *IEEE Transactions on Industrial Electronics*, vol. 48, no. 4, pp. 853-863, 2001.
- [52] Muir, P. F., & Neuman, C. P., "Kinematic modeling for feedback control of an omnidirectional wheeled mobile robot", *Autonomous robot vehicles*, pp. 25-31, 1990.
- [53] Angeles J., "On the Numerical Solution of the Inverse Kinematic Problem", *The International Journal of Robotics Research*. vol. 4, no. 2, pp. 21-37, 1985.
- [54] Xiao, L., Zhang, Y., "Solving time-varying inverse kinematics problem of wheeled mobile manipulators using Zhang neural network with exponential convergence", *Nonlinear Dynamics*, vol. 76, pp. 1543-1559, 2014.
- [55] Hu, Y., Zhang, J., Wan, Z., & Lin, J., "Design and analysis of a 6-DOF mobile parallel robot with 3 limbs", *Journal of mechanical science and technology*, vol. 25, no. 12, pp. 3215-3222, 2011.
- [56] Tsai, L. W., "The Jacobian analysis of a parallel manipulator using reciprocal screws", *Advances in Robot Kinematics: Analysis and Control*, pp. 327-336, 1998.
- [57] Merlet, J. P., "Jacobian, manipulability, condition number, and accuracy of parallel robots", *ASME Journal of Mechanical Design*, vol. 128, no. 1, 2006.
- [58] Huang, Z., & Li, Q. C., "Type synthesis of symmetrical lower-mobility parallel mechanisms using the constraint-synthesis method", *The International Journal of Robotics Research*, vol. 22, no. 1, pp. 59-79, 2003.
- [59] Kong, X., & Gosselin, C. M., "Type synthesis of 4-DOF SP-equivalent parallel manipulators: A virtual chain approach", *Mechanism and machine theory*, vol. 41, no. 11, pp. 1306-1319, 2006.
- [60] Kim, S., & Kwon, S., "Dynamic modeling of a two-wheeled inverted pendulum balancing mobile robot", *International Journal of Control, Automation and Systems*, vol. 13, no. 4, pp. 926-933, 2015.
- [61] Chakraborty, N., & Ghosal, A., "Dynamic modeling and simulation of a wheeled mobile robot for traversing uneven terrain without slip", *ASME Journal of Mechanical Design*, vol. 127, no. 5, 2005.
- [62] Chung, J. H., Yi, B. J., Kim, W. K., & Lee, H., "The dynamic modeling and analysis for an omnidirectional mobile robot with three caster wheels", *IEEE International Conference on Robotics and Automation*, pp. 521-527, vol.1, 2003.
- [63] Tian, Y., Sidek N., & Sarkar, N., "Modeling and control of a nonholonomic Wheeled Mobile Robot with wheel slip dynamics", *IEEE Symposium on Computational Intelligence in Control and Automation*, pp. 7-14, 2009.
- [64] Wang, G., Liu, X., Zhao, Y. et al., "Neural Network-Based Adaptive Motion Control for a Mobile Robot with Unknown Longitudinal Slipping", *Chinese Journal of Mechanical Engineering*, vol. 32, no. 61, 2019.
- [65] Wu, W., Chen, H., & Woo, P. Y., "Time optimal path planning for a wheeled mobile robot", *Journal of Robotic Systems*, vol. 17, no. 11, pp. 585-591, 2000.

- [66] Borenstein, J., & Koren, Y., “Real-time obstacle avoidance for fast mobile robots”, *IEEE Transactions on systems, Man, and Cybernetics*, vol. 19, no. 5, pp. 1179-1187, 1989.
- [67] Kim, J., “Trajectory generation of a two-wheeled mobile robot in an uncertain environment. *IEEE Transactions on Industrial Electronics*, vol. 67, no. 7, pp. 5586-5594, 2019.
- [68] Liu, S., & Sun, D., “Minimizing energy consumption of wheeled mobile robots via optimal motion planning”, *IEEE/ASME Transactions on Mechatronics*, vol. 19, no. 2, pp. 401-411, 2013.
- [69] Zafar, M. N., & Mohanta, J. C. “Methodology for path planning and optimization of mobile robots: A review”, *Procedia computer science*, vol. 133, pp. 141-152, 2018.
- [70] Tzafestas, S. G., “Mobile robot control and navigation: A global overview”, *Journal of Intelligent & Robotic Systems*, vol. 91, no. 1, pp. 35-58, 2018.
- [71] Gao, X., Li, J., Fan, L., Zhou, Q., Yin, K., et al., & Wang, Z., “Review of wheeled mobile robots’ navigation problems and application prospects in agriculture”, *IEEE Access*, vol. 6, pp. 49248-49268, 2018.
- [72] Jin, H., Wang, T., Yu, F., Zhu, Y., Zhao, J., & Lee, J., “Unicycle robot stabilized by the effect of gyroscopic precession and its control realization based on centrifugal force compensation”, *IEEE/ASME Transactions on Mechatronics*, vol. 21, no. 6, pp. 2737-2745, 2016.
- [73] Chen, C. K., Chu, T. D., & Zhang, X. D., “Modeling and control of an active stabilizing assistant system for a bicycle”, *Sensors*, vol. 19, no. 2, 248, 2019.
- [74] Yi, J., Song, D., Levandowski, A., & Jayasuriya, S., “Trajectory tracking and balance stabilization control of autonomous motorcycles”, *Proceedings 2006 IEEE International Conference on Robotics and Automation*, pp. 2583-2589, 2006.
- [75] Meng X., Gao F., Wu S., et al., “Type synthesis of parallel robotic mechanisms: Framework and brief review”, *Mechanism and Machine Theory*, vol. 78, pp. 177-186, 2014.
- [76] Ye, W., Li, Q., “Type Synthesis of Lower Mobility Parallel Mechanisms: A Review”, *Chinese Journal of Mechanical Engineering*, vol. 32, no. 38, 2019.
- [77] Fang, Y., & Tsai, L. W., “Structure synthesis of a class of 3-DOF rotational parallel manipulators”, *IEEE transactions on robotics and automation*, vol. 20, no. 1, pp. 117-121, 2004.
- [78] Gao, F., Yang, J., & Ge, Q. J., “Type synthesis of parallel mechanisms having the second class GF sets and two dimensional rotations”, *Journal of Mechanisms and Robotics*, vol. 3, no.1, pp.011003, 2011.
- [79] Hunt K., “Kinematic Geometry of Mechanisms”, Cambridge, U.K.: Oxford Univ. Press, 1978.
- [80] Komori, M., Matsuda, K., Terakawa, T., Takeoka, F., Nishihara, H., & Ohashi, H., Active omni wheel capable of active motion in arbitrary direction and omnidirectional vehicle, *Journal of Advanced Mechanical Design, Systems, and Manufacturing*, vol. 10, no. 6, JAMDSM0086-JAMDSM0086, 2016.
- [81] Zhao, J., Li, B., Yang, X., & Yu, H., “Geometrical method to determine the reciprocal screws and applications to parallel manipulators”, *Robotica*, vol. 27, no. 6, 929, 2009.
- [82] Terakawa, T., Komori, M., Yamaguchi, Y., & Nishida, Y., “Active omni wheel possessing seamless periphery and omnidirectional vehicle using it”, *Precision Engineering*, vol. 56, pp. 466-475, 2019.
- [83] Komori, M., & Matsuda, K., “Velocity characteristics of active omni wheel considering transmitting mechanism”, *In European Conference on Mechanism Science (Germany)*, pp. 109-116, 2018.
- [84] Tahmasebi, F., & Tsai, L. W., “On the stiffness of a novel six - degree - freedom parallel

- minimanipulator”, *Journal of Robotic Systems*, vol. 12, no. 12, pp. 845-856, 1995.
- [85] Jin, Y., Chen, I. M., & Yang, G., “Kinematic design of a family of 6-DOF partially decoupled parallel manipulators”, *Mechanism and Machine Theory*, vol. 44, no. 5, pp. 912-922, 2009.
- [86] Li, Q., Huang, Z., & Hervé, J. M., “Type synthesis of 3R2T 5-DOF parallel mechanisms using the Lie group of displacements”, *IEEE transactions on robotics and automation*, vol. 20, no. 2, pp. 173-180, 2004.
- [87] Wu, G., & Bai, S., “Design and kinematic analysis of a 3-RRR spherical parallel manipulator reconfigured with four-bar linkages”, *Robotics and Computer-Integrated Manufacturing*, vol. 56, pp. 55-65, 2019.
- [88] Abe, M., “Automotive vehicle dynamics theory and applications”, second edition, Tokyo Denki University Press (in Japanese), 2012.
- [89] Nagai, M., Yamanaka, S., & Hirano, Y., “Integrated control of active rear wheel steering and yaw moment control using braking forces”, *Transactions of the Japan Society of Mechanical Engineers C*, 1998, (in Japanese).
- [90] Baslamisli, S. C., Polat, I., & Kose, I. E., “Gain scheduled active steering control based on a parametric bicycle model”, *2007 IEEE Intelligent Vehicles Symposium*, pp. 1168-1173, 2007.
- [91] Tanaka, Y., & Murakami, T., “Self sustaining bicycle robot with steering controller”, *The 8th IEEE International Workshop on Advanced Motion Control*, pp. 193-197, 2004.
- [92] Yavin, Y., “Stabilization and control of the motion of an autonomous bicycle by using a rotor for the tilting moment”, *Computer methods in applied mechanics and engineering*, vol. 178, no. 3-4, pp. 233-243, 1999.
- [93] Omata, N., Suga, T., Furusawa, H., Urabe, S., Kondo, T., & Ni, Q. Q., “Viscoelasticity evaluation of rubber by surface reflection of supersonic wave”, *Ultrasonics*, vol. 44, pp. 211-215, 2006.
- [94] Takahashi, T., Hayashi, N., & Hayashi, S., “Structure and properties of shape-memory polyurethane block copolymers”, *Journal of Applied Polymer Science*, vol. 60, no. 7, 1061-1069, 1996.

List of Publications

Chapter 2 consists of:

Siyong Long, Tatsuro Terakawa, Masaharu Komori, Kippe Matsuda, “Kinematic Characteristics Analysis of Omnidirectional Vehicle Equipped with Active Omni wheels Based on Screw Theory”, *The Japan Society of Mechanical Engineers MDT2021*, 2021.12.6.

Chapter 3 consists of:

Siyong Long, Tatsuro Terakawa, Masaharu Komori, “Type synthesis of 6-DOF mobile parallel link mechanisms based on screw theory”, *Journal of Advanced Mechanical Design, Systems, and Manufacturing*, Vol. 16, (2022), No. 1, pp. JAMDSM0005~JAMDSM0005. < DOI: 10.1299/jamdsm.2022jamdsm0005>

Chapter 4 consists of:

Siyong Long, Tatsuro Terakawa, Masaharu Komori, Takumi Ougino, “Analysis of Traveling Strategies for Driving Omni-Wheeled Vehicle Around a Corner”, *IEEE Access*, Vol. 8, (2020), pp. 104841-104856. < DOI: 10.1109/ACCESS.2020.2999344>

Siyong Long, Tatsuro Terakawa, Masaharu Komori, Takumi Ougino, “Comparison of Motion Strategies between Vehicle with Conventional Wheels and Omni Wheels”, *Proceedings of the SICE Annual Conference 2021*, 2021.9.9, pp. 839-844. Copyright © The Society of Instrument and Control Engineers (SICE) rights reserved.

Chapter 5 consists of:

Siyong Long, Tatsuro Terakawa, Masaharu Komori, Yugo Nishida, Takumi Ougino, Yusuke Hattori, “Effect of double-row active omni wheel on stability of single-track vehicle in roll direction”, *Mechanism and Machine theory*, Vol. 163, (2021), 104374. <DOI: 10.1016/J.MECHMACHTHEORY.2021.104374>